Naval Research Laboratory

Washington, DC 20375-5320

Advanced Radiation Theory Support Annual Report 2002, Final Report

J. Davis
J. Apruzese
Y. Chong
R. Clark
A. Dasgupta
J. Giuliani
P. Kepple
R. Terry
J. Thornhill
A. Velikovich

Radiation Hydrodynamics Branch
Plasma Physics Division

May 1, 2003

20030529 044

REPORT DOCUMENTATION PAGE

Form Approved
OMB No. 0704-0188

1. REPORT DATE (DD-MM-YYYY)	2. REPORT TYPE	3. DATES COVERED (From - To)
May 1, 2003		1 October 2001 - 30 September 2002

4. TITLE AND SUBTITLE

Advanced Radiation Theory Support Annual Report 2002, Final Report

5a. CONTRACT NUMBER
67-0857-A3-5

5b. GRANT NUMBER

5c. PROGRAM ELEMENT NUMBER

6. AUTHOR(S)

J. Davis, J. Apruzese, Y. Chong, R. Clark, A. Dasgupta, J. Giuliani, P. Kepple, R. Terry, J. Thornhill, and A. Velikovich

5d. PROJECT NUMBER

5e. TASK NUMBER

5f. WORK UNIT NUMBER

7. PERFORMING ORGANIZATION NAME(S) AND ADDRESS(ES)

Naval Research Laboratory, Code 6720
4555 Overlook Avenue, SW
Washington, DC 20375-5320

8. PERFORMING ORGANIZATION REPORT NUMBER

NRL/MR/6720--03-8660

9. SPONSORING / MONITORING AGENCY NAME(S) AND ADDRESS(ES)

Defense Threat Reduction Agency
6801 Telegraph Road
Alexandria, VA 22310

10. SPONSOR / MONITOR'S ACRONYM(S)

11. SPONSOR / MONITOR'S REPORT NUMBER(S)

12. DISTRIBUTION / AVAILABILITY STATEMENT

Approved for public release; distribution is unlimited.

13. SUPPLEMENTARY NOTES

This research was sponsored by the Defense Threat Reduction Agency under Job Order Title "Advanced Radiation Theory Support," MIPR No. 02-2045M.

14. ABSTRACT

This report describes the work of the Radiation Hydrodynamics Branch during FY 2002 in support of the DTRA PRS Program. Critical issues covered are: (1) side-on and end-on x-ray imaging of wire and gas puff implosions, (2) multi-group radiative diffusion, (3) discussions of radiation transport that includes pitfalls inherent to radiation modeling of Z-pinch plasmas, (4) K-shell yield performance assessment of argon loads on DTRA machines, (5) Z-pinch-driven direct drive inertial confinement fusion, (6) Z-scaled K-shell dielectronic recombination rate coefficients, (7) modeling enhanced energy coupling in Z-pinch plasmas, (8) incompressible fluid model for wire array implosions, and (9) increasing K-shell yields by using a low-z gas in the outer shell of a double-puff nozzle.

15. SUBJECT TERMS

Decade; Enhanced energy dissipation; Long time implosions; Large radius implosions; Transport coefficients; Diagnostic line ratios; Rayleigh-Taylor instability; Plasma radiation source; Radiation MHD; Z-pinch physics

16. SECURITY CLASSIFICATION OF:			17. LIMITATION OF ABSTRACT	18. NUMBER OF PAGES	19a. NAME OF RESPONSIBLE PERSON
a. REPORT	b. ABSTRACT	c. THIS PAGE	UL	150	J. W. Thornhill
Unclassified	Unclassified	Unclassified			19b. TELEPHONE NUMBER (include area code) (202) 404-4383

Standard Form 298 (Rev. 8-98)
Prescribed by ANSI Std. Z39.18

i

CONTENTS

EXECUTIVE SUMMARY

This report describes the theory support of DTRA's Plasma Radiation Source (PRS) program carried out by NRL's Radiation Hydrodynamics Branch (Code 6720) in FY 2002. Included is work called for in DTRA MIPR 02-2045M - "Plasma Radiation Theory Support" and in DOE's Interagency Agreement DE-AI03-02SF22562 - "Spectroscopic and Plasma Theory Support for Sandia National Laboratories High Energy Density Physics Campaign."

Some of this year's work was presented at the Dense Z-Pinches 5th International Conference held June 23-28 in Albuquerque, New Mexico. A common theme of many of these presentations was a demonstration of the importance of correctly treating the radiation physics for simulating Plasma Radiation Source (PRS) load behavior and diagnosing load properties, e.g. stagnation temperatures and densities. These presentations are published in the AIP Conference Proceedings and, for reference, they are included in Section I of this report. Rather than describe each of these papers in the Executive Summary, we refer to the abstracts that accompany each paper. As a testament to the level of involvement and expertise that our Branch brings to DTRA as well as the general Z-Pinch community, eight first-authored presentations were contributed at this conference as well as a Plenary and an Invited talk. The remaining four sections of this report discuss subjects either not presented at the conference or requiring more space than allotted in the Proceedings, they are:

(II) 6720 has demonstrated the importance of correctly modeling radiation physics in order to understand and thus control PRS load behavior. Historically this understanding and control has been achieved by reliable feedback between experiment, model development, load design, and plasma diagnostics and analysis. The correct treatment of radiation physics is an essential element in all these efforts. In this regard, 6720 is a unique organization in that it employs comprehensive radiation and ionization dynamics models that correctly characterize the radiation physics of L-shell and K-shell emitting PRS loads. Other approaches typically utilize computationally rapid algorithms at the expense of properly modeling the radiation physics. Code 6720 has also developed fast algorithms, but they contain more radiation physics than historically has been the case. In addition, they are benchmarked against the full transport methods so that their limits of validity are known. These algorithms include: multi-group diffusion models - for treating

low energy photon transport, and the Tabular Collisional Radiative Equilibrium model, which makes realistic L-shell and K-shell radiation transport feasible in multi-dimensional MHD codes. This section summarizes the basic theory and equations of radiation transport and why its correct treatment is so important to DTRA for maintaining sustained progress in PRS load development.

(III) In this section we demonstrate some encouraging results attained by replacing argon with a low-Z gas in the outer shell of a 4-3-2-1 nozzle. These calculations provide theoretical evidence that attaining high argon K-shell yields from more massive loads than presently envisioned on Decade Quad (DQ) are possible if a low-Z gas, rather than argon, is employed in the outer shell. This means that for a given load configuration, e.g. the 4-3-2-1 nozzle, more of the DQ current and energy could be used for producing K-shell emission. Note the idea of replacing argon with a low-Z gas in the outer shell is an idea that has been discussed by the PRS community for some time. Such a study was recommended in the Summary of the Second Meeting of the DTRA PRS Working Group, which took place in October 2002. The work presented in this section was performed in response to that recommendation.

(IV) All aspects of the evolution of wire-array plasmas are not yet completely understood. Depending on the current drive and the number of wires initially in the inner and outer arrays, the imploding plasmas can behave as either penetrating, in which the outer array passes through the inner array, or non-penetrating. Modeling this dynamics is important for DTRA if it is going to be able to design PRS loads that optimize plasma conditions for producing high-energy photons either by K-shell line radiation (moderate- to high-Z plasmas) or else by recombination radiation (moderate-Z plasmas). This section develops and describes an analytical multi-wire implosion model that is capable of fundamentally demonstrating this transition from an array that implodes as individual wire columns (penetrating) to one that behaves as a shell-like (non-penetrating) configuration.

(V) Dramatic increases in the total radiated energies were seen in Al wire array experiments on the Saturn generator at Sandia National Laboratories when it was operated in a long current rise-time mode as opposed to a short rise-time mode. Radiated yields were of the order of the JxB coupled energy for short rise-time implosions and two to four times that value for long rise-time implosions. The study described in this section makes a strong case that, in addition to JxB

energy inputs, there has to be an anomalous energy input into these long pulse Saturn aluminum experiments. This extra input is of the order 0.4 Ohms of resistance coupled to the circuit that pumps energy into the plasma during the later stages of the implosion. One mechanism for enhancing generator coupling is through the growth of micro-instabilities at the pinch surface and another possibility is the presence of magnetic bubbles. Identifying and controlling this phenomenon is critical to the DECADE program if it is to channel this additional energy into K-shell radiation.

I. A Compilation of Papers Presented at the 5$^{\text{th}}$ International Conference on Dense Z Pinches

Calculated Evolution of Side-on and End-on X-ray Images of Wire and Gas Puff Implosions on Z

J. P. Apruzese,[a] J. W. Thornhill,[a] C. Deeney,[b] C. A. Coverdale,[b] J. Davis,[a] A. L. Velikovich,[a] H. Sze,[c] P. L. Coleman,[d] B. H. Failor,[c] J. S. Levine,[c] and K. G. Whitney[e]

[a]*Radiation Hydrodynamics Branch, Plasma Physics Division, Naval Research Laboratory, Washington, DC 20375 USA*
[b]*Sandia National Laboratories, Albuquerque, NM 87185 USA*
[c]*Titan Systems Corporation, Pulse Sciences Division, San Leandro, CA 94577 USA*
[d]*Alameda Applied Sciences Corp., San Leandro, CA 94577 USA*
[e]*Berkeley Scholars, Inc., Springfield, VA 22150 USA*

Abstract. As $J \times B$ forces implode a Z-pinch load, a variety of phenomena that affect its radiative behavior may occur. These include snowplows and shocks, instabilities, amplification of initial load asymmetries, and high-density condensations (possibly caused by a local radiative collapse). On the axis, arrival of the main load mass occurs, but it may be preceded by a precursor plasma. An important aim of experimental diagnostics is to determine the degree and importance of such physical processes as a function of the properties of the load and the driving generator. X-ray spectroscopy and imaging are well-established components of most Z-pinch diagnostic suites. The purposes of the present work are to determine the x-ray signatures of some of these phenomena and to ascertain the x-ray energies that provide the clearest and least ambiguous indicators of these processes. To accomplish this, we have carried out radiation hydrodynamics calculations of argon gas puff and titanium wire array loads imploded on Sandia's Z generator. These calculations provide a large database of x-ray spectra and images. Some clear image signatures are seen in the calculations. These include intensity enhancement near the outer edge of the pinch, which is characteristic of the heating and compression that occurs in the snowplowed region of the pinch prior to its final on-axis assembly. Spatial image intensity profiles in the lower energy x-rays are generally indicative of the density profile of the pinch. The profile of the image at different photon energies within the K-shell spectral region is related to the presence of an electron temperature gradient.

INTRODUCTION

X-ray pinhole imaging of Z pinches has been used to assess and improve pinch "quality". This diagnostic has also provided quantitative measurements of the diameter of Z pinches to apply spectroscopy to diagnose their average temperature and density (see, e.g., Ref. 1). Undoubtedly, much more information is contained in such images,

2

especially with regard to spatial variations of temperature and density. Routine, accurate diagnosis of these variations as a function of load and the current that drives it would be likely to provide valuable insight into the physical processes that are thought to create such variations. These include: formation of "snowplowed" regions, shocks, various plasma and hydrodynamic instabilities, on-axis assembly and compression, and radiative collapse. The fundamental purpose of our calculations is to connect the x-ray images of Z pinches to the conditions that produce the images, thereby optimizing the extractable information from pinhole images and their diagnostic cousin, spatially resolved spectroscopy.

MODEL AND CALCULATIONS

The implosion dynamics of argon and titanium loads on Sandia National Laboratories' Z generator [2] were calculated with a one-dimensional (1D) Lagrangian magnetohydrodynamic (MHD) model [3] in which detailed configuration atomic models and tabular collisional-radiative equilibrium radiation transport [4] are used to calculate the evolution of the ionic species, level populations, and spectra. As described in Ref. 3, enhanced viscosity is employed to model multidimensional effects such as turbulent flow. For 15-30 ns surrounding peak compression, the radiative transfer was computed on expanded numerical grids of 40 rays and ~ 2200 photon frequencies [5], to allow for calculation of detailed pinhole images at virtually any x-ray energy or specified band of energies. Both side-on and end-on images can be calculated.

The initial load conditions were chosen to approximately correspond to those of two very successful shots on Z. For Ar, a mass load of 0.8 mg/cm was distributed in two broad peaks centered near radii of 15 and 35 mm. This load is similar to that of Z shot 663, which produced 274 kJ of Ar K-shell radiation [6]. For the Ti calculation, a mass load of 1.1 mg/cm was assumed, 75% of which was concentrated at a radius of 22.5 mm, and the remainder distributed nearly uniformly in the interior. These conditions are similar to those of the single array Z shot 303, which produced 120 kJ of Ti K-shell radiation. The main purpose of analyzing the calculations was not detailed comparison with experiment, but to enhance the diagnostic value of pinhole imaging and spatially resolved spectroscopy. The calculations do reproduce the experimental K-shell yields within 35%, the diagnosed average temperatures within 20%, and the corresponding densities to within a factor of 2. However, the calculated K-shell pulse widths are too short by factors of 2-3. For the Ti load, a 3 ns pulse width was calculated vs. 7 ns measured, and for Ar the corresponding values are 5 ns calculated vs. 12 ns measured. These are compensated by greater calculated radiating load masses and powers, giving better agreement with measured K-shell yields.

RESULTS

The calculated density profiles for the Ar and Ti pinches at three times during the implosion are shown in Figs 1a and b. Note that a softer, more uniform density implosion results from the initially filled-in Ar puff load than from the mostly hollow single-array Ti load. For Ar, peak compression and K-shell power occur in the time frame 140-143 ns, and for the Ti load, these events occur at 121-123 ns. The electron temperature profiles at peak compression (not shown), are fairly similar. For both loads, a core temperature of ~ 2.5 keV remains relatively spatially flat out to about 75-90% of the total radius, at which point a sharp decline in temperature is followed by an increase due to ohmic heating in the further out, current-carrying plasma skin, then (for Ti) a decline at the very outer edge occurs. Figs. 2 a and b show the end-on L-shell images for the two loads, calculated by integrating the intensity from 0.4-1.0 keV for Ar, and 0.7-1.7 keV for Ti. Note that these intensity profiles are similar to the corresponding density profiles shown in Figs. 1 a and b. The corresponding K-shell image intensity profiles do not track the density profiles due to the temperature sensitivity of the higher energy x-ray emission.

(a)   (b)
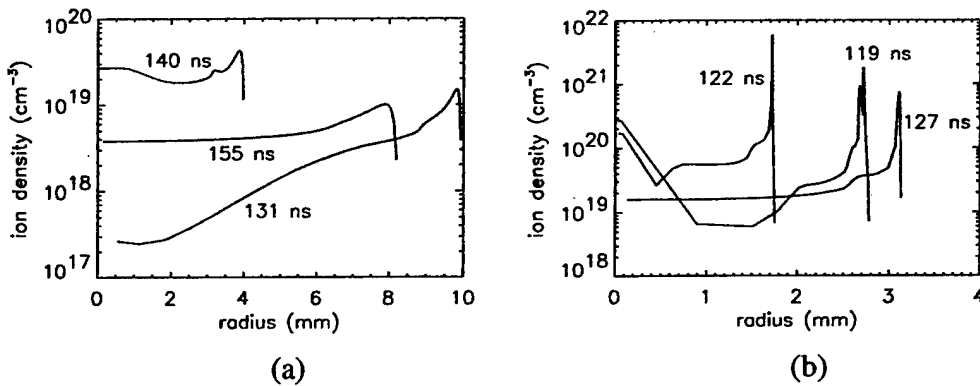
Fig. 1. Calculated ion density profiles at three times during the implosions of (a) Ar and (b) Ti.

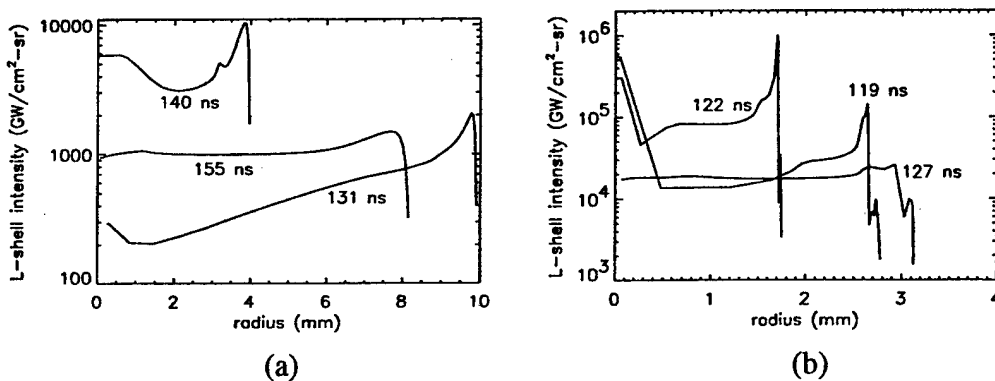

(a)   (b)

Fig. 2. Calculated L-shell intensity profiles at three times during the implosions of (a) Ar and (b) Ti.

4

Fig. 3 shows the side-on K-shell image of the Ti pinch near peak compression. There are two noteworthy features. One is the strong self-reversed core of the He-α line.
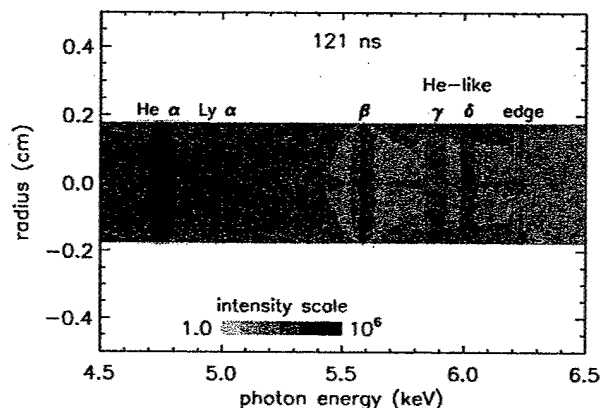

Fig. 3. The calculated K-shell side-on image of the Ti pinch near peak compression for hν=4.5-6.5 keV

This is due to the sharp decline in electron temperature at the very outer edge of the pinch. The second feature is an enhancement of intensity just inside the outer edge of the pinch (seen at photon energies of 5.5 to 6.2 keV). This reflects the increase in electron temperature that occurs just inward of the outer radius. The simultaneous collection of spectrally and spatially resolved data has the potential to be a powerful diagnostic of the pinch's temperature profile.

In summary, detailed calculations of the x-ray images of imploding Ar and Ti Z pinches have shown that x-ray "bright spots" are the result of corresponding enhancements of temperature, density, or both. Images of bright spots at lower photon energies are more likely to be the result of density, rather than temperature, enhancements. Self-reversals in the profiles of strong lines are sensitive to temperature gradients, as are spatial intensity profiles in the higher energy, K-shell regions of the x-ray spectrum. When the density falls with increasing distance from the pinch axis, it is found that the image is larger in the spectral lines than in nearby continuum regions.

ACKNOWLEDGMENT

REFERENCES

1. Whitney, K. G., et al., Phys. Plasmas 8, 3708 (2001).
2. Spielman, R. B., et al., Phys. Plasmas 5, 2105 (1998).
3. Thornhill, J. W., et al., Phys. Plasmas 1, 321 (1994).
4. Thornhill, J. W., et al., Phys. Plasmas 8, 3480 (2001).
5. Apruzese, J. P., et al., Phys. Plasmas 7, 3399 (2000).
6. Sze, H., et al., Phys. Plasmas 8, 3135 (2001).

Direct Drive Inertial Confinement Fusion in a Z-Pinch Plasma

Robert W. Clark, Jack Davis, Alexander Velikovich,
Leonid Rudakov[a], and John L. Giuliani, Jr.

Radiation Hydrodynamics Branch, Plasma Physics Division
Naval Research Laboratory, Washington, DC 20375
[a]Berkeley Research Associates, Inc., P. O. Box 852, Springfield, VA 22150 USA

Abstract. The recent successes with the Saturn and "Z" facilities at Sandia National Laboratory have renewed interest in Z-pinch fusion as a means of producing an abundance of high-energy photons. We have estimated that, in a nuclear fusion pulsed Z-pinch, peak currents in excess of 20-30 MA may produce magnetic fields sufficient to confine α-particles. We performed a series of numerical simulations with Au/CH/DT loads for devices with peak currents ranging from 20 to 60 MA. A detailed ionization model for Au was employed, and includes a forest of transported emission lines or line groups. For each case, we will give the calculated D-T yield and the yield of the α-particles deposited in the plasma.

INTRODUCTION

The "Z" facility at Sandia National Laboratory is capable of putting 18-20 MA into a load, and in a few years, the "ZR" machine will be able to produce load currents in excess of 25 MA. The recent successes with large Z-pinch devices have renewed interest in Z-pinch fusion as a process for creating a hot dense plasma. However, the prospects for designing an operating fusion device depend on the results from some very basic research. Can substantial thermonuclear burn be produced in a Z-pinch? How efficiently will the α-particles, which carry much of the fusion energy, be confined in the plasma? At what values of the magnetic field will magnetic confinement of the α-particles occur? If breakeven cannot be achieved, will such devices be useful for enhanced high-energy photon PRS output? In previous studies [1,2] we explored at the prospects for ignition in a high-current Z-pinch and found that (1) The magnetic fields produced in a 30 MA pinch may be sufficient to confine α-particles, (2) Low-Z Bremsstrahlung (characteristic of fusion plasmas) may be an attractive alternative for enhancing the photon spectra for PRS applications, and (3) Stabilization in the early phase and high-compression (exceeding Bennett equilibrium) in the final stage is a promising path to Z-pinch fusion. Several DT/CH configurations were considered to quantify these hypotheses, including a D-T shell with a CH pusher and a B_z interlayer. A summary of the Au/CH/DT configurations and D-T yields is given in Figure 1.

MODEL

The dynamics of the radially imploding Z-pinch plasma was simulated using a one-dimensional multi-zone non-LTE radiation-magnetohydrodynamics code, DZAPP [3], which uses a transmission line circuit model to represent the driving generator. The thermonuclear burn was calculated using rates from Glasstone and Lovberg [4], and a diffusion model was

used for the transport of the α -particles. The diffusion equation for the α-particle energy density E_α takes the form

$$dE_\alpha / dt = (1-\gamma)\, E_\alpha\, div\, \mathbf{v}) + div\,(D\, grad\, E_\alpha) + S - 2\, v_e\, E_\alpha$$

where $\gamma=c_p/c_v$ is the gas constant and $\mathbf{v}$ is the velocity. The α-particle diffusion coefficient and the electron-ion collision frequency are given by

$$D = Q / [(v_e m_i)\, (9 + \Omega_i^2 / v_e^2)]$$
$$v_e = n_e\, \Lambda\, Z^2\, (m_e/m_i) / (3.44 \times 10^5\, T_e^{3/2})$$

where T_e and n_e are the electron temperature and density, Λ is the Coulomb logarithm, and Q is the initial α-particle energy (3.52 MeV). The α-particle source term $S = -Q\, d[T]/dt$, where [T] is the local tritium concentration (we assume that [D] = [T]). This treatment takes the local transverse magnetic field into account via the term involving the ion cyclotron frequency $\Omega_i = ZeB / m_i c$ in the diffusion coefficient D. The circuit model used in the simulations is based on an equivalent circuit for the Z generator. An extensive atomic database was used for each of the elements in the target, and detailed radiation transport was performed [5-7].

Configuration	Mass [mg]			Current	B_z (t=0)	DT Yield [kJ]	
	DT	CH	Au			E_{burn}	E_{dep}
DT shell + CH shell + Au coating (Nested Shells)	0.561	0.523	0.48	20 MA	0.00 MG	6.60	1.02
DT shell + CH shell +	5.045	4.703	1.372	60 MA	0.10 MG	803.00	531.00
Au coating (Nested Shells)	2.242	2.090	0.593	40 MA		156.00	112.50
B_z interlayer	0.561	0.523	0.148	20 MA		5.20	3.60

$$M_o = \frac{\mu\, I_{max}^2\, \tau^2}{\{4\pi\, \Pi\, R_o^2\}}$$
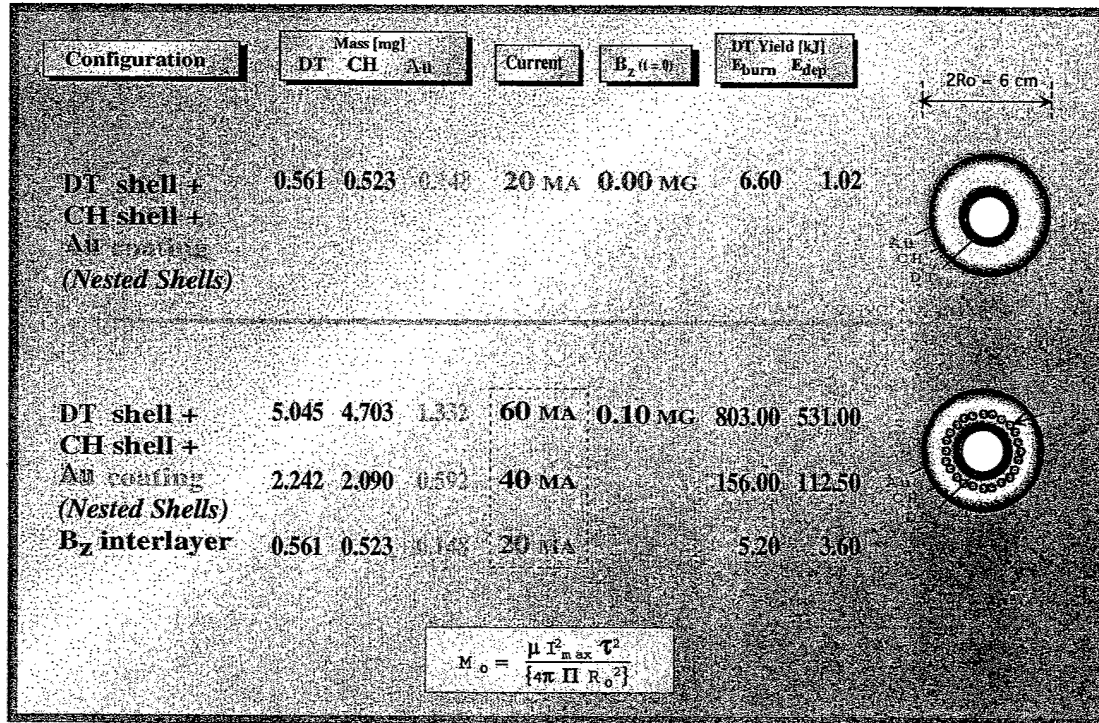
FIGURE 1. Initial configurations and yields for Au/CH/DT Z-pinch implosions

RESULTS

Although a number of different load designs were investigated, we will describe only the results with a D-T shell, an Au-coated CH Pusher and B_z Interlayer. In simple D-T implosions, the thermonuclear burn is inefficient, even at the highest currents. The ion temperature, which approaches 100 keV for the 60 MA case, is certainly sufficient to provide nearly optimum D-T reaction cross-sections. Unfortunately, the plasma density is not very high in the hottest regions. Also, the plasma bounces, quickly reducing the temperature and density; the D-T becomes too cool for fusion after only a few nanoseconds. A mechanism which could delay the bounce would likely improve the burn efficiency. The most complex (and promising)

7

series of simulations involved concentric D-T and Au/CH shells separated by a B_z interlayer. The axial magnetic field is embedded in the plasma at time t=0, such that it is uniform between the D-T and Au/CH shells and zero elsewhere. Such a field configuration could be established between two wire arrays if they were twisted slightly in opposite directions [8]. The initial magnitude of the B_z interlayer was varied over a fairly large range, and it was found that values of B_z near about 100 kilogauss gave the best yields. We considered three peak currents: 20, 40 and 60 MA. In all cases, as the implosion progresses, the axial field diffuses into (and eventually through) the D-T and Au/CH shells. In addition, when the Au/CH shell impinges on the underlying D-T plasma, the B_z interlayer is compressed until it is comparable in magnitude to the azimuthal field B_θ driving the implosion. Thus, the B_z interlayer ultimately becomes quite thin. The magnetic interlayer also has the property of confining the α- particles in the D-T region. The yields vary strongly with current, $E_{D-T} \sim I_{max}^{4.5}$.
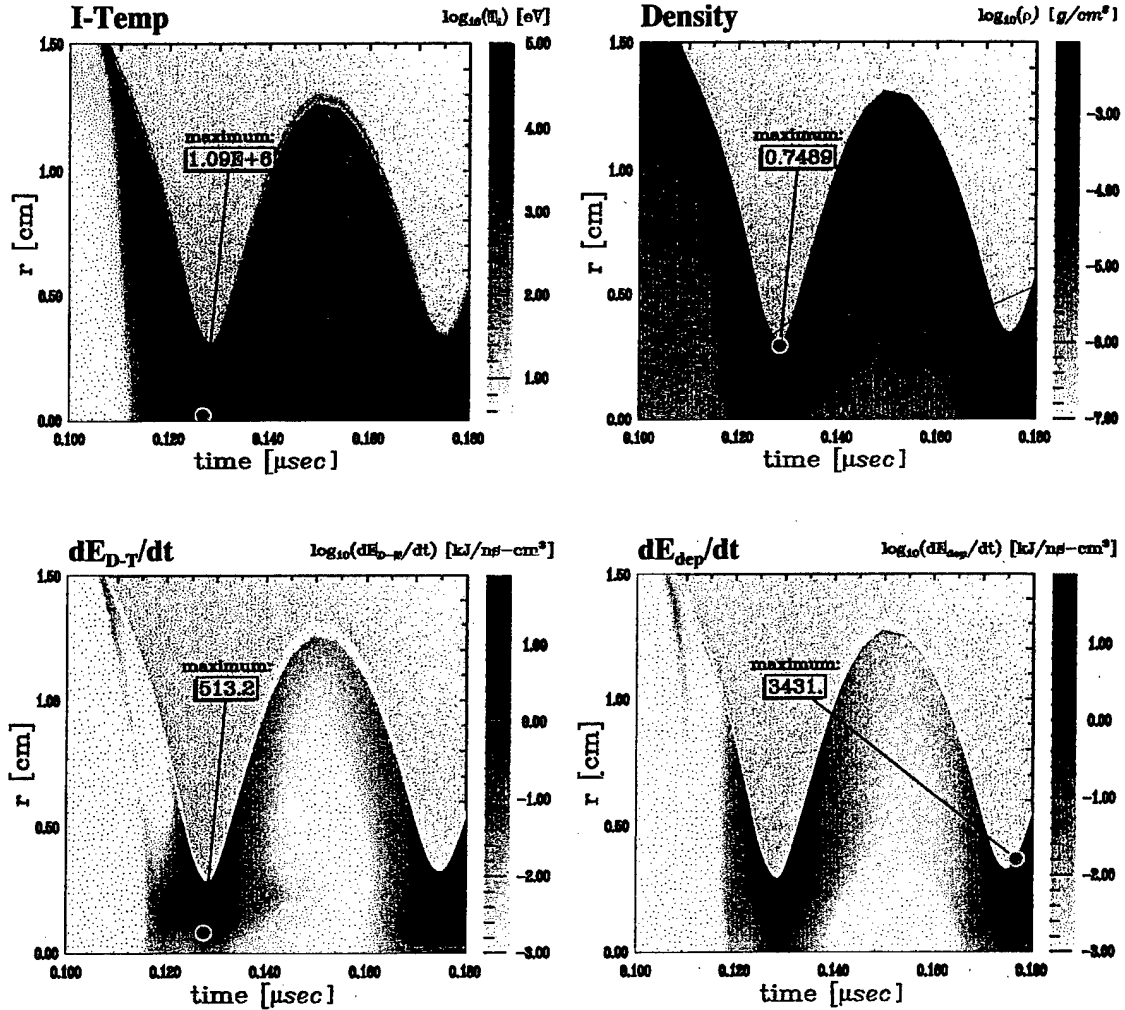

FIGURE 2. History of ρ, T_e, fusion heating and α-deposition for the 60MA case.

In the three simulations, although the *peak ion temperature* does not vary by very much, the temperature in the vicinity of maximum burn increases with current. In addition, the ion density increases with current. The masses were scaled so that the bounce occurs at about 125

ns in each case. At 20 MA, a second bounce occurs, but it is very weak, and little D-T burn occurs. At 40 MA, the subsequent bounce is stronger, and the burn is more robust (but the second pulse of α-particles is much less than the first). For the 60 MA case, the burn in the second pulse of α-particles is nearly as large as the first. The histories of several important quantities from the 60 MA case are shown in Figure 2: ion temperature T_i, density ρ, fusion heating dE_{D-T}/dt, and α-particle deposition dE_{dep}/dt. As is characteristic of z-pinch implosions, the electrons remain substantially cooler than the ions. Most of the burn occurs away from the axis, where temperature and density are *both* favorable. The α-particles produced in the reaction are stopped most efficiently in the cool dense outer region of the target, particularly the Au layer. The yields are given in Fig 1.

CONCLUSIONS

We have investigated load designs that might be employed to produce D-T fusion in proposed Z-pinch devices and found that high currents (I > 40 MA) reduce α-particle losses, but that they are not necessarily deposited where they will do the most good (in terms of increasing the burn fraction). The α-particle deposition occurs mostly in cool, dense plasma near the outer edge of the pinch. D-T burn in these devices seems to be limited more by density (and the rapidity of the bounce) than by the ion temperature. At the highest currents, it is easy to obtain 100 keV ions near the axis. The yield is improved with a massive Au/CH pusher, and improved still further when an axial magnetic interlayer was introduced. The load parameters (initial radii, array masses, etc.) were selected to give good energy coupling to the load, but were not optimized. It is likely that substantially improved fusion-like plasma conditions capable of radiating high-energy photons could be obtained after some adjustment of these parameters. In particular, the nested array simulations assign approximately equal masses to the inner (fuel) and outer (pusher) plasmas. However, the fusion yields do not reach breakeven (even at 60 MA). Substantially higher ion temperatures in the fuel and increased yields could be obtained by decreasing the fuel mass M_{D-T} and increasing the pusher mass M_{pusher} such that the total mass $M_o = M_{D-T} + M_{pusher}$ is unchanged, but with $M_{pusher} / M_{D-T} \sim 10$.

ACKNOWLEDGMENTS

REFERENCES

1. "*Advanced Radiation Theory Support Annual Report 1998, Final Report*", Radiation Hydrodynamics Branch, Naval Research Laboratory.
2. S. M. Gol'berg et al., "*Compression, heating and fusion in Megagauss Z-Q pinch systems*", in Dense Z-Pinches, ed. N.R. Periera, J. Davis and N. Rostoker (AIP, NY, 1989). Phys. Rev. Lett. **81**, 4883 (1998).
3. J. Davis, J. Giuliani, Jr., M. Mulbrandon, Phys. Plasmas **2**, 1766 (1995).
4. S. Glasstone and R. H. Lovberg, "*Controlled Thermonuclear Reactions*", (Van Nostrand, NY, 1960), Chapt. 2.
5. D. Duston, R. W. Clark, J. Davis and J. P. Apruzese, Phys. Rev. A **27**, 1441 (1983).
6. J. P. Apruzese, J. Davis, D. Duston and R. W. Clark, Phys. Rev. A **29**, 246 (1984).
7. J. P. Apruzese, J. Quant. Spect. Rad. Transf. **34**, 447 (1985).
8. R. E. Terry and R. W. Clark "*Analysis of Magnetic Interlayer Staged PRS Loads*", in Dense Z-Pinches, ed. N. R. Periera, J. Davis and P. E. Pulsifer (AIP, NY, 1987).

Z-scaled K-shell Dielectronic Recombination Rate Coefficients

Arati Dasgupta, Paul Kepple, and Jack Davis

Naval Research Laboratory, Plasma Physics Division,
Radiation Hydrodynamics Branch, Washington, DC 20375, USA

Abstract. We present total as well as state-specific dielectronic recombination (DR) data such as singly and doubly-excited state energies, autoionization and radiative rates and DR branching ratios for recombination from H-like to He-like and from He-like to Li-like ions. The data obtained are calculated using a detailed Hartree-Fock calculation with relativistic corrections. Explicit calculations for Al, Ti, and Kr are performed to cover a range of ions such that scaling relations obtained using these data can be used to interpolate the DR data for any ion of interest within this range and may be somewhat beyond. Since accurate and detailed state-specific knowledge of DR rate coefficients are crucial for atomic model development of any species, these present data will be extremely relevant for analysis of z-pinch physics.

INTRODUCTION

Dielectronic recombination (DR) is an important process for ionization balance in a non-LTE plasma of moderate to high-Z ions. The dielectronic satellite lines appearing on the long–wavelength side of the resonance lines as a result of this recombination can be used as plasma temperature and density diagnostics and analysis of x-ray spectra. DR is a two-step ion-electron resonant collision process in which an electron undergoes radiationless capture into an autoionizing doubly excited state followed by radiative decay into a singly excited state of the recombined ion. These doubly excited states can also autoionize to the ground or other possible excited states of the initial ion.

In the low-density corona approximation, the DR rate coefficients α^{DR} from initial state i to final state k through intermediate autoionizing state j at temperature T is given by

$$\alpha^{DR}(i,k) = \left[\frac{4\pi\Re}{kT}\right]^{3/2} \frac{a_0^3}{2g_i} \sum_j F_{ijk} \exp(-\varepsilon_j / kT), \qquad (1)$$

where

$$F_{ijk} = \frac{g_j A^a_{ji} A^r_{ik}}{\sum_{i'} A^a_{ji'} + \sum_{k'} A^r_{jk'}}. \qquad (2)$$

Here g_i and g_j are the statistical weights of the initial and final states, kT is the electron temperature, ε_j is the energy of the free recombining electron, A^a_{ji} and A_{jk}^r are the autoionization and radiative rates from state j to states i and k respectively.

10

These DR branching ratios also provide a direct measure of the intensity of satellite lines produced due to this recombination and they can be used for plasma diagnostics of electron temperature:

$$I(j,k) = N_e E_{jk} \left[\frac{4\pi\Re}{kT} \right]^{3/2} a_0^3 \frac{e^{-\varepsilon_j/kT}}{2} \sum_i \frac{N_i}{g_i} F_{ijk}. \tag{3}$$

In this equation, N_e is the electron density, N_i is the density of initial state and E_{jk} is the energy of the satellite line.

Most of the published works present only total DR rates as a function of temperature. In this work we present state-specific DR rates and the total rate can easily be obtained by summing these rates. More importantly, the Z dependence of various DR data are determined using detailed calculations of Al, Ti, and Kr ions. These scaling relations can then be used to obtain DR rates and satellite line data for any ion between Al and Kr and maybe somewhat beyond with little effort.

ATOMIC MODEL AND Z SCALING

Evaluation of detailed DR data requires considerations of many doubly and singly excited levels. Although in some instances it is necessary to work at the fine-structure levels, this leads to the generation of a superabundance of atomic data. In order to calculate the ionization balance of non-coronal plasma it is sometimes more practical to work at the configuration level. If necessary, one can determine multiplet emissions from the configuration populations as a next step.

Our atomic model for recombination from H- to He-like ions consist of the initial $1s$ ground state, 33 doubly-excited He-like states of which there are 31 unlumped $2lnl'$ and two lumped $2sn''l''$ and $2pn''l''$ states and 11 final singly-excited states of $1snl'$ configurations. Here l takes on values 0 and 1, $2 < n < 7$, $0 < l' < 7$, $7 < n'' < 20$, and $l'' < 7$. We consider an equivalent atomic model for our calculations of DR data for recombination from the He- to Li-like recombination. The calculations of all the quantities relevant for obtaining F_{ijk} in Eq. (2) were obtained using the HFR (Hartree-Fock with relativistic corrections) code of R. D. Cowan [1]. The theoretical methods used in these calculations are given in detail in Ref. 2. At configuration level, i, j, and k in Eq. (2) go over to the configuration averaged labels a, b, and c respectively and the configuration averaged DR branching ratios F_{abc} and intensity $I(b,c)$ can be expressed in terms of the configuration-averaged energies, rates and statistical weights by replacing i, j, and k in Eq. (2) and (3) by a, b, and c respectively.

The scaling of F_{abc}, $\alpha^{DR}_{(a,c)}$ and $I(b,c)$ is accomplished by scaling A_{bc}^a, A_{ba}^r, and ε_b. These rates A_{bc}^a, and A_{ba}^r depend on Z through the doubly- and singly-excited states energies ε_b and ε_a. We found that these quantities scale as

$$\varepsilon_b = Z^2 (b_0^{**} + b_1^{**} + b_2^{**} + b_3^{**})_b \tag{4}$$

$$\varepsilon_c = Z^2 (b_o^* + b_1^* + b_2^* + b_3^*)_c \tag{5}$$

$$A_{bc}^r = Z^4 (b_0^r + b_1^r / Z + b_2^r / Z^2 + b_3^r / Z^3)_{bc} \tag{6}$$

$$A_{ba}{}^a = (b_0{}^a + b_1{}^a / Z + b_2{}^a / Z^2 + b_3{}^a / Z^3)_{ba} \qquad (7)$$

Accommodating the scaling behaviors of both A^r and A^a, the DR branching ratio is expressed as a four-coefficients polynomial :

$$F_{abc} = Z^2(b_0{}^F + b_1{}^F / Z + b_2{}^F / Z^2 + b_3{}^F / Z^3) \qquad (8)$$

A partial list of scaling coefficients for the doubly excited states energies and the branching ratios F_{abc} for recombination from H- to He-like ions are given in Tables I and II respectively. We do not present any scaling data for He- to Li-like recombination.

TABLE I. Scaling Coefficients for energies of doubly-excited He-like states

b	state	$b_0{}^{**}$	$b_1{}^{**}$	$b_2{}^{**}$	$b_3{}^{**}$
1	2s2p	5.458E-01	-1.879E+00	3.686E+01	-2.112E+02
2	2p^2	5.604E-01	-2.525E+00	4.881E+01	-2.796E+02
3	2s3p	6.913E-01	-2.313E+00	4.224E+01	-2.417E+02
4	2p3p	7.063E-01	-3.025E+00	5.452E+01	-3.121E+02
5	2p3d	7.094E-01	-3.149E+00	5.693E+01	-3.256E+02
6	2s4p	7.429E-01	-2.533E+00	4.494E+01	-2.573E+02
7	2p4s	7.554E-01	-3.118E+00	5.467E+01	-3.119E+02
8	2p4p	7.575E-01	-3.221E+00	5.664E+01	-3.239E+02

TABLE I. Scaling Coefficients of DR branching ratios F_{abc} for He-like states

b	c	$b_0{}^F$	$b_1{}^F$	$b_2{}^F$	$b_3{}^F$
1 (2s2p)	1 (1s 2s)	-1.032E-01	8.302E+00	-1.255E+02	6.060E+02
2 (2p^2)	2 (1s2p)	-4.363E-01	3.251E+00	-5.099E+02	2.339E+03
3 (2s3p)	1 (1s2s)	-3.255E-02	2.524E+00	-3.753E+01	1.738E+02
4 (2p3p)	2 (1s2p)	-2.371E-02	1.626E+00	-1.102E+01	-4.836E+01
4 (2p3p)	4 (2s2p)	-8.160E-02	5.427E+00	-1.711E+01	-3.752E+02
5 (2p3d	5 (1s3d)	3.123E-03	-5.255E+00	4.835E+01	-3.699E+02
7 (2p4s)	6 (1s4s)	2.375E-03	-2.376E+00	1.260E+01	-8.643E+01
8 (2p4p)	2 (1s2p)	1.251E-03	-1.445E+00	8.567E+00	-7.771E+01

The total DR rates for each ion are obtained by summing the state-specific rates $\alpha^{DR}(a,c)$ over all the final singly excited recombined state c. In calculating the DR rates to each of these singly excited state, we explicitly calculated all the data for $n<20$ and employed the usual $1/n^3$ extrapolation procedure for all bound Rydberg levels of the captured electron with $n>20$. These total DR rates are shown in Fig. 1 as a function of temperature.

In order to investigate the reliability of this scaling, we performed detailed calculations for selenium ions and compared the DR rates obtained with those evaluated using the scaling coefficients and these are also presented in Fig. 1. We see that the scaled DR rates for H- and He-like Se obtained using the scaling coefficients given in Tables I and II (only partial data are included here) and the scaling relations given above are very close to those calculated explicitly.
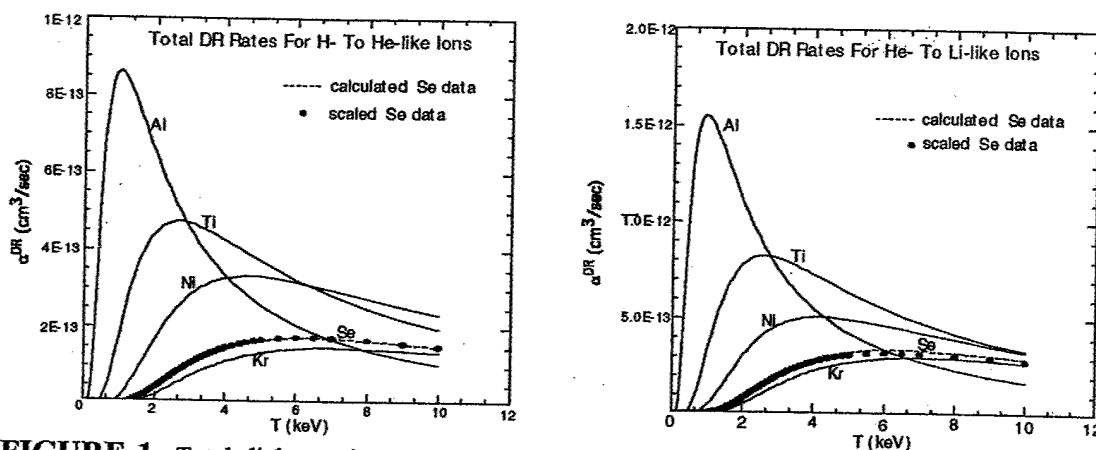
FIGURE 1. Total dielectronic recombination rates for H-to He-like and He- to Li-like ions. Shown are also the calculated as well as scaled DR rates for selenium.

SUMMARY

The reliability and scalability of atomic data used in the ionization calculations of K-shell moderate-Z elements are of great concern. For ionization balance calculations, data obtained at the configuration-averaged level are quite reliable although the accuracy of these data should be checked against other published configuration-averaged data. The number of dominant channels included in our calculations combine to give 95% or more of the total DR rates for recombination from H- and He-like ions. All the atomic quantities scale very smoothly From the data presented for selenium in Fig. 1, we conclude that the DR rates obtained using the scaling coefficients, one can very accurately predict the DR dates for any ion between argon and krypton without any detailed and difficult calculations. It will be instructive to investigate the scalability of these DR rates beyond the range of Z considered here by extrapolating these calculated data [3].

ACKNOWLEDGMENTS

REFERENCES

1. Dasgupta, A., and Whitney, K. G., *Phys. Rev. A* **42**, 2640-2652 (1990).
2. Cowan,R. D., in *Book The Theory of Atomic Structure and Spectra*, University of California Press, Berkeley, CA., 1981.
3. Dasgupta, A., and Whitney, K. G., *J. Phys. B* **28**, 515-529 (1995).

Pitfalls in Radiation Modeling of Z-Pinch Plasmas[+]

J. Davis,[a] **J.L. Giuliani,**[a] **J.P. Apruzese,** [a]**R.W. Clark,**[a] **J.W. Thornhill,**[a] **K.G. Whitney,**[a] **A. Velikovich,**[a] **Y. K. Chong,**[a] **C.A. Coverdale,**[b] **C. Deeney,**[b] and **P.D. LePell**[c]

[a]*Plasma Physics Division, Naval Research Laboratory, Washington, DC 20375 USA*
[b]*Sandia National Laboratories, Albuquerque, NM 87185 USA*
[c]*K-Tech Corporation, Albuquerque, NM 87106 USA*

Over the last three decades there has been a quantum jump in the production of x-rays from pulsed power driven Z-pinch plasmas. Total radiative yields have gone from a few kilojoules to almost two megajoules. This increase occurred as a result of higher current drivers coupled with improvements in our understanding of the issues most relevant to good load design. Critical analyses of experimental data have led to a better understanding of the load dynamics, which includes all phases of load evolution extending from the cold start to the final collapsed phase and the emission of the x-ray pulse. A Z pinch is a deceptively simple device that has a very complex plasma dynamics. It can be a platform for demonstrating a variety of textbook plasma instabilities. However, its primary application in the present context is as an intense source of x-ray radiation. Therefore it is attractive both as a direct source of x-rays and for creating hohlraum conditions for plasma fusion experiments. After a few historical comments are offered on how radiation has been treated in modeling Z pinches, some of the methodologies and models that are employed in this endeavor are discussed. These include both nonLTE and LTE ionization dynamic models and escape probability radiation transport and LTE radiation diffusion models. To illustrate their use, comparisons are made between experimental data from a stainless steel wire array pinch implosion and 1-D MHD calculations that employ these models. The consequences that stem from the compromises and trade-offs that result from the different approximations used in these models are addressed. We will explore the role that radiation plays in the dynamic evolution of a Z-pinch and demonstrate the need for as near a self-consistent radiation-hydrodynamics treatment as possible.

INTRODUCTION

Pulsed power driven Z-pinch plasmas have been studied for over 50 years both experimentally and theoretically. The recent sustained interest in and fascination with Z-pinch plasmas is due in large measure to the success of the Z facility's performance in rapidly heating dense wire array and gas puff plasmas to temperatures high enough to produce an intense burst of K- and L- shell x-rays from moderate atomic number elements. It is also due to an improved understanding of load performance and load design. The linear Z-pinch is a deceptively simple device that exhibits a complicated plasma dynamics. It finds application in conducting indirect drive fusion, x-ray lasers, and hohlraum physics experiments. However, for our purposes here, we focus on its primary application as an intense source of soft x-ray radiation producing upwards of about 2 megajoules of total radiation for a number of material loads.

The production and transport of radiation in Z-pinch produced plasmas are often modeled using a radiative diffusion approximation and assuming Local Thermodynamic Equilibrium (LTE). Since these plasmas are neither in LTE nor entirely opaque or transparent to the radiation, LTE and radiation diffusion are erroneous assumptions and only provide poor descriptions of the energetics, emission spectra and yield from Z-pinch plasmas. The application of inappropriate models easily leads to the misinterpretation of experimental data and to misunderstanding of the plasma dynamics and load

performance. Radiation modeling of Z-pinches (and laser produced plasmas) usually does not take the "high road" and rationalizes traversing the "low" road in the name of computational efficiency, which oftentimes is full of potholes, pitfalls and wasted computational resource.

The power radiated by a Z-pinch plasma consisting of multi-charged atomic ions can have important consequences on the plasma dynamics. The radiated power depends both on the detailed atomic structure of the ions and on the properties of the plasma such as T, N and opacity. Therefore, the calculation of the radiated power of a dynamically evolving Z-pinch represents a complex problem. In this presentation we discuss and assess some of the more common approximations employed to describe the radiative behavior of Z-pinch plasmas. Through the use of examples and illustrations, we show that in calculations with identical initial plasma conditions, atomic level structure and rate coefficient data, the change of radiation models has a strong affect on the dynamic evolution and hydrodynamic history of the plasma, often promoting an erroneous interpretation of experimental results. To illustrate the degree of error, we generate an emission spectrum using a 1-D radiation MHD model that self-consistently coupled to a circuit representing the Sandia Z-facility. Comparison between several radiation models for a multi-wire titanium array also illustrate the kinds of errors and pitfalls that are possible.

POPULATION KINETICS MODEL

The population kinetics model determines the occupation of atomic levels and ionization stages of the material load as a function of temperature, density, and opacity. The level dynamics is usually described by either Local Thermodynamic Equilibrium (LTE). Collision Radiative Equilibrium (CRE), or Time dependent (CRT) non-equilibrium, Corona Equilibrium (CE), or some form of Average Atom (AA) model with hydrogenic or averaged real atomic data. The level dynamics is important because it provides plasma opacity and emissivity data to the radiation transport models. This transport can be carried out using a variety of approximations from the simplistic Holstein escape factor to the solution of detailed moment equations for the emitted flux or intensity. We will focus on radiation diffusion and multi-cell, probability of escape, methods. For a fuller discussion of these see Davis, et. al.[1]

The average charge state, $Z_{Average}$, shown on Figure 1 for a gold plasma as a function of temperature for an ion density of 10^{20} cm^{-3} illustrating the large differences that are possible depending on the ionization dynamic model used (a) and temperature and density (b) for LTE, CRE and CE. For example, At a temperature of 1 keV the average charge state can differ by as much as 30 ionization stages at a density of 10^{20} ions. This result clearly demonstrates the need to determine the correct distribution of charge states because a number of parameters such as transport coefficients and the "color" of emitted photons depend on $Z_{Average}$. The only reason for adopting an LTE accounting of the level occupations is to simplify the calculations. Unfortunately, LTE is a bad approximation leading one has to ask why it is used and what does it provide. Figure 1 showing $Z_{Average}$ as a function of temperature and density illustrates the large errors involved in using an LTE model at low densities.
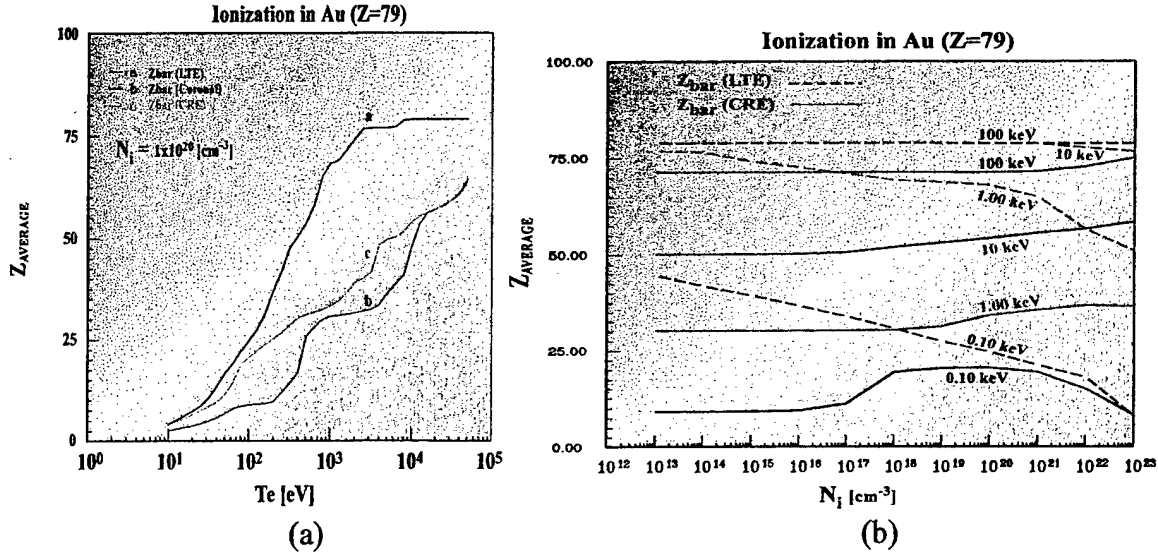
Figure 1. Average charge state for Au plasma

MODELING AND SIMULATION

The implosion dynamics of a titanium load on Sandia's Z facility was calculated with a one-dimensional (1D) Lagrangian MHD model using some commonly employed descriptions for the ionization dynamics and radiation transport. The simulations include LTE with single- and multi- group diffusion, CRE and TCRE[2] with on-the-spot transport. A summary of the total and K-shell calculated yields for six different cases are shown on Figure 2 along with experimental data for 3 loads. The numbers on the bar graph for the TCRE and NLCRE results represent the number of lines carried in the calculation. There are only minor differences between the calculated yields since the 126 line calculation was chosen judiciously. The experimental results with their shot number are also shown. . The single- and multi-group diffusion results for the total yield are similar, but the single group cannot produce a K-shell yield. Figure 3 isolates specific results from Figure 2 and exhibits the variation of the yield as a function of photon energy for the non-local and multigroup LTE diffusion simulations. A quick view of these results suggests that LTE in conjunction with single- or multi-group diffusion agrees well with experiment for the K-shell and total radiative yields. This could lead us to the conclusion that LTE and radiation diffusion adequately represents the radiation yield and that the hydrodynamic profiles have evolved correctly to produce these results. However, as we shall see below that nature has conspired to mislead us to this conclusion because the plasma conditions are calculated to produce these results are very different. This is one of the unsuspected pitfalls! The transport has significantly changed the hydrodynamics to give comparable x-ray emissions.

Figure 3 isolates shot # 303 and shows a comparison between the multi-group based on a 1200 spectral lines from the full model and the non-local CRE for atomic models containing 126 and 483 radiating spectral lines, respectively. As the atomic model improves with increasing structure the yield results also improve. The experimental value is about 990 kJ's and appears midway between the diffusion and probability of escape. Once again, the pitfall is not looking beyond the yields and comparing with other experimental observations.
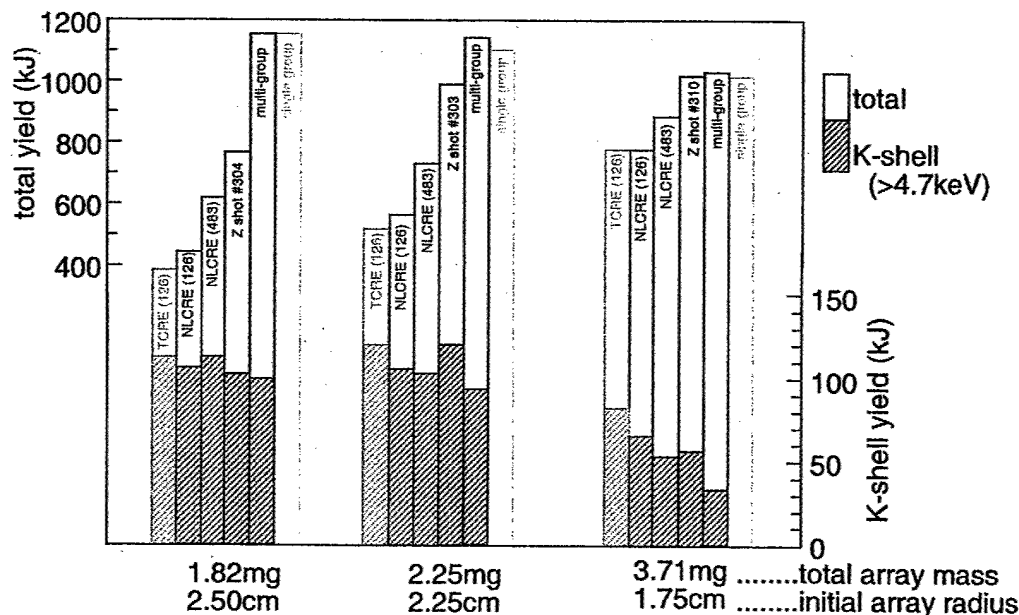
16

Figure 2. Comparison of total and K-shell yields for Ti array implosions.
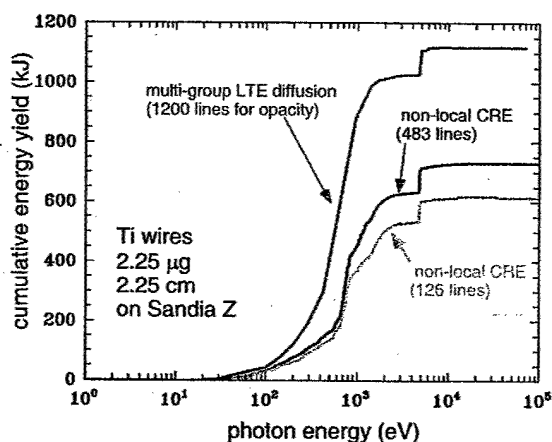

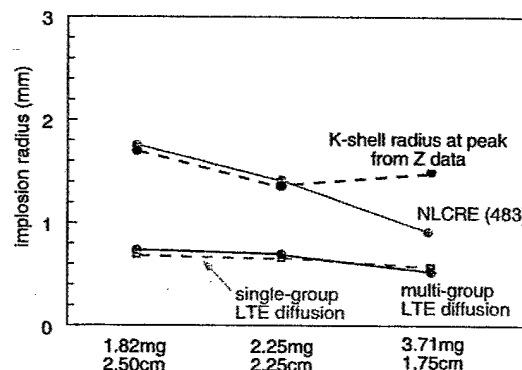Figure 3. LTE diffusion transport

Figure 4. Implosion radii

X-ray pinhole pictures provide information on the size of the emitting plasma. The experimental observations of the radius of the emitting region at peak emission are exhibited in Figure 4 along with the results of the simulations. The LTE diffusion calculations pinch down to smaller radii for all 3 loads due to the large radiative losses making it possible to compress a cooler plasma. The radii obtained in the non-LTE simulations are in better agreement with the observations in support of the other plasma properties such as temperature and density inferred from experiment. The LTE K-shell emitting radius deviates from the non-LTE estimates is difficult to understand by itself. However, one needs to compare the L-shell emitting region which occurs at larger radii and raises questions of plasma stability and a clear and concise observable radius. This

behavior will be discussed in a forthcoming paper. The main point here is that the diffusion models disagree with the observations on the size of the minimum radius.
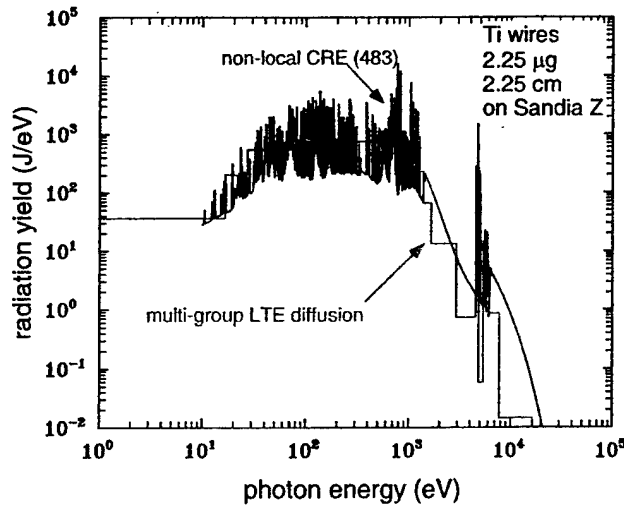

Figure 6. Ti spectra and multi-group LTE emission model

Figure 6 shows the calculated Ti spectra superposed on the LTE multi-group diffusion result. With a judicious choice of opacity groups it is possible to get a reasonable representation of the emission spectra from diffusion methods. Just how one determines the number of groups and their wavelength range potentially can be another pitfall!
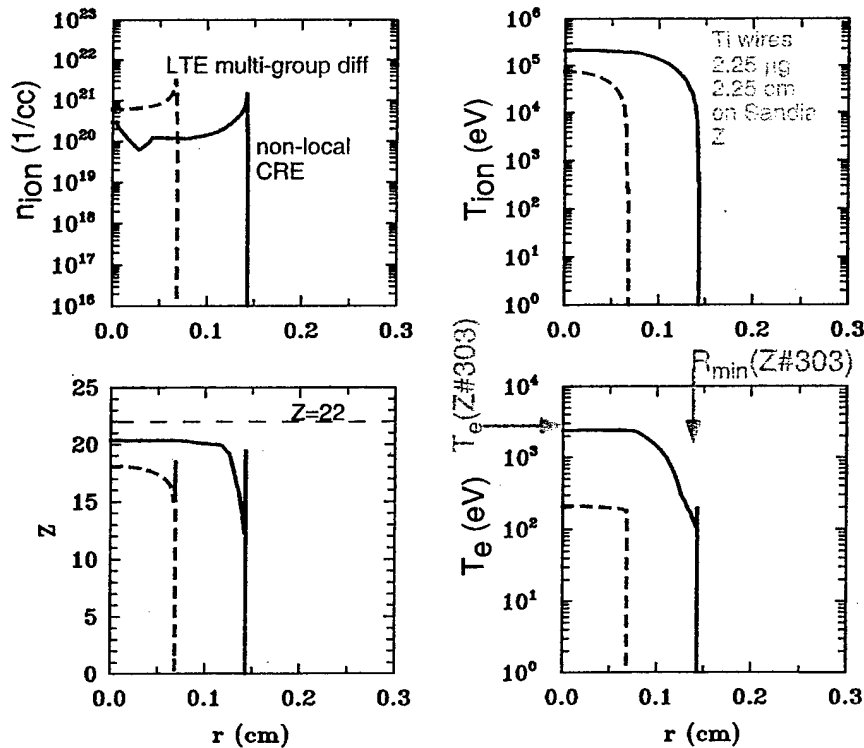

Figure 7. Hydrodynamic profiles for Ti shot #303

The hydrodynamic profiles of electron and ion temperature, average charge state and ion density are displayed in Figure 7 at about the time of peak emission. The results are self-explanatory in view of what has been stated above. The electron temperature, density and charge state can be inferred from the experimental data. The radius of the emitting region can be measured from the pinhole pictures. The comparison of these parameters with the non-LTE simulations are in good agreement. The LTE multi-diffusion hydrodynamic results are not! The LTE diffusion plasma cools at a greater rate lowering the temperature and charge state and reaching higher compressions leading to higher densities, behavior that is in contradiction to the observed measurements.

CONCLUSIONS

Modeling the radiation of Z-pinch plasmas, even for the experienced modeler focused more on the MHD phenomenology than on the radiative behavior of the plasma, oftentimes is pressured to make model choices that lead down a path of self-deception by making the code predictions agree with experiment. In the limited space provided in these proceedings we have provided some examples and consequences associated with substituting LTE multi-group diffusion methods for non-LTE and radiation transport methods in order to describe the plasmas' radiative evolution with high computational speed but low computational accuracy. The consequences result in a misinterpretation of the experimental observations and a model incapable of addressing issues relevant to the tailoring of x-ray production and of evaluating load performance. We are in the process of incorporating the non-LTE methods into multidimensional Z-pinch models to investigate how to best calculate the total and K-shell radiative yields and to evaluate the effects of plasma instabilities on x-ray production.

ACKNOWLEDGEMENTS

REFERENCES

1. Davis, J., et. al., Laser and Particle Beams, **19**, 557 (2001).
2. Thornhill, J. W., et. al., Physics of Plasmas, **8**, 3480 (2001.

A Comparison of Radiation Transport Models for a Ti Z Pinch

John L. Giuliani, Robert W. Clark, J. Ward Thornhill, and Jack Davis

Radiation Hydrodynamics Branch, Plasma Physics Division
Naval Research Laboratory, 4555 Overlook, Ave. SW, Washington, DC 20375

Abstract. One dimensional simulations of titanium (Ti) wire array Z pinches on the Z generator are compared with experimental data using four models of radiation transport: single and multi-group diffusive transport, tabulated and non-local collisional radiative equilibrium (CRE) transport. While the multi-group diffusion model can reasonably predict the total and K-shell radiative yields, there are significant discrepancies in the plasma properties at implosion between the diffusion approach and data. The present CRE models for Ti match the K-shell yield and the plasma properties, but the total yield increases with the number of emission lines transported.

INTRODUCTION

A Z pinch implosion driven by a high current generator efficiently converts mechanical energy into radiative energy. Hence the model employed to treat the radiation physics in a Z pinch simulation can affect the calculated dynamics. The most accurate model incorporates a self-consistent coupling of the ionic level populations with the radiation field through kinetic rate equations and non-local photo-processes. Such a general approach, termed the non-local collisional radiative equilibrium (NLCRE) model, is practical for a 1-D radial implosion of low atomic number plasmas ($Z<40$) [1]. In multi-dimensional simulations the predominant model in use is the three temperature approximation: ion and electron temperatures together with a radiation temperature [2,3]. The latter is calculated with a single group radiation diffusion (SGRD) equation wherein the input tabular opacities are determined from local thermodynamic equilibrium (LTE) conditions and a Planckian radiative source function is assumed. A natural extension of this approach is the multi-group radiation diffusion (MGRD) treatment which has the advantage over a single group of providing spectral content of the pinch's radiative yield. An alternative approximation for multi-dimensional simulations is the recently developed tabulated collisional radiative equilibrium (TCRE) model [4].

The objective of the present paper is to compare and contrast the radiation physics of the above four models (SGRD, MGRD, TCRE, and NLCRE) within the context of 1-D simulations for titanium (Ti) Z pinches on the Z-generator at Sandia National Laboratories. This study will briefly indicate successes and some pitfalls of the diffusion approach.

RADIATION MODELS

Both the diffusion models and the CRE models are prepared from the same Ti atomic data base composed within the Radiation Hydrodynamics Branch at NRL. For the single and multi-group diffusion approaches, the atomic level populations were determined by LTE, and the absorption coefficient included 1200 lines in all ionization stages of Ti as well as bound-free and free-free continuum processes. The multi-frequency absorption data was then averaged according to the standard formulas for single and multi-group Planck and Rosseland opacities [5]. Twenty groups were judiciously chosen to capture important spectral features, with eight resolving the K-shell emission (>4.7 keV). The standard Lagrangian 1-D hydromagnetic equations were solved along with a radiation diffusion equation for each group. An extension of a single group flux limiter [6] is applied to each group, and a Milne relation is used to specify the group radiation boundary condition at the moving outer edge of the plasma.

Details of the TCRE and NLCRE models have been described previously. We only note here that the tabular data used in the TCRE and NLCRE models have either 126 lines or 483 lines. The transport coefficients were chosen to optimize agreement with the K-shell yield from three shots on Z, vis., #303, #304, and #310. The same transport coefficients and initial grid were used in all the calculations.

TABLE 1. Results from different radiation transport models for Ti Z pinches on the Z-generator.

Z-shot #304 2.50 cm, 1.82 µg	Single group	Multi-group	TCRE (126)	NLCRE (126)	TCRE (483)	NLCRE (483)	Exp data
Total yield (kJ)	1150	1150	384	431	476	612	764
K-shell yield (kJ)	-	100	110	105	124	113	102
Z-shot #303 2.25 cm, 2.25 µg							
Total yield (kJ)	1100	1140	512	558	602	720	990
K-shell yield (kJ)	-	93	116	106	122	103	120
Z-shot #310 1.75 cm, 3.71 µg							
Total yield (kJ)	1010	1030	738	780	778	884	1008
K-shell yield (kJ)	-	32	80	66	80	53	55

RESULTS AND DISCUSSION

The total yields, K-shell yields, and implosion radii are given in Table 1 for various radiation models along with the corresponding experimental data [7]. The model results for the total yield are taken after the first bounce while the same yield from the experiments is determined from the product of the peak power and the FWHM. The SGRD and MGRD models give very similar total yields, which exceeds the observed

value at the low mass shot, but equals it for the high mass one. Both the TCRE and NLCRE models give too little total yield, but one can see an increase in the total yield for both models as the number of transported emission lines (number in parentheses) increases. This indicates that the L-shell radiation in the CRE models depends upon the number of emission lines transported in the calculation.

The K-shell yields for all the models, except SGRD, are fairly accurate, within a factor of two of the experimental results. The largest variation occurs for the high mass case where MGRD is too low and the TCRE results are too large. An estimate of the K-shell yield for the SGRD models was made by considering the emission at each time to be the Planck function at the radiation temperature of the outer zone. The result was less than a joule for each mass. The origin of the K-shell emission in the MGRD models is deep inside the plasma. Such high energy radiation groups are optically thin and nearly free stream outward to the plasma surface.
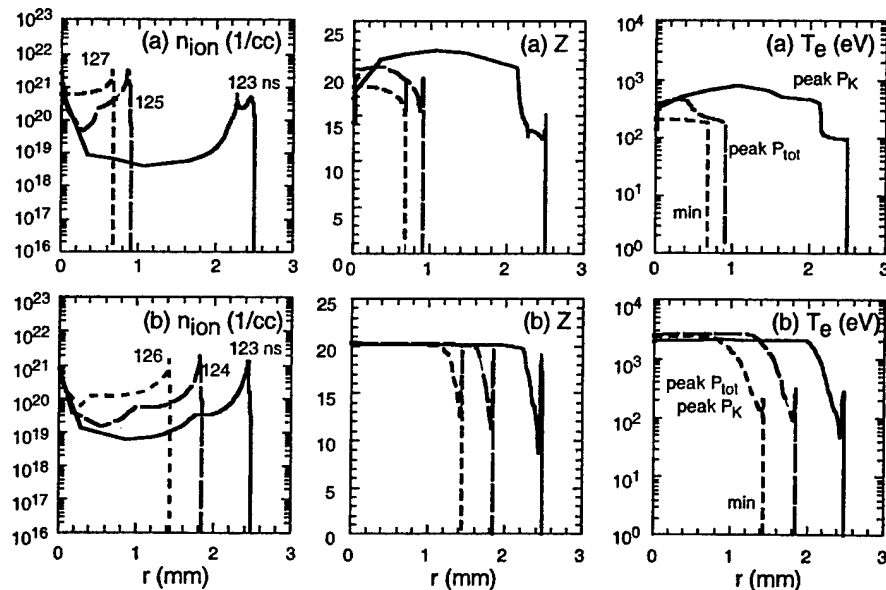

FIGURE 1. (a) Profiles of the ion density, mean charge state, and electron temperature at the time of peak K-shell power (123 ns), the time of peak total power (125 ns), and the minimum radius (127 ns) for the MGRD model. The initial radius of the Ti wire array was 2.25 cm and the total mass is 2.25 mg. (b) The same quantities for the NLCRE(483) model at similar times. The peak total and K-shell power occur at the minimum radius.

The agreement in the gross radiation features between the diffusion results and the experiments does not follow through to the dynamic features. We note four problems with the LTE radiation diffusion models. Simulation results of the pinch dynamics at three times near the implosion are displayed in Fig.1 for the intermediate mass case. First, the minimum radius of the MGRD model is about half that of the NLCRE model, which is close to the observed value of 1.4 mm [7]. This high compression ratio (~30) is typical for the diffusion treatments of radiation, and it explains the large total yields obtained with such models: a deep implosion translates to more magnetic

work done on the pinch, which in turn is efficiently radiated by an LTE plasma with a Planckian source function. Second, the electron temperature, T_e, is smaller in the MGRD model than for the NLCRE one, especially at the minimum radius. Analysis of experimental data of wire arrays on the Z generator [8] indicate $T_e \sim 3000$ eV, again closer to the NLCRE result. Third, the rapid decrease in T_e in the MGRD implosion predicts that the peak K-shell emission occurs prior to that of the total power. This is opposite to the observed relation [8]. Finally, the same change in T_e causes the mean charge state, Z, to rapidly decrease over ~ 1 ns due to the LTE condition. This is unphysical as the dominant recombination process under these pinch conditions (dielectronic) gives a time scale of >10 ns for Ti to recombine from hydrogen to helium-like.

In conclusion, the total yields from the 1-D diffusion models follow from the large compression ratio and the subsequent conversion of a large coupled magnetic compression energy to radiation. We found that the TCRE model fairly well matched the NLCRE results, including the density, Z, and T_e profiles, though it is 3 to 4 orders of magnitude faster in run time. It is remarkable that the MGRD model reproduced the K-shell yields of the NLCRE model to within a factor of two, given that the plasma conditions of T_e and Z are so disparate from the CRE results. The K-shell yields for the MGRD model result from compensating effects. For a given T_e, the ionization level for LTE is higher than for CRE, and the amount of K-shell emission would be excessive except that the assumption of a Planckian source function leads to strong radiative cooling and a low T_e compared to the CRE model.

ACKNOWLEDGMENTS

REFERENCES

1. Davis, J., Clark, R., Blaha, M., and Giuliani, J.L., *Laser and Particle Beams*, 19, 557-577 (2001).
2. Peterson, D.L., Bowers, R.L., Brownell, J.H., Greene, A.E., McLenithan, K.D., Oliphant, T.A., Roderick, N.F., and Scannapieco, *Phys. Plasmas*, 3, 368-381 (1996).
3. Douglas, M.R., Deeney, C., Spielman, R.B., Coverdale, C.A., Roderick, N.F., Haines, M.G., *Phys. Plasmas*, 7, 2945-2958 (2000).
4. Thornhill, J.W., Apruzese, J.P., Davis, J., Clark, R.W., Velikovich, A.L., Giuliani, J.L., Chong, Y.K., Whitney, K.G., Deeney, C., Coverdale, C.A., Cochran, F.L., *Phys. Plasmas*, 8, 3480-3489 (2001).
5. Mihalas, D., and Mihalas, B.W., *Foundations of Radiation Hydrodynamics*, Oxford University Press, New York, 1984, pp.363-365.
6. Levermore, C.D., *J. Quant. Spectrosc. Radiat. Transfer*, 31, 149-160 (1984).
7. Denney, C., private communication.
8. Deeney, C., C.A. Coverdale, Douglas, M.R., Nash, T.J., Spielman, R.B., Struve, K.W., Whitney, K.G., Thornhill, J.W., Apruzese, J.P., Clark, R.W., Davis, J., Beg, F.N., Ruiz-Camacho, J., *Phys. Plasmas*, 6, 2081-2088 (1999).

K-shell Yield Performance Assessment of Argon Gas Puff Loads Imploded on Double Eagle, Z, and Decade Quad

J. W. Thornhill,[a] J. P. Apruzese,[a] J. Davis,[a] A. L. Velikovich,[a] K. G. Whitney,[b] H. Sze,[c] J. S. Levine,[c] B. Failor,[c] C. Deeney,[d] C. A. Coverdale,[d] and D. Bell[e]

[a]Radiation Hydrodynamics Branch, Plasma Physics Division, Naval Research Laboratory, Washington, DC 20375 USA
[b]Berkeley Scholars, Inc. Springfield, VA 22150 USA
[c]Titan Systems Corp., Pulse Sciences Division, 2700 Merced Street, San Leandro, CA 94577
[d]Sandia National Laboratories, Albuquerque, NM 87185 USA
[e]Defense Threat Reduction Agency, Alexandria, VA 22310-3398

Abstract. The K-shell yield performance of Titan double-shell argon gas puff loads imploded on the Z machine and Decade Quad (DQ) is compared to the performance of Double Eagle loads employing the same nozzle configuration. Specifically, the K-shell yields obtained on the Z and DQ machines are compared with I^4, I^2, and I^0 current scaling projections made from Double Eagle yields, where I is the peak load current. This analysis allows initialization and multidimensional effects to be factored out of the scaling behavior. This projection analysis is useful for evaluating argon gas-puff load performance because it relates I^4, I^2, and I^0 K-shell yield scaling transitions that a load, of a given specific energy, is predicted to undergo as the total load mass increases. Our analysis shows that the maximum K-shell yields were near optimum for the nozzle configuration used and the energy coupled to the load in the Z and Decade Quad experiments. At present it is not understood why an additional 22 nh of inductance for DQ, 6 nh for the Z machine, and 8 nh for Double Eagle is required in their respective equivalent circuit models to reasonably match measured peak currents and implosion times. Note, we do not think that there is extra inductance in the real circuit; it is included in the modeled equivalent circuit as a method to account for the possible anomalous effects that are reducing the current from its expected value. These effects may include: multidimensional effects, current losses, and anomalous resistivity.

INTRODUCTION AND REVIEW OF I^2 AND I^4 YIELD SCALING

In this work we examine the performance of Titan 4-3-2-1 nozzle argon loads on the Z machine and Decade Quad (DQ) relative to their performance on Double Eagle (DE). This nozzle is a double puff design with gas flowing from two concentric annuli (outer annulus located between 4 cm and 3 cm radius, inner annulus between 2 cm and 1 cm radius).[1,2] The K-shell yields obtained on Z and DQ are compared with I^0, I^2, and I^4 scaling projections from DE K-shell yields for implosions having the same implosion velocities, mass distribution, pinch length, and cathode recession. Because the loads are so similar this scaling analysis automatically excludes scaling effects resulting from different initialization and multidimensional effects. This allows load

performance to be evaluated entirely in terms of its current scalings from its performance on DE. The DQ and Z experiments are analyzed in the context of three physics based scaling trends, which are: (1) I^4 scaling, which is valid in the low mass regime because radiation rates there increase at their optically thin density squared rates, (2) since energy inputs increase as I^2, at large enough load mass energy conservation requires that K-shell yields asymptote to an $I^{\leq 2}$ scaling, and (3) total radiation rates often increase with mass faster than ionization and thermalization rates such that radiation losses cool the plasma faster than it can be heated and ionized resulting in either a fall off or in I^0 saturation of K-shell yield. Trend (3) especially occurs for low specific energy ($\eta^* < 2$) implosions because they barely have enough energy to ionize into and radiate from the K-shell.[3] η^* is defined as the J×B coupled energy-per-ion normalized by $E_{min} \cong 1.012\ Z^{3.662}$ eV/ion, the minimum energy needed to instantly heat and ionize into the K-shell.[4] Conversion efficiencies of 20-30 percent of J×B energy into K-shell emission are calculated in the I^2 regime for high specific energy ($\eta^* > 4$) implosions. [4] These efficiencies have been achieved experimentally for plasmas with atomic numbers as high as Z=18.

The DE experimental yields from which scaling projections to DQ and Z are performed are shown as a function of experimental implosion time (τ) which depend on the load mass that the measured peak values of current in Fig. 1 can implode. These results are taken from Ref. [1]. The I_{peak} curve shown in Fig. 1 required that an additional 8 nh of inductance be included in the circuit model in order to obtain a reasonable fit to the measured peak current values as a function of τ. The inferred η^* and mass curves of Fig. 1 are based on this circuit model. The inferred masses are close to the values listed in Ref. [1]. The DE K-shell yields are projected for DQ along I^α scaling curves using,

$$Y^{I^\alpha}(\eta^*) = Y_{DE}(\eta^*) \times \left(\frac{I_{DQ}(\eta^*)}{I_{DE}(\eta^*)} \right)^\alpha \qquad \text{for fixed } \eta^* \text{ and } \alpha = 0, 2, 4 \qquad (1)$$

An I^0 yield projection implies that the K-shell yield is saturated at the DE K-shell yield. Likewise, an I^2 {I^4} projection implies that the yield is increasing in proportion to the ratio of the J×B {(J×B)^2} energy from the DQ pinch to that from DE.

ANALYSIS OF DQ AND Z EXPERIMENTS

Figs. 2 and 3 show the results for the DQ experiments in which the voltage was reduced by the factor 0.7/0.85. Fig. 2 demonstrates that adding 22 nh to the DQ circuit produces a reasonable match with the measured peak current values as a function of τ. The masses and η^* values that are inferred from this circuit as well as the calculated peak current, without any additional inductance, are also shown in Fig. 2. This figure indicates, for a fixed τ, that the measured peak current values are about 1 MA below their expected values (no extra 22 nh). This represents approximately 30 percent less energy coupled to the load than expected. The I^α K-shell yield scaling projections are shown in Fig. 3. This figure illustrates that the 244 ns implosion was in a saturated, I^0, scaling regime. In other words, at this low level of η^* ($\eta^* \cong 1.7$), as the mass is

increased from 150 µg/cm on DE to 260 µg/cm on DQ, the total radiation rates have increased with mass and cooled the plasma to the extent that it is difficult to ionize to and radiate from the K shell. Thus, increasing the mass beyond 260 µg/cm at $\eta^* \leq 1.7$ will not produce any additional K-shell emission. As the mass is reduced and correspondingly η^* is increased (230 ns shot), the DQ K-shell yield approaches an I^2 scaling projection in which the K-shell yield is increasing in proportion to the coupled energy. The conversion efficiency of coupled energy to K-shell emission is about 12 percent for this shot, which is reasonable for this relatively low $\eta^* \cong 2$ implosion. Fig. 3 demonstrates that it is futile to attempt to optimize K-shell emission in future experiments by operating with this nozzle configuration with mass loads in excess of 200 µg/cm having η^* values less than 2. However, an encouraging consequence of the I^2 scaling achieved for the 230 ns experiment (mass $\cong$ 200 µg/cm) is that loads of less than 200 µg/cm that are imploded at η^* values greater than 2 can be expected to be in an $I^{>2}$ scaling regime. This consequence was verified by the DQ shot at full voltage. The 28 kJ of K-shell emission achieved by this shot (not shown) lie between I^2 and I^4 scaling projections. It is about 18 percent of the J×B energy.

The Z machine results for 2.4-cm length experiments are displayed in Fig. 4. The experimental results shown in this figure are taken from Ref. [2]. An additional 6.0 nh in the circuit model was required to reasonably match the measured peak currents with their respective implosion times (not shown). The inferred masses (Fig. 4) are also in agreement with those in Ref. [2]. The peak current calculated with extra inductance is 2-3 MA lower than that calculated without extra inductance. This represents about a 30 percent reduction in J×B energy for a given τ. Neither the DQ nor this current reduction is presently understood. Figure 4 illustrates how the yield behavior changes from nearly saturated, I^0, at the higher mass and lower η^* values of the 135 ns shot, to yields that are clearly in excess of I^2 projections from DE as the mass is reduced and the η^* values correspondingly increased. The K-shell yield for the lowest mass shot (800 µg/cm, η^*=5.5, τ=112 ns) is so large that it begins to approach typical theoretical values of 30 percent of the J×B coupled energy.

CONCLUSIONS

This analysis shows that the Titan nozzle's K-shell yield performance on Z and DQ is in accord with established current scaling trends from its performance on DE. It also shows that the efficiency of converting J×B energy to K-shell emission increases with implosion velocity for this configuration, i.e. the maximum conversion efficiency for an $\eta^* \leq 2$ load is about 12 percent whereas for an η^*≅5.5 it is at least 27 percent. At present it is not understood why DQ, Z and DE require additional inductance in their respective equivalent circuits (22 nh for DQ) to obtain a reasonable match between measured peak currents and implosion times. In addition to understanding and improving power flow, another option for achieving higher argon K-shell yields on DQ is to implode loads from larger radius, which will allow more energy to couple to the load at higher specific energy.
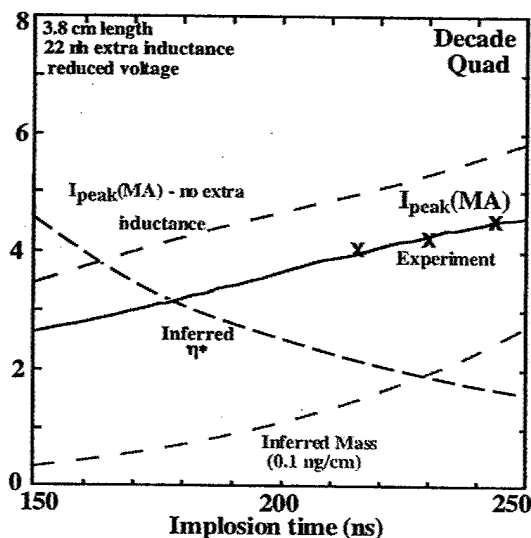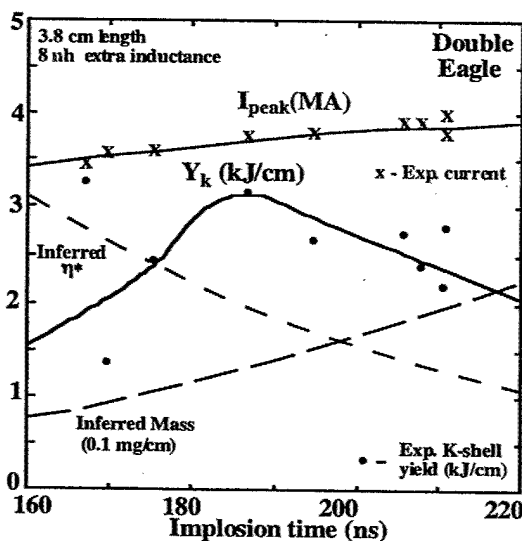
Figures 1 and **2.** Double Eagle and Decade Quad experimental peak currents as a function of experimental implosion time. Also shown are inferred mass loads, η* values, and calculated peak currents. In **Fig. 1** the experimental K-shell yields are shown as a function of implosion time.
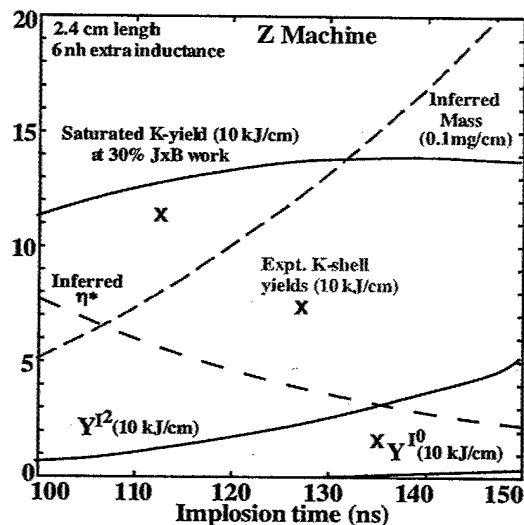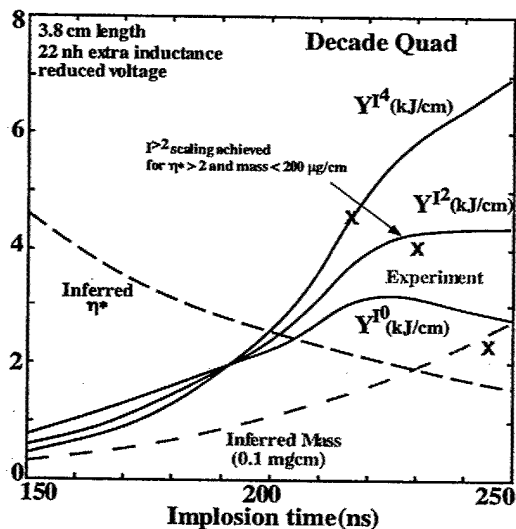
Figures 3 and **4.** Comparison of Decade Quad and Z machine experimental K-shell yields as a function of implosion time with I^0, I^2, and I^4 scaling projections from Double Eagle K-shell yields. Also shown are inferred mass loads and η* values.

ACKNOWLEDGMENTS

REFERENCES

1. H. Sze, P. L. Coleman, B.H. Failor, A. Fisher, J. S. Levine, et al., *Phys. of Plasmas* **7**, 1 (2000).
2. H. Sze, P. L. Coleman, J. Banister, B. H. Failor, A. Fisher, J. S. Levine, et al., *Phys. of Plasmas* **8**, 3135 (2001).
3. J. W. Thornhill, K. G. Whitney, J. Davis, and J. P. Apruzese, *J. Appl. Physics* **80**, 710 (1996).
4. K. G.Whitney, J. W. Thornhill, J. P. Apruzese, and J. Davis, *J. Appl. Phys.* **67**, 1725 (1990).

Cooperative Relaxation Methods for Multigroup Radiation Diffusion in Radiation Hydrodynamics

R. E. Terry*, J. L. Giuliani* and J. P. Apruzese*

*Radiation Hydrodynamics Branch, Plasma Physics Division Naval Research Laboratory, Washington, DC 20375 USA

Abstract. With restrictive Courant criteria, the time integration of a radiation diffusion equation is generally done by a fully or partially implicit method. Relaxation methods are often effective and *cooperative relaxation* refers to a technique that will diffuse each spectral radiation group as a separate operation and combine the changes to a full spectrum. Successive passes over the groups provide convergence, as well as conserving energy over time, space and spectrum. Linearized and fully nonlinear variations on the method are discussed.

INTRODUCTION

Diffusion may offer a reasonable approximation for x-ray radiation transport when optical depths are large, high atomic number species are involved, and populations are in local thermodynamic equilibrium (LTE). In fast Z-Pinch events these criteria are not well met for energetic radiation but may be satisfied for lower energies, higher Z elements, or cooler, denser regions. A multigroup diffusion theory affords the numerical radiation hydrodynamics model a measure of flexibility in tracking the domains of space and spectrum where diffusion is valid, as well as a means to isolate those domains where an alternate transport method must replace it.

Rosseland Courant numbers increase quadratically with smaller mesh sizes and as power laws with higher electron temperatures, hence a time integration of the radiation diffusion equation is generally done by an implicit method. The fully implicit methods developed here are tailored to radiation hydrodynamic codes (like Mach2[1]) where direct matrix inversions are incompatible with the range of geometries and grid options available. Here relaxation methods are required and offer the same quality of numerical performance as direct methods, without the requirement to specify a globally connected mesh. Moreover a relaxation method offers the ability to change easily from diffusion to thin emission or detailed transport on some spatial and spectral domains while retaining the diffusive method where it remains viable.

Cooperative relaxation, as discussed here, refers to a technique that will diffuse each spectral radiation group as a separate operation but combine the changes into a "provisional" full spectrum at the forward time level. Successive passes over the groups then provide convergence on the final spectrum, conserving energy over time, space and spectrum to machine precision. The method is also manifestly compatible with a Milne or free surface boundary condition[2]. Two variations are discussed — linearized and fully nonlinear in the T^4 dependence of the radiation source term.

28

MATHEMATICAL FORMULATION

The radiation diffusion approximation for transport in a material characterized by a Rosseland mean opacity κ_R, and a Planck mean opacity κ_P, is often expressed in terms of the variables $u_R = aT_R^4$, which represents the radiation field energy density, and $u_e = aT_e^4$ the corresponding energy density at the ambient electron temperature. Here $a = 4\sigma/c = 137.18$ [erg/cm^{3}eV^4].

When a multi-group formulation is used then Rosseland and Planck opacities extend over the domain of frequency groups [k]. The equivalent transport relationship for each group $[u_k, \kappa_{R,k}, \kappa_{P,k}]$ is written in plane or cylindrical geometry (p=0,1) as:

$$\frac{1}{c}\left(\frac{Du_k}{Dt} + u_k\nabla\cdot\mathbf{V}\right) - \frac{1}{r^p}\partial_r\left(\frac{r^p}{3\kappa_{R,k}}\partial_r u_k\right) - \partial_z\left(\frac{1}{3\kappa_{R,k}}\partial_z u_k\right) = \kappa_{P,k}(u_{e,k} - u_k), \quad (1)$$

with the source term $u_{e,k} \equiv F_k aT_e^4$ such that the fractions F_k sum to one $\forall(t,r,z)$. These fractions are readily computed from Debye functions of T_e. As written the opacities are mass normalized, viz. $1/\kappa_{P,R} \equiv \lambda_{P,R}$, the mean free path; thus $c\lambda_{R,k}/3$ is a group radiation conductivity dependent on ρ and T_e. With $h_e = \rho C_V T_e$, the internal energy couples to the radiation according to $\partial_t h_e = -\Sigma_k \partial_t u_k$, constraining the changes in u_k.

COOPERATIVE RELAXATION OF RADIATION GROUPS

The partial differential equations above are easily recast in terms of dimensionless operators on a space scale ℓ_0 and time scale t_0. The diffusion and energy exchange processes are then measured by Courant numbers $C_k \equiv ct_0\lambda_{R,k}/3$ and $K_k \equiv ct_0\kappa_{P,k}$. The divergence of the flux at any solution point $u_{0,0}$ can always be represented by $\nabla\cdot\Gamma_{0,0} \approx B\,u_{\pm b,\pm b} - D\,u_{0,0}$, where b is the "bandwidth" of the spatial differencing.

First, we set the definitions $K_k = cdt\,\kappa_{P,k}$, $\bar{\kappa}_P = \Sigma_k\,\kappa_{P,k}\,F_k$, $R_k = 1 - F_k\frac{\alpha\beta}{1+\alpha\beta}\,(\kappa_{P,k}/\bar{\kappa}_P)$, $\alpha = cdt\,\bar{\kappa}_P$ and $\beta = 4a\,^nT_e^3/\rho\,C_V$. The variable β embodies the optional linearization of the electron temperature equation based on the current ("nth") time level. We further denote $S \equiv \Sigma_l(\kappa_{P,l}/\bar{\kappa}_P)\,u_l$ and $\tilde{S}_k \equiv \Sigma_{l\neq k}(\kappa_{P,l}/\bar{\kappa}_P)\,u_l$.

Implicit Differencing — Linearized Method. When fully implicit, particularly with the C_k evaluated at the forward time level, the resulting time difference scheme is similar to the Crank-Nicholson method. The RHS contains the band portion, B; the LHS, the diagonal portion, D. The complete difference scheme for Eqn (1) as tested in the following discussions is thus stated (without proof) as,

$$^{n+1}u_k[1 + K_kR_k + {}^{n+1}D] = {}^n u_k + {}^{n+1}B + K_k F_k\cdot\left\{\frac{{}^nu_e + \beta\alpha({}^{n+1}\tilde{S}_k)}{(1+\alpha\beta)}\right\}. \quad (2)$$

The forward time level temperature is updated directly from the energy conservation rule using the accumulated $\nabla\cdot\Gamma_k$ based on the "n+1 th" time level. This procedure

29

is demonstrably superior when dealing with transients in such a stiff energy exchange system as contained here. In particular, the new temperature is given by

$$^{n+1}T_e = {}^n T_e + \Sigma_k \left\{ \frac{^{n+1}\nabla \cdot \Gamma_k - (^{n+1}u_k - {}^n u_k)}{\rho C_V} \right\} . \qquad (3)$$

Let $^*S$ be the measure of general spectral convergence in any spatial location, then the *cooperative relaxation* method begins by making the *initial* substitution $^*u_l \approx {}^n u_l$ or $F_l^n u_R$ for $^*u_l$ in the source $^{n+1}\bar{S}_k$ for the groups at the n+1 time level. When the fractional changes in ^{n+1}S are sufficiently small with each iteration, the forward electron temperature and the radiation groups are regarded as converged to a "fixed point" and the time step is complete. This formulation affords excellent energy conservation.

Implicit Differencing — Fully Nonlinear Method. Using $\gamma \equiv a/(\rho C_V)^4$, we can use $h_e = \rho C_V T_e$ rather than u_e as the fundamental thermal energy. Now, with $^{n+1}u_k$ and $^{n+1}h_e$ fully coupled through ^{n+1}S, the equivalent forms to Eqns. (2) and (3) become

$$^{n+1}u_k[1 + K_k + {}^{n+1}D] = {}^n u_k + {}^{n+1}B + K_k F_k \cdot \{\gamma^{n+1}h_e^4\} \qquad (4)$$

and

$$^{n+1}h_e = \left(\frac{^n h_e + \alpha\, {}^{n+1}S}{1 + \alpha\gamma\, {}^{n+1}h_e^3} \right) . \qquad (5)$$

TESTING THE METHODS

On a rectilinear uniform mesh we have examined the excitation of nonlinear Marshak like waves, c.f. Figure 1. The initial disturbance below is a pulse in T_e, but a pulse in u_R behaves similarly. The background cold gas is Ar at a pressure of 10x standard conditions. A power law opacity model is used with a fixed, cold gas value for C_V.

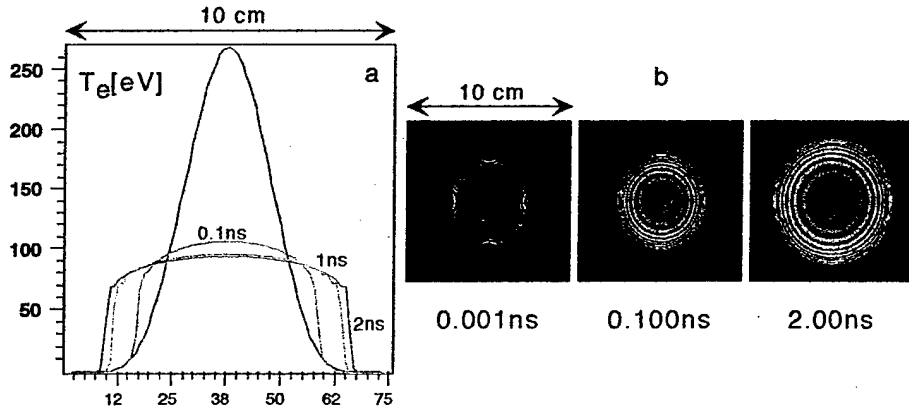
Figure 1. (a) Central cuts of the electron temperature profile, with cell locations shown; (b) corresponding 2D intensity plots of the 20 —245 eV radiation.

TABLE 1. Spatial Diffusion: Iterates for convergence to various tolerances and the corresponding number of spectral sweeps required.

$\|\delta u_k/u_k\| \approx$ grid $\|C_{max}$	10^{-6} per group	10^{-9} per group	10^{-12} per group	10^{-15} per group	Group Sweeps $\|\delta S/S\| < 5\,10^{-9}$
30x30	0.05	-	4	5	7	12*
30x30	0.50	-	4	5	7	74*
30x30	0.159	-	18	25	30	15
50x50	0.5	-	13	20	26	14
75x75	1.11	-	11	17	20	6
75x75	5.57	5	12	15	22	12
75x75	27.76	17	31	108	-	35

* nonlinear method

The 20 —245 eV radiation band shown is strongest in peak intensity for the sample at 0.1 ns. The electron temperature profile generally follows the spread of the lowest energy band (0 —20 eV). While these radiation waves do not hold a constant speed as they expand and are forced to heat an ever larger volume of gas, they share with Marshak waves the property that a stronger initial disturbance produces a faster moving wavefront. The late time profiles of the electron temperature and radiation energy density in all surviving radiation bands also appear to lock onto a self-similar shape. The example shown was done with the linearized model, but the fully nonlinear one will give similar results under similar conditions. As also shown in Table 1, an increase in the peak Rosseland Courant number by a factor of order 10 for either method will increase the number of group sweeps by a lesser factor. Similarly, adding groups at fixed convergence parameters will not increase the number of sweeps significantly, if at all. In these cases energy conservation errors over time, space, and spectrum were down to machine precision.

We have demonstrated a class of energy conserving, multigroup relaxation methods compatible with radiation hydrodynamic codes and free surface boundary conditions. The resolution of self-similar radiation waves has provided a baseline test suite.

Acknowledgements

REFERENCES

1. R. E. Peterkin, M. H. Frese, C. R. Sovinec *JCP*, **140** 148 (1998).
2. R. E. Terry, J. L. Giuliani, *IEEE TRANSACTIONS ON PLASMA SCIENCE*, **30** 2 (April 2002).

Modeling Enhanced Energy Coupling of Z-pinches to Pulsed-power Generators

K. G. Whitney,[a] J. W. Thornhill,[b] C. Deeney,[c] C. A. Coverdale,[c] J. P. Apruzese,[b] J. Davis,[b] A. L. Velikovich,[b] and L. I. Rudakov[a]

[a]*Berkeley Scholars Assoc., P. O. Box 852, Springfield, VA 22150 USA;* [b]*Radiation Hydrodynamics Branch, Plasma Physics Division, Naval Research Laboratory, Washington DC 20375 USA;* [c]*Sandia National Laboratories, P. O. Box 5800, Albuquerque, NM 87185 USA.*

Abstract. It has been observed over the years that the energy coupled to the load in many z-pinch experiments is larger than can be accounted for by the sum of the **jxB** work and classical Ohmic heating. Moreover, this energy enhancement appears to be a function of the generator design, increasing as the risetime of the current is increased. In recent experiments on the Saturn generator, for example, which was operated at current risetimes in excess of 160 ns, observed energy enhancements were factors of 2 to 4 times the energy input expected from JxB work alone. When Saturn operates with risetimes of less than 90 ns, much smaller energy enhancements over the JxB energy are seen. In the past, it was conjectured that some form of anomalous resistivity was needed to account for the extra energy input, while recently, a new idea was proposed based on the buildup of internally generated tubes of magnetic flux energy.[1,2] It was hypothesized that the growth of the Rayleigh-Taylor instability at the surface of the z-pinch plasma would generate bubbles of magnetic flux-tube energy that deposit their energy in the plasma at a current-to-the-third-power rate. While 0-D modeling of the Saturn experiments shows that an anomalously high load resistance can input the required energy needed to match the x-ray data, an alternate mechanism than magnetic flux-tubes exists for anomalous heating that is based on the production of micro-instabilities at the pinch surface. Both this and the flux-tube model are phenomenological and require guidance from experiments to be implemented. Several issues that arise from these enhanced energy coupling mechanisms are discussed in this paper.

SATURN EXPERIMENTS

Various aluminum array shots in which the load mass, the array length, and the array radius were varied were carried out on the Saturn generator at Sandia National Laboratories. In these experiments, Saturn was operated with current risetimes that varied between 140 to 230 ns depending on the load parameters. In all these experiments, large amounts of x rays were emitted. Generally, the total energy radiated was 2 to 4 times the energy imparted to the load by the **jxB** forces. Consequently, for a calculation to produce this much x-ray energy, it must impart in excess of this amount to the plasma by means that go beyond the conventional hydrodynamic modeling and that are generally considered to originate from some form of anomalous plasma heating.

The two total x-ray output pulses that are shown in Fig. 1 illustrate the variable nature of this added energy input. These pulses were generated in two shots that had identical load parameters: 180 wires of 2 cm length initially at a radius of 2 cm with a load mass of 616 μg/cm. The x-ray pulse from shot 2693 had a peak power approximately twice that of shot

2636. Moreover, shot 2693 had a late-time foot that followed the main pulse while shot 2636 did not. Fig. 2 contains two running time integrations of the power curves in Fig. 1. They show that the energy radiated in the main pulse was approximately the same in each shot -- roughly 500 kJ. However, a significant amount of late-time emission occurs in shot 2693 (~700 kJ), which is absent in shot 2636. For these energies to be radiated from the pinch, they must be supplied to it over the two, very different, time intervals of the emission. If the pinch is regarded as a dynamic circuit element having both a time dependent resistance, $R_{load}(t)$, and a time dependent inductance, $L_{load}(t)$, then this energy is supplied either through L-dot work or through resistive heating with the late-time emissions coming from late-time resistive heating.
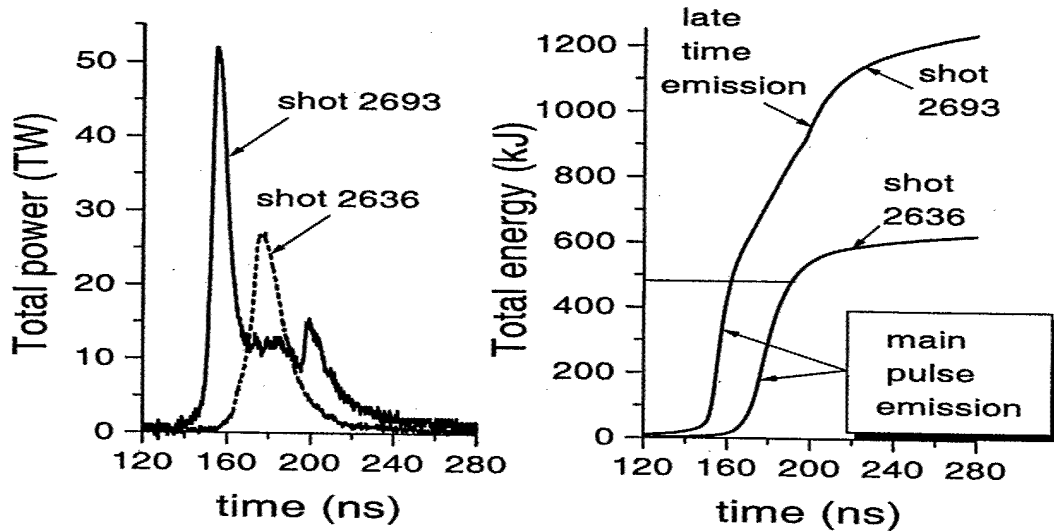
FIGURES 1 AND 2. The total x-ray power pulses for shots 2693 and 2636 are shown in the first figure and their running time integration in the second.

0-D COUPLING

The simplest way to model the L-dot and resistive heating energetics of shots 2636 and 2693 is to use a 0-D kinetics model of the load that is coupled to the circuit model for Saturn appropriate to its long current-risetime mode of operation. In this case, the load inductance, L_{load}, is given by $L_{load}(t) = (2\ell/c^2)\ln(r_{rc}/b(t))$, where ℓ is the length of the pinch, r_{rc} is the radius of the return current path, and $b(t)$ is the location of the outer boundary of the imploding pinch as a function of time. The energy equation of the circuit in a 0-D model describes the buildup of magnetic field energy, kinetic energy, and Ohmic heating by the discharge of the generator:

$$\frac{d}{dt}\left(\frac{1}{2}L_{gen}I^2 + \frac{1}{2}L_{load}I^2\right) + \left(R_{gen} + R_{load} + \frac{1}{2}\frac{dL_{load}}{dt}\right)I^2 = V(t)I(t),$$

where the dL_{load}/dt resistive term in this equation corresponds to the build-up of kinetic energy in the load:

$$\frac{d}{dt}\left(\frac{1}{2}m\ell\left(\frac{db}{dt}\right)^2\right) = \frac{1}{2}\frac{dL_{load}}{dt}I^2.$$

In these equations, m is the mass per unit length of the z-pinch load, $L_{gen} = 11.8$ nH is the generator inductance, $R_{gen} = 0.068$ Ω is the generator resistance, and $V(t)$ is the voltage drive of the Saturn generator. These equations are solved for b and the current, I. In calculations with these equations, dL_{load}/dt is obtained from b and db/dt, while $R_{load}(t)$ must be specified.

Solutions to 0-D equations can be used to determine energy inputs to loads only during the implosion phase of the dynamics. Hence, these energies can only be compared to total energies radiated during the main x-ray pulse. Some guidance for specifying R_{load} is provided in Ref. [3]. In sub-mega-ampere experiments, the load resistance was observed to grow rapidly to a maximum value late in the implosion. The calculations of the Ohmic and kinetic energy inputs to different massed loads, which are shown in Fig. 3, were guided by these experiments. The load resistance was turned on rapidly during the run-in to the maximum values that are shown in the figure prior to the termination of the implosion at a radius of 1.5 mm. The implosion calculations were begun at a radius of 2 cm.
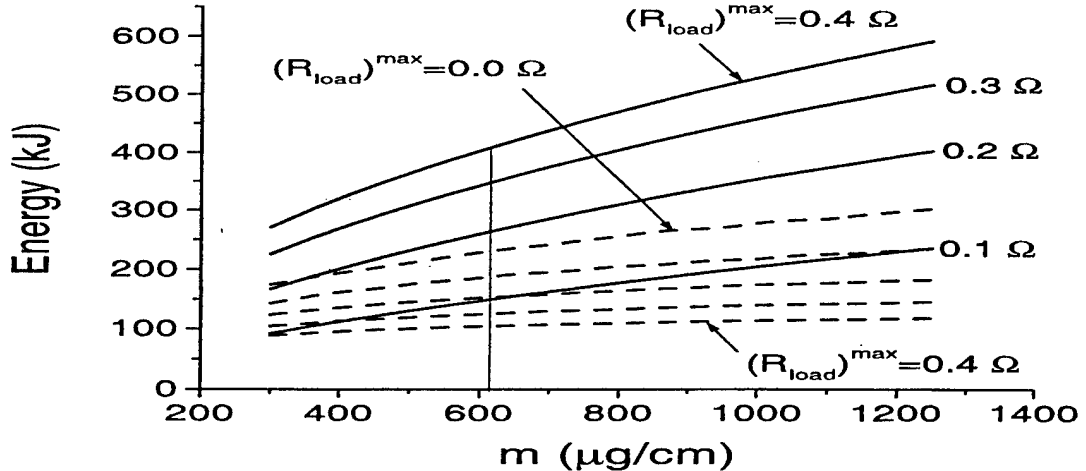

FIGURE 3. The kinetic and Ohmic energies imparted to different massed loads during the implosion phase of the z-pinch dynamics are shown for four values of the maximum load resistance. The dashed curves are kinetic energies and the solid curves, Ohmic energies. As the load resistance is increased, the kinetic energy generated in the implosion progressively decreases.

34

As seen in these 0-D calculations, the kinetic energy generated during implosion for the 616 μg/cm load, when there is no load resistance, accounts for only half of the energy radiated during the main x-ray pulses of shots 2636 and 2693; a load resistance peaking at values in excess of 0.4 Ω is needed to impart the necessary energy. Moreover, as the load resistance is increased, the amount of kinetic energy generated during implosion goes down. Both Ohmic and kinetic energy inputs to the load increase as the load mass, and consequently the load implosion time, is increased. This behavior as load mass is increased was also seen in the x-ray outputs of the Saturn shots shown in Table 1 in which only the load mass was varied.

Table 1 Variable Mass Experiments

Shot #	Array Mass (μg/cm)	Implosion Time (ns)	Total X-ray Output (kJ)	Total X-ray Output (main pulse) (kJ)
2640	328	134	777	334
2636	616	175	629	458
2637	887	183	736	382
2641	1050	184	845	546
2702	1576	208	1040	652

1-D AND 2-D COUPLING

Since Spitzer resistivity is too small to account for the Ohmic heating needed to produce the energy outputs (and thus the required energy inputs) seen in the Saturn experiments, two ways have been proposed for increasing the resistivity of a z-pinch load. One, proposed in Refs. [1] and [2], involves the generation of added amounts of magnetic field energy within the pinch plasma that is decoupled from the load inductance. The process by which this energy is generated is proposed to be related to the generation of Rayleigh-Taylor instabilities at the surface of the pinch. The subsequent dissipation of this magnetic field energy within the plasma then adds resistivity to the pinch. However, there is also a second mechanism for producing anomalous resistivity in a pinch. It occurs by way of micro-instability generation at the pinch surface.

An expression for R_{load} in terms of the surface micro-instability resistivity can be derived by calculating the power flow at the termination of the transmission line into the z-pinch load in a 1-D geometry. This power flow, P^{Load}, produces increases in the energy stored within the z-pinch plasma and radiated from it:

$$P^{Load} = \frac{d}{dt}\left(U_{Fluid} + \frac{1}{8\pi} \int_{Plasma} dV\, B_\theta^2 \right) + P^{Rad} ,$$

where $U_{Fluid} \equiv \int_{Plasma} dV\left(u_{KE} + u_{Thermal} + u_{Ioniz}\right)$, the total plasma energy, is the sum of kinetic, thermal, and ionization energy parts and P^{Rad} is the total x-ray power emitted from the plasma. From the total energy equation of the fluid equations in a 1-D geometry, one also finds that

P^{Load} can be expressed in terms of the Poynting flux of the transmission line electromagnetic energy through the moving surface, $b(t)$, of the pinch:

$$P^{Load} = Lim_{\varepsilon \to 0} 2\pi\ell r \left\{ \frac{dr}{dt} \frac{B_\theta^2}{8\pi} + \frac{c}{4\pi} E_z B_\theta \right\} \Big|_{r=b-\varepsilon} ,$$

Finally, to be consistent with the circuit equation, one must also have that $P^{Load} = \left(\frac{1}{2} \frac{dL_{load}}{dt} + R_{load} \right) I^2$. On inserting the surface values for B_θ and E_z, which are obtained from Ampere's law: $B_\theta = 2I(t)/cb$ and from Ohm's law:

$$E_z = -\frac{1}{c}\frac{db}{dt}B_\theta + \frac{1}{n_e e}\left(\alpha_\perp \frac{j_z}{n_e e} + \beta_\Lambda \partial_r (k_B T_e) \right),$$

into the Poynting vector expression for P^{Load} and by comparing the resulting expression for P^{Load} with the circuit equation expression, one finds that $L_{load}(t) = (2\ell/c^2)\ln(r_{rc}/b(t))$ in agreement with 0-D modeling, and one obtains the following expression for R_{load} :

$$R_{load} = \frac{\ell\eta_0}{A_{th}}\left(\frac{A_{th}}{A_j}\hat{\alpha}_\perp + \frac{1}{2}x_{tr}\hat{\beta}_\Lambda \right).$$

The areas, A_{th} and A_j, appearing in this equation are defined by $A_{th} \equiv I/n_e e v_{th}$ and $A_j \equiv I/j_z(r=b)$, where the thermal velocity, v_{th}, is defined by $v_{th} \equiv \sqrt{2k_B T_e/m_e}$. The dimensionless transport quantities, $\hat{\alpha}_\perp$, $\hat{\beta}_\Lambda$, and x_{tr}, are defined by $\hat{\alpha}_\perp \equiv 1 - (\alpha_1' x_b^2 + \alpha_0')/\Delta$, $\hat{\beta}_\Lambda \equiv x_b(\beta_1'' x_b^2 + \beta_0'')/\Delta$, and $x_{tr} \equiv v_{th}\tau_e \partial_r \ln(T_e)$. The coefficients in these definitions are given in Ref. [4] and $x_b \equiv eB_\theta \tau_e/(m_e c)$. The resistivity, η_0, is defined by $\eta_0 \equiv m_e/(n_e e^2 \tau_e)$.

All of the quantities appearing in the expression for R_{load} are evaluated at the surface of the pinch. At this surface, micro-instabilities can be generated because Ohmic heating drives up the plasma temperature and drives down the plasma density. As the density decreases, the current drift velocity increases and a point is reached at which micro-instabilities can onset. To account for this process, one needs to replace the classical resistivity, $\hat{\alpha}_\perp \eta_0$, by one with an additional micro-instability contribution: $\hat{\alpha}_\perp \eta_0 \to \hat{\alpha}_\perp \eta_0 + \eta_{Micro}$. In Ref. [5], it was postulated that lower hybrid drift waves, which have been detected in a theta pinch sheath, could also be important in adding anomalous resistance to z-pinches. In this case, a formula for η_{Micro} was offered that, unlike η_0, which is essentially density independent, has an inverse dependence on the surface density.

SUMMARY

In the absence of well-developed theories, one must rely on phenomenological models to compute the enhanced energy inputs to a z-pinch that are needed to account for the large x-ray

outputs that are observed from pinches in multi-mega-ampere and/or long current-risetime generators. Moreover, the parameters in such models must be set with guidance from experimental data when theoretical guidance is missing. Since more than one explanation is often possible of observed z-pinch behavior, experimental data must also be used to determine the presence or absence of the underlying phenomena that each explanation assumes in accounting for the observed behavior. The data most relevant to this task to date has been the early-time rate of increase of the diode current, the onset times of the x-ray emissions, the times to peak emission, the pulseshapes of the total x-ray emission and the K-shell emissions, and the total and K-shell x-ray yields.

The problem of incorporating a phenomenological flux-tube model of enhanced energy coupling into a 1-D MHD z-pinch calculation provides an example of the kind of guidance that is needed to implement the model. Neither the dynamics by which a Rayleigh-Taylor instability at the surface of a pinch generates magnetic flux-tube energy nor the fluid dynamics by which this energy is subsequently thermalized has been demonstrated. Nevertheless, experimental data from the shots in Table 1 suggest two important features of this proposed enhanced coupling mechanism. One, a significant amount of flux-tube energy generation appeared to be needed during the run-in in order to account for the observed implosions times of the shots. However, the thermalization of this energy had to be delayed until just prior to pinch assembly in order to get agreement with the observed x-ray emission onset times.

Calculations carried out using a 0-D model of the Saturn generator support the need for a load resistance that grows rapidly to a maximum value prior to load assembly on axis. Maximum load resistances in excess of 0.4 Ω are needed for energy inputs to exceed 500 kJ for a 616 µg/cm load, in accord with the x-ray outputs in the main pulse that were observed in shots 2636 and 2693 on Saturn. However, the coupling of a z-pinch plasma to a transmission line occurs by virtue of a flow of electromagnetic energy from the vacuum diode through the plasma surface, where it is subsequently transported into the plasma by magnetic field diffusion, heat conduction, radiation transport, and compressive heating or shock wave propagation. How an enhanced amount of Ohmic heating is generated by these processes in a 1-D fluid calculation by micro-instabilities at the surface of a pinch has yet to be determined.

ACKNOWLEDGMENTS

REFERENCES

1. Rudakov, L. I., et. al., Phys. Rev. Lett., **84**, 3326 (2000).
2. Velikovich, A. L., et. al., Phys. of Plasmas, **7**, 3265 (2000).
3. Labetsky, A. Yu., et. al., IEEE Transact. on Plasma Sci., to be published.
4. Braginskii, S. I., in *Reviews of Plasma Physics*, edited by M. A. Leontovich (Consultants Bureau, New York, 1965), Vol. 1, pp. 205-311.
5. Robson, A. E., Phys. of Fluids B, **3**, 1461 (1991).

II. RADIATION TRANSPORT IN Z PINCHES AND OTHER DENSE PLASMAS

I.   INTRODUCTION

Radiation transport is the redistribution of energy within a medium through the emission and absorption of photons. It is of great importance in influencing the yield and diagnostics of Z pinches. Its importance in the laboratory plasma context depends to a large extent on the optical depth of the plasma under consideration, which increases with its size and density. The potential size and/or density of a plasma is limited by the energy available to create it, and both size and density can increase as that energy is enhanced. Over the past few decades, the deliverable energies of state-of-the-art pulsed-power generators and high power lasers have steadily increased. At Sandia National Laboratories, the Z generator[1] is capable of delivering over 2 MJ to a Z-pinch load at currents approaching 20 MA, an increase of a factor of ~ 4 in energy compared to the previous generation Saturn machine. At Lawrence Livermore National Laboratory, the National Ignition Facility[2] envisions laser energies on target in excess of 1 MJ, as compared to tens of kilojoules for the previous generation Nova laser. At the University of Rochester, the upgraded Omega laser[3] delivers more than an order of magnitude more energy to its targets than did the original Omega system. Thus, the importance of radiation transport to the dynamics and diagnostics of both laser- and pulsed-power-produced plasmas is increasing.

In this chapter, we review the theory of radiation transport, its physical effects, experimental signatures, and current issues and challenges in the field relating to dense laboratory plasmas. Sec. II presents the basic theory and equations describing radiation transport, and describes conditions under which the theory can be simplified by approximations. Sec. III describes the physical effects of radiation transport, and presents calculations and experimental examples of some of these effects as they are manifested in dense laboratory plasmas. Current challenges and issues in the field are summarized in the concluding Sec. IV. The emphasis is primarily on the physics of radiation transport, rather than numerical methods. Our overall aim is to describe the rich physics and diversity of phenomena brought about by the interaction of a plasma with the photons it emits.

II. BASIC THEORY AND EQUATIONS

A. The equation of transport

The initial developments in the theory of radiation transport occurred early in the 20th century and are mostly due to Planck, Schuster, Schwarzschild, Milne, Eddington, and Rosseland. Chandrasekhar's elegant treatise[4] summarizes the state of the field prior to the advent of high-speed computers. Despite the intervening discoveries in quantum physics, the theory retains its validity over a wide range of physical conditions. A derivation of radiation transport theory from quantum electrodynamics, and a discussion of the limits of its validity, has been given by Sudarshan[5].

39

The equation of radiation transport and its moments can be written in full three-dimensional generality using vector differential operators[6]. Here we follow a perhaps more physically intuitive approach and initially consider photons traveling in the positive direction along a single ray s. The ray begins at $s = 0$, and the intensity of the photon field is to be calculated at $s = s_0$, with a known photon intensity incident upon the ray at $s = 0$. In CGS units, the fundamental radiation quantities of the equation of transport are: the *specific intensity I_v*, at frequency v, in erg/(cm^2-sec-sr-Hz), the *emission coefficient j_v*, in erg/(cm^3-sec-sr-Hz), and the *absorption coefficient k_v*, in cm^{-1}. A derived quantity, the *source function S_v*, is defined as j_v / k_v. The equation of transport is

$$\frac{\partial I_v}{\partial s} = j_v - k_v I_v - \frac{1}{c}\frac{\partial I_v}{\partial t} \tag{1}$$

The third term on the right hand side is negligible unless the plasma changes significantly during a photon transit time; it is usually necessary to carry this term only in cases where the plasma is driven by a sub-ps laser[7], and it is not considered further here. The physical content of Eq. (1) is that, along a ray, the specific intensity increases in proportion to the local emission coefficient, but is attenuated at a rate equal to its product with the local absorption coefficient. If j_v and k_v are known along the ray s, the formal solution to Eq. (1) may be straightforwardly obtained, as detailed elsewhere[8]

$$I_v(s_0) = I_v(0)\, e^{-\tau_v(0)} + \int_0^{s_0} j_v(s)\, e^{-\tau_v(s)}\, ds \tag{2}$$

where the optical depth $\tau_v(s)$ between point s along the ray and the viewpoint s_0 is given by

$$\tau_v(s) = \int\limits_{S}^{S_o} k_v(x)\,dx \ . \tag{3}$$

The first term on the right hand side of Eq. (2) represents exponential attenuation of radiation incident on $s = 0$, and the integral in Eq. (2) describes the cumulative effect of emission and absorption along the ray. Equation (2) also implies that the specific intensity I_v along an optically thick ray is approximately equal to the value of the source function S_v at one optical depth inward from the observation point. Even though it is usually not the most efficient numerical method, the radiation field of a medium of any shape or dimensionality can be represented with an appropriate set of rays. It can be calculated as a function of space, time, and frequency given the emission and absorption coefficients.

The physical complexity of radiation transport within a plasma, and the numerical difficulties in solving the transport equation, both stem from the fact that the absorption and emission coefficients not only determine the radiation field, but are (usually) to a significant extent determined by it. For instance, the absorption coefficient at a given frequency is equal to the population density of atomic states which absorb photons of that frequency multiplied by the absorption cross section. However, the population density can be influenced by radiative processes such as photoexcitation and photoionization. In general, therefore, iteration is required between the formal solution of the transport equation and a set of atomic rate equations (which must include the radiation field and all significant radiative processes).

B. Radiation diffusion

In some instances, prevailing plasma conditions may result in a much simpler physical picture as well as a much less daunting numerical challenge. If the plasma is optically thick at all photon frequencies, its radiation is transported diffusively in many small steps of absorption and re-emission. In such a case, spatial randomization produces a nearly isotropic radiation field that is well described by a diffusion theory. The elements of this theory are obtained by taking moments of Eq. (1). The nth moment of Eq. (1) results from multiplying both sides by the nth power of the cosine of the angle subtended by the ray and the outward normal direction, and then integrating over 4π sr. When the radiation field is isotropic, the ratio of the second to the zeroth moment of the specific intensity (the so-called "Eddington factor") is 1/3. This approximation provides closure of the sequence of moment equations, leading to a diffusion equation for the net flux F_ν

$$F_\nu = -\frac{4\pi}{3k_\nu}\frac{dS_\nu}{dz}.$$ (4)

Equation (4) applies to planar geometry, z being the coordinate normal to the plane. It is of the form given in Ref. 8, i.e., the flux is given by the gradient of the source function multiplied by an effective diffusion coefficient (the reciprocal of the absorption coefficient, which is the mean free path). Other forms of a diffusion equation can be derived, depending on whether local thermodynamic equilibrium (LTE) applies (see below), on the specific sequence of algebraic substitutions used when simplifying the moment equations, and on the assumed geometry of the medium. For plasma in LTE, the following diffusion equation can be employed to solve for the radiation energy density u_ν

42

$$\frac{d}{dz}\left(\frac{1}{3k_v}\frac{du_v}{dz}\right) = k_v\left(u_v - u_{BBv}\right) \qquad (5)$$

where k_v is the absorption coefficient and u_{BBv} is the energy density of blackbody radiation at the local electron temperature. Note that diffusion theory can eliminate the need for a calculation of the spatial dependence of the radiation field. Through the use of average opacities such as the Rosseland and Planck means (see Chap. 2 of Ref. 8) the need for a detailed multifrequency treatment can also be reduced or eliminated. This description of the attractive features of the use of a diffusion equation to describe plasma radiation needs to be accompanied by a cautionary note. The radiation of plasmas primarily composed of low and medium atomic number elements is often dominated by emission from well-separated spectral lines. This is especially true if most of the ions are in the H- or He-like K shell or certain L-shell stages with relatively simple spectra. Many of these lines are optically thick, and the radiation within the cores of their profiles is well described by diffusion. However, most of the radiation that is transported within such lines as well as that which ultimately escapes the plasma is often located in the wings of the line profiles, where the optical depth is lower and the consequent mean free photon path greater. This (sometimes dominant) part of the overall radiation field is not well described by a diffusion theory, and the use of diffusion is ill advised in modeling such a plasma. However, if the continuum is also optically thick, or if the lines overlap, free-streaming photon escape and transport on the line wings is greatly reduced, and diffusion may then become a reasonable approximation.

C. The state of local thermodynamic equilibrium (LTE)

The axioms of entropy maximization and microscopic reversibility jointly assert that a state of thermodynamic equilibrium (TE) exists in any plasma in which the number of transitions in each atomic process is equal to those of its inverse (detailed balancing). The ionization stage distributions and bound state population fractions are then given by the Saha and Boltzmann equations. Since virtually no plasmas are uniform in temperature, the radiation passing through a given parcel of plasma cannot in general represent a single temperature. However, collisional processes are local. If they are dominant in determining the populations of the various ionic stages and bound levels, and if the colliding electrons are in the state of maximum entropy, i.e., a Maxwellian distribution, the local populations will still be given, to a good approximation, by the Saha and Boltzmann equations. This condition is referred to as local thermodynamic equilibrium (LTE). In LTE, the source function is given by the Planck function $B_\nu(T_e)=(2h\nu^3/c^2)/[exp(h\nu/kT_e)-1]$ evaluated at the local electron temperature. The requirement that collisional transition rates exceed those of radiative processes implies that a minimum density is required for a plasma to be in LTE. The next section presents calculations of such minimum densities for two elements. If the collision rates do not well exceed the radiative rates, a state of LTE may still result if the plasma is optically thick at all frequencies, so that each radiative emission process is detail balanced by self-absorption.

III. BASIC EFFECTS: CALCULATIONS AND EXPERIMENTS

A. Densities needed for LTE

As explained above, for an optically thin plasma a minimum density is required, such that collisional transition rates well exceed the radiative rates, to bring the plasma into a reasonable approximation of LTE. For specificity, we adopt the criterion given by Griem[9] that for LTE to prevail for all levels the collisional rates must be at least an order of magnitude greater than the corresponding radiative rates. The electron density needed to fulfill this criterion varies according to element and ionization stage. As the charge state of a given element increases, the collisional rate coefficients tend to decrease while the radiative transition probabilities increase. This results in a sharp general upward trend in the electron density needed for LTE as ionic charge increases. This trend is not always rigorously followed from stage to stage because of the discrete and individualized nature of atomic electron configurations. Figs. 1 and 2 show calculations of the electron density needed for LTE for various ionic stages of Al and Au, respectively. They demonstrate that both Al and Au obey the expected overall trend requiring higher electron densities for higher charge states. These calculations are based on an atomic database calculated and compiled as described in Ref. 10. For each ionization stage, the electron temperature has been assumed to equal one-third of the ground state ionization potential. Note from Fig. 1 that the trend toward higher required electron densities for higher charge states is conspicuously violated for the K-shell stages of Al. The He-like Al stage needs higher electron density than does the H-like to reach full LTE primarily because of the strong $1s^2$

$^1S_0 - 1s2p\ ^1P_1$ radiative transition whose spontaneous decay rate exceeds that of the corresponding H-like 1s-2p line by nearly a factor of 2.

As the plasma density approaches that required for LTE, its radiative source function approaches the Planck function. As its opacity increases along with the density, the emitted intensity must approach the source function, i.e., a blackbody spectrum. This phenomenon is demonstrated in Fig. 3, which presents calculated spectra emitted by a 3 mm diameter Al cylinder as its ion density increases from 10^{19} to 10^{23} cm^{-3}. The spectrum was divided into more than 2000 photon energy groups to carry out this calculation; further details are given elsewhere[11]. The electron temperature is assumed to be 398 eV; a blackbody spectrum of that temperature is also shown in Fig. 3. Figure 1 explains the major features of the evolution of these calculated spectra toward the Planck limit. Note that the lower energy L-shell lines approach the blackbody limit at a lower density; this is just what is expected from Fig. 1 for the lower ionization stages. Note also that at 10^{23} cm^{-3}, the He-like K-shell transitions above 1.5 keV appear as absorption lines, but the H-like lines are in emission. This is a manifestation of the higher densities needed for the He-like stage to reach full LTE as discussed above and shown in Fig. 1.

B. Experimental measurements of a diffusion wave

According to the discussion of Sec. II B, diffusive radiation transport is a poor description for a plasma whose continuum is thin and whose opacity is mostly due to non-overlapping lines. It is more appropriate for a plasma whose elements contain many

opaque overlapping lines or continuum features that inhibit free streaming of photons. Plasma composed of a high atomic number element such as gold or tungsten, with a complex many-electron atomic structure (even when highly ionized) would likely be the strongest candidate for a diffusive medium. However, lower atomic number element plasmas may also exhibit diffusive behavior as long as they are not stripped to the simple K-shell, H- and He-like ionic stages. Recently, Back et al.[12] observed a supersonic radiative diffusion wave in a SiO_2 foam plasma which was driven by x-rays from a laser-heated hohlraum. The peak temperature of the x-ray drive was approximately 85 eV, the foam plasma temperature, 40-60 eV. The velocity and spatial distribution of the diffusion wave was measured by repeating the experiment with several different lengths of foam in conjunction with an x-ray streak camera and time-gated x-ray imaging which recorded the breakout times at a photon energy of approximately 250 eV, see Fig. 4. Marshak first analyzed radiative diffusion waves[13] in a classic paper. Their properties, including spatial profiles and velocities, are sensitive probes of the conditions of the medium through which they propagate. The Mach 2.5 diffusion waves measured in the work described in Ref. 12 were well reproduced by radiation hydrodynamics simulations based on the OPAL opacity data[14]. The radial intensity profile measurements are fitted much better by the OPAL data than by average atom opacities.

C. Sources of opacity and absorption lines

To calculate radiation transport, or to assess its effects when designing or analyzing an experiment, the absorption coefficient as a function of photon energy must be known.

The principal sources of opacity in dense plasma are: bound-bound transitions (spectral lines), bound-free transitions (photoionization of a bound electron), and free-free transitions (bremsstrahlung radiation). Unless the plasma is fully stripped to bare nuclei, the maximum (monochromatic) absorption usually occurs in the cores of strong lines. The bound-free continuum is normally the second strongest opacity source, followed by free-free radiation. For order-of-magnitude estimates of the absorption cross-sections for these processes, consider plasma with an electron and ion temperature of 1 keV. At a photon energy of 1 keV, a typical absorption cross section at the center of a strong Doppler-broadened line is $\sim 10^{-16}$ cm^2. For a given oscillator strength, line cross-sections scale approximately as the inverse of the transition energy. A typical photoionization cross-section at threshold is $\sim 10^{-19}$ cm^2. The free-free cross-section per ion is proportional to the electron density N_e and the square of the ionic charge Z: it is about $10^{-47} N_e Z^2$ cm^2 at 1 keV. Both the bound-free and free-free cross-sections scale approximately as the inverse cube of the photon energy. For plasma of a given size, strong lines become optically thick at densities about three orders of magnitude lower than are required to produce an optically thick x-ray continuum. Detailed atomic physics calculations are required to obtain accurate cross-sections; to convert cross-sections to absorption coefficients as a function of energy (i.e., opacity data) the ionic stage and bound level populations must be known. In general, as pointed out above, the populations are influenced by the radiation field, which in turn depends on the global properties of the plasma. Since plasmas can vary so widely, this would seem to preclude general tabulation of opacities. However, for plasmas in LTE, detailed opacity databases such as OPAL[14] or TOPS[15] have been developed. They may be employed for approximate calculations for

non-LTE plasmas, but the developers of OPAL, for example, have cautioned in Ref. 14 against expecting detailed agreement with experiment in such instances.

A key factor affecting the appearance of lines in a spectrum is the fact that their absorption cross-sections generally exceed those of continuum processes by two orders of magnitude or more. As a consequence, there is a wide regime of plasma conditions in which lines are optically thick, but continua are thin. The intensity of a thin continuum is approximately equal to its source function multiplied by its (small) optical depth. In contrast, the intensity of an optically thick line is nearly equal to its source function. In this regime, therefore, lines are more intense than the continuum and are thus seen as emission lines. As the density increases, the gap between the line and continuum intensities gradually narrows; but the lines remain much more opaque and radiation that escapes from their very thick cores generally originates near the outer boundary of the plasma. If the outer boundary plasma is cooler than the interior, which it often is, the intensity of the less opaque continuum that originates deeper in the plasma can exceed that of the line cores. This set of circumstances produces absorption lines. Figure 5 illustrates these features of line formation. A 3 mm diameter Al plasma is assumed to have a core electron temperature of 600 eV and outer surface temperature of 200 eV. Its calculated K-shell spectrum is plotted for assumed (uniform) ion densities of 3×10^{19} and 10^{22} cm^{-3}. At the lower of these densities, the lines are strongly in emission, but at the higher density, in absorption. Note that the intensities of the cores of the He-like lines closely approximate a 200 eV blackbody for the higher density case. This is due to the

49

fact that they are formed at the surface of the plasma where the electron temperature is

200 eV.

D. Diagnostics based on radiation transport

A striking example of formation of absorption lines as well as their use in plasma

diagnosis is provided by some experiments of Hauer et al.[16]. A gas-filled microballoon

target of diameter 0.43 mm was imploded with 4.5 kJ of energy from the Helios CO_2

laser system at Los Alamos National Laboratory. The Ar-DT fill gas was enclosed in a

glass shell. Between that shell and an outer plastic tamper, a layer of KCl was embedded

to provide a source of absorption lines during the implosion. Most of the absorption lines

that were observed (Fig. 6) arise from transitions between the n=1 K shell to vacancies in

the n=2 L shell of Cl ions already containing 1-6 electrons in that shell. The He-like n=1

to n=2 absorption line was also detected. The broad absorption features seen in Fig. 6

arising from the Li-like and lower ionization stages are complexes containing 1-35

individual transitions, the exact number depending on the ionization stage. The

absorption lines arise from the sharp difference between the 700 eV core electron

temperature and the pusher temperature of 200-230 eV. The distribution of ionization

stages in Cl is strongly temperature-dependent; fitting of the distribution of strengths of

the various absorption complexes to the predictions of a non-LTE model gives the pusher

temperature. The optical depths of the absorption features are proportional to the $\rho\Delta R$

product of the Cl-bearing layer. Given the known intrinsic strengths of the absorption

lines, the measured absorption in each complex, and the distribution of ionization stages,

a partial $\rho\Delta R$ can be obtained for each ion; summing over the observed ionic species gives the total $\rho\Delta R$ for the layer. Further details are given in Ref. 16. This initial work has been further developed and refined, especially at the University of Rochester. One signature of core-shell mixing is emission lines that result when shell material migrates to the hotter core of an imploding spherical laser target, as described by Yaakobi et al.[17].

Despite the recent blossoming of Z-pinch research, absorption lines have yet to be used to diagnose their conditions. Indeed, they have rarely been detected in x-ray spectra of Z pinches. An exception to this pattern, which may lead to future quantitative diagnosis, is shown in Fig. 7. This figure displays a time-integrated x-ray spectrum, taken in the axial direction, of a wire array pinch from shot 427 on the Z generator of Sandia National Laboratories. The wires were composed of the alloy known as Al 5056, which contains 95% Al and 5% Mg. The total array mass employed, 6 mg cm^{-1}, is several times that which produces optimum yields of K-shell, keV photons[18]. Note from Fig.7 that inner shell absorption complexes from the Li-like and Be-like stages of Mg were observed, analogous to those reported by Hauer and co-workers in Ref. 16. Although no quantitative interpretation can be given at this time, the general picture is likely to be similar to that deduced for laser-imploded capsules: cooler outer material present in sufficient abundance to be opaque forms absorption lines.

The opacity of plasma can also be measured using emission lines. Consider a plasma of fixed electron density, but composed of ions of two elements, say Al and Mg, as is the case when Al 5056 wire loads are used to create a Z pinch. Assume initially that the Mg

51

fraction is so small that the optical depths at the cores of even the strongest Mg lines are much less than unity. Under such conditions, the emission in the Mg lines is linearly proportional to the Mg density, thus doubling the fractional composition of Mg would double the emission from the Mg lines. The emission of the dominant, optically thick Al lines behaves quite differently. Since the Doppler cores and much of the wing structures of the Al lines are optically thick, very little extra emission is obtained by increasing the already dominant proportion of Al ions. Therefore, if one objective of an experiment is to increase the overall x-ray emission, summed over both the Al and Mg lines, one should remove ions of the dominant Al component and replace them with those of the trace Mg component, as has been demonstrated with detailed calculations[19] and verified experimentally[20]. Furthermore, since the ratio of the density of the trace to the dominant element is known, the measured intensity ratio of a line or lines from the trace component to the same line or lines emitted by the dominant component is a measure of the attenuation of the lines of the dominant optically thick component. Figure 8 provides a particularly clear demonstration of this manifestation of radiation transport. This figure shows the He- and H-like α lines emitted during shot 70 of the Z generator at Sandia National Laboratories. Despite Mg constituting just 5% of the plasma ions, its lines in this spectrum sum to 31% of the intensity of their counterpart Al lines. This is a clear indication that opacity has restrained the Al emission by a substantial factor. Diagnosis of the pinch conditions, including its energy-dependent opacity, must be consistent with this Mg/Al line ratio of 0.31. The modeling described in Ref. 18 predicts this ratio to better than 10%, therefore the pinch diagnosis reported in that article provides a reasonable representation of at least the K-shell opacity of the pinch.

IV. CURRENT ISSUES AND CHALLENGES

The preceding sections have presented the fundamental physics of radiation transport in dense plasmas. To illustrate basic principles and physical processes, some present and past research in the field has been discussed. However, there are many other areas of current research in dense plasmas in which radiation transport is of significant, or even dominant importance. This concluding section describes some of these endeavors. In the four sub-sections that follow, we briefly describe and motivate the ongoing efforts in each frontier area; the interested reader may consult the references to the original work for further details. The categories are organized according to the nature of the research rather than by specific device or laboratory.

A. Numerical modeling

Even though we have emphasized physical principles rather than computational issues, numerical modeling has played a vital role in elucidating the physics of radiation transport and in analyzing experiments, and will continue to do so. Using state-of-the-art algorithms, it is currently possible to perform a non-LTE one-dimensional (1D) radiation-magnetohydrodynamics (RMHD) calculation (tracking a laser- or pulsed-power-driven plasma for nanoseconds) on a GHz-class personal computer in a few hours. Such a simulation uses a detailed atomic database for a low or medium atomic number element to calculate the radiation field, opacities, and populations self-consistently. The complex

atomic structure of high atomic number elements gives rise to a large number of levels and unresolved transition arrays. A number of strategies have been proposed and developed to enhance the feasibility of non-LTE RMHD simulations for high atomic number elements; Klapisch et al[21] discuss these.

It is obviously desirable to extend the domain of realistic RMHD simulations to two- and three-dimensional geometries. At present, multidimensional RMHD calculations use simplifying approximations to avoid otherwise prohibitive computational requirements. These approximations include: assuming that the plasma is optically thin or use of a local probability-of-escape treatment (e.g., the PRISM code[22]), or assuming LTE with diffusion and a Rosseland mean opacity (e.g., the MACH2 code[23]). Recently, Thornhill et al.[24] have demonstrated a promising technique in which the local probability-of-escape approximation is accelerated by using tabulated source functions that have been pre-calculated, albeit for uniform plasmas. The overall increase in computer time required for 2-D vs. 1-D RMHD calculations is usually at least two orders of magnitude. However, it varies according to the numerical algorithm used; for a simple ray trace the CPU time scales approximately as the square of the number of zones, but the time required when using the variable-Eddington-tensor method[6] scales linearly with the number of zones.

B. Radiation efficiency and uniformity

One of the prime applications of dense plasmas is their use as x-ray sources. X rays produced by laser irradiation, or by Z pinches, can be confined in a hohlraum (radiation cavity) with the ultimate goal of driving a fusion capsule to ignition. Another application of high power plasma x-ray sources is the study of radiation-material interactions, including the launching of shock waves as a means of diagnosing the material's equation of state. Recently, plasma formed from the laser irradiation of a xenon gas jet has emerged as a principal candidate for the radiation source for extreme ultraviolet lithography[25]. For all of the above plasma radiation sources, it is desirable to maximize both the efficiency of x-ray production and the spatial uniformity of the emitted radiation. By no means is radiation transport the only physics issue that arises when confronting these goals; however, it is certainly a major one.

In a laser-driven hohlraum, laser beams injected through entrance holes energize a cavity whose radiating walls are composed of high atomic number elements[26]. Transport and escape of x-rays within and from the wall plasma are a major factor in determining the overall performance of the hohlraum with regard to symmetry of capsule irradiation and achievable radiation temperature[27]. It has recently been demonstrated that fabricating the hohlraum walls from mixtures of elements rather than from a single element reduces wall losses by plugging opacity "holes" in various regions of the x-ray spectrum[2,28,29].

Z pinch plasma radiation sources have been reviewed by Pereira and Davis[30] and by Ryutov, Derzon, and Matzen[31]. Radiation transport is a key physics issue affecting the emitted x-ray power and yield of a Z pinch. Ref. 20 reported an increase in keV x-ray yield of 50% when mixing Al and Mg instead of using a pure Al wire load. Similar in concept to filling in hohlraum opacity "holes" in the spectrum, this successful approach to enhancing x rays fills in spectral emissivity "holes". There are various types of Z-pinch-driven hohlraum; radiation transport needs to be taken into account in their design, and is vital to their successful performance. The "static-wall" hohlraum[32] transports radiation from one or two coaxially located Z pinches into a radiation cavity. A "dynamic" hohlraum[33] traps radiation inside an optically thick Z pinch that is formed from an outer liner, which collides with an inner target that can be foam or a plastic liner. Another interesting design[34] energizes a coaxial, centrally located secondary hohlraum with two primary Z-pinch driven hohlraums located at its ends. Stygar et al.[35] have recently developed a unified analytic model of hohlraum physics.

C. Effects on plasma dynamics

The dynamic behavior of plasma is strongly influenced by its equation of state. An important element of the equation of state is the radiative response of a plasma to compressive forces such as the $J \times B$ "magnetic piston" of a Z pinch, shock waves, or the ablation pressure generated by blowoff of the outer layer of a fusion capsule.

The issue of radiative collapse in a Z pinch provides an interesting example of both current and historical importance. Suppose initially that the pinch is optically thin. Then its emission is proportional to the square of the density, and upon $J \times B$ compression, the plasma radiates at a greater rate, resulting in cooling, greater compressibility, and a possible spiral of collapse to very high density. This scenario has been considered and investigated for decades in quasi-static hydrogen pinches for fusion research. When a Z pinch becomes optically thick, its emissivity is no longer proportional to the square of the density, but acquires a much more complicated dependence depending on the intricacies of the radiation transport within the plasma. At very high density, the pinch becomes a surface blackbody emitter, at which point its radiative power output can decrease upon compression, halting any radiative collapse[36]. The phenomenon of radiative collapse is also relevant to the behavior of dynamic, multi-megampere Z pinches that are primarily used as radiation sources. Intensely radiating submillimeter-sized structures have been observed on several generators[37-39]; these may be regions within pinches where partial radiative collapse has occurred.

Transport of radiation can also have significant effects on the dynamics of laser-produced plasmas. Dahlburg et al.[40] noted the development of localized, shock-like density enhancements in simulations of laser-driven, ablating plasmas. These features form in regions where the atomic shell structures of carbon or chlorine maximize line emission. Their formation and evolution is evidently dependent on the detailed temperature dependence of radiative cooling as well as radiation transport between fluid elements[41]. It may be possible to harness the effects of radiation transport to enhance the performance

of laser fusion targets. For instance, the effects of the ablative Rayleigh-Taylor instability may be mitigated[42] by tailoring soft x rays to preheat the ablator, thereby raising its isentrope and reducing the instability growth rate.

D. Diagnostic uniqueness - the inverse source problem

The diagnosis of plasma conditions using spectroscopic measurements is a vast and highly developed field. The book by Griem[9] is perhaps the best general reference and guide to current research in this area. One of the fundamental questions that this field attempts to address is: are the derived plasma conditions unique, or, phrased differently, how much spectroscopic information must be collected to infer a given level of detail regarding the plasma conditions? This question-known as the inverse source problem[43]-has not been fully answered.

For an optically thin plasma, intensity measurements taken along various lines of sight can be used in conjunction with Abel inversion to obtain the emissivity as a function of position (see Sec. 8.5 of Ref. 9), which translates to temperature and density when interpreted with appropriate atomic data. This approach is similar to medical diagnostic tomography. However, multiple chord measurements are not always practical, nor are most dense plasmas optically thin. A problem of great practical interest is inferring plasma conditions from spatially integrated spectroscopy of an optically thick plasma. The opacity of such a medium is to some extent a diagnostic asset, because the differing absorptivities of various spectral regions sample the emission of the plasma at a range of

depths along the line of sight. Due to the complex, nonlinear dependences of spectral features on plasma properties, it is unlikely that analytic methods can be employed to prove or disprove uniqueness, or to obtain a one-to-one correspondence between the level of spectral detail measured and the level of plasma detail inferred[44]. If a uniform plasma is assumed, a solution for its temperature and density may be obtained by plotting the isocontours of an observed temperature-dependent line ratio and of the (mostly density dependent) emitted power in the temperature-density plane. Their single intersection provides unique values of plasma temperature and density. However, a non-uniform case was discovered[44] in which, rather than cleanly intersecting, the contours closely overlap for a range of plasma core temperatures between 400 and 800 eV. In that work, a power law temperature profile was assumed. Another case of non-unique diagnosis is described on p. 243 of Ref. 9. More recently, use of four line ratios as well as the measured K-shell power led to an apparently (but not provably) unique diagnosis of non-uniform conditions in several Z pinches[39]. Given the ever-increasing accessibility and speed of both personal and mainframe computers, this long-standing problem is ripe for rapid progress, and the possibility of more surprises, in the near future

REFERENCES

1. R. B. Spielman, C. Deeney, G. A. Chandler *et al.*, Phys. Plasmas **5**, 2105 (1998).

2. L. Suter, J. Rothenburg, D. Munro, B. VanWonterghem, and S. Haan, Phys. Plasmas **7**, 2092 (2000).

3. T. R. Boehly, D. L. Brown, R. S. Craxton *et al.*, Opt. Commun. **133**, 495 (1997).

4. S. Chandrasekhar, *Radiative Transfer* (Dover, New York, 1960).

5. E. C. G. Sudarshan, Phys. Rev. A **23**, 2802 (1981).

6. R. I. Klein, J. I. Castor, A. Greenbaum, D. Taylor, and P. G. Dykema, J. Quant. Spectrosc. Radiat. Transfer **41**, 199 (1989).

7. J. P. Apruzese, Phys. Rev. E **47**, 2798 (1993).

8. D. Mihalas, *Stellar Atmospheres* (W. H. Freeman, San Francisco, 1970).

9. H. R. Griem, *Principles of Plasma Spectroscopy* (Cambridge University Press, Cambridge, 1997), p. 213.

10. D. Duston and J. Davis, Phys. Rev. A **23**, 2602 (1981).

11. J. P. Apruzese, K. G. Whitney, J. Davis, and P. C. Kepple, J. Quant. Spectrosc. Radiat. Transfer **57**, 41 (1997).

12. C. A. Back, J. D. Bauer, O. L. Landen, R. E. Turner, B. F. Lasinski, J. H. Hammer, M. D. Rosen, L. J. Suter, and W. H. Hsing, Phys. Rev. Lett. **84**, 274 (2000).

13. R. E. Marshak, Phys. Fluids **1**, 24 (1958).

14. F. J. Rogers, C. A. Iglesias, and B. G. Wilson, Astrophys. J. **397**, 717 (1992).

15. N. H. Magee, Jr., J. Abdallah, Jr., R.E.H. Clark *et al.,* Astronomical Society of the Pacific Conference Series **78**, 51 (1995).

16. A. Hauer, R. D. Cowan, B. Yaakobi, O. Barnouin, and R. Epstein, Phys. Rev. A **34**, 411 (1986).

17. B. Yaakobi, F. J. Marshall, D. K. Bradley, J. A. Delettrez, R. S. Craxton, and R. Epstein, Phys. Plasmas **4**, 3021 (1997).

18. J. P. Apruzese, P. E. Pulsifer, J. Davis *et al.,* Phys. Plasmas **5**, 4476 (1998).

19. J. P. Apruzese and J. Davis, J. Appl. Phys. **57**, 4349 (1985).

20. C. Deeney, P. D. LePell, B. H. Failor *et. al,* Phys. Rev. E **51**, 4823 (1995).

21. M. Klapisch, A. Bar-Shalom, J. Oreg, and D Colombant, Phys. Plasmas **8**, 1817 (2001).

22. F. L. Cochran, J. Davis, and A. L. Velikovich, Phys. Plasmas **2**, 2765 (1995).

23. R. E. Peterkin, Jr., M. H. Frese, and C. R. Sovinec, J. Comput. Phys. **140**, 148 (1998).

24. J. W. Thornhill, J. P. Apruzese, J. Davis et al., Phys. Plasmas **8**, 3480 (2001).

25. G. Stix, Sci. Am. **284**, 32 (April 2001).

26. J. Lindl, Phys. Plasmas **2**, 3933 (1995).

27. L. J. Suter, R. L. Kauffman, C. B. Darrow *et al.,* Phys. Plasmas **3**, 2057 (1996).

28. T. J. Orzechowski, M. D. Rosen, H. N. Kornblum, J. L. Porter, L. J. Suter, A. R. Thiessen, and R. J. Wallace, Phys. Rev. Lett. **77**, 3545 (1996).

29. D. Colombant, M. Klapisch, and A. Bar-Shalom, Phys. Rev. E **57**, 3411 (1998).

30. N. R. Pereira and J. Davis, J. Appl. Phys. **64**, R1 (1988).

31. D. D. Ryutov, M. S. Derzon, and M. K. Matzen, Rev. Mod. Phys. **72**, 167 (2000).

32. T. W. L. Sanford, R. E. Olson, R. L. Bowers *et al.,* Phys. Rev. Lett. **83**, 5511 (1999).

33. T. J. Nash, M. S. Derzon, G. A. Chandler *et al.,* Phys. Plasmas **6**, 2023 (1999).

34. M. E. Cuneo, R. A. Vessey, J. L. Porter *et al.,* Phys. Plasmas **8**, 2257 (2001).

35. W. A. Stygar, R. E. Olson, R. B. Spielman, and R. J. Leeper, Phys. Rev. E **64**, 026410 (2001).

36. A. E. Robson, Phys. Fluids B **1**, 1834 (1989).

37. P. Burkhalter, J. Davis, J. Rauch, W. Clark, G. Dahlbacka, and R. Schneider, J. Appl. Phys. **50**, 705 (1979).

38. K. N. Koshelev, Yu. A. Sidel'nikov, G. Decker *et. al,* Opt. Spectrosc. **76,** 202 (1994).

39. J. P. Apruzese, J. W. Thornhill, K. G. Whitney, J. Davis, C. Deeney, and C. A. Coverdale, Phys. Plasmas **8,** 3799 (2001).

40. J. P. Dahlburg, M. Klapisch, J. H. Gardner, C. R. DeVore, A. J. Schmitt, and A. Bar-Shalom, J. Quant. Spectrosc. Radiat. Transfer **54,** 113 (1995).

41. G. Hazak, A. L. Velikovich, M. Klapisch *et al.,* Phys. Plasmas **6,** 4015 (1999).

42. D. G. Colombant, S. E. Bodner, A. J. Schmitt *et al.,* Phys. Plasmas **7,** 2046 (2000).

43. H.- Y. Li, J. Quant. Spectrosc. Radiat. Transfer **69,** 403 (2001).

44. J. P. Apruzese, J. W. Thornhill, K. G. Whitney *et al.,* IEEE Trans. Plasma Sci. **26,** 1185 (1998).

FIGURE CAPTIONS

FIG. 1. Electron densities needed for full local thermodynamic equilibrium (LTE) for the various ions of Al are plotted vs. ionic charge. The solid line is a least-squares fit to the points. The method of calculation is described in Sec. III A.

FIG. 2. As in Fig. 1, except that the element is Au and only the even-numbered charge states are shown.

FIG. 3. Calculated spectra emitted from a 2 cm long, 3 mm diameter Al cylinder of uniform density and temperature for 3 different ion densities. The electron temperature is 398 eV. Also shown is the spectrum of a blackbody of that size and temperature (dotted line).

FIG. 4. From Ref. 12, shows intensity vs. time for various lengths of a SiO_2 foam plasma heated by x-rays from a laser-driven hohlraum. The dashed lines are data; the solid lines are calculations. The radiation temperature of the x-ray drive is plotted on the right-hand axis.

FIG. 5. Calculated spectra from a 2 cm long, 3 mm diameter cylindrical Al plasma, for the two indicated ion densities. The core electron temperature is 600 eV, the surface, 200 eV. The intensity of a 200 eV blackbody of the same size is shown for comparison (dotted line).

FIG. 6. From Ref. 16, shows absorption line complexes from the indicated ionic stages of Cl formed by a layer of KCl embedded between the glass shell and plastic tamper of a gas-filled spherical microballoon. The target was imploded with 4.5 kJ of energy from the 8-beam Helios laser system at Los Alamos National Laboratory.

FIG. 7. Time-integrated x-ray spectrum of Z shot 427 viewed along the axis of the pinch. The composition of the alloy used for the wire load is 95% Al, 5% Mg. Inner shell absorption features of Li-like and Be-like Mg are indicated.

FIG. 8. From Ref. 18, shows the Al and Mg K-shell α lines from the x-ray spectrum of shot 70 from the Z generator at Sandia National Laboratories. Mg constitutes 5% of the ions in the pinch, but the sum of the intensities of the two Mg lines is 31% of that of the Al lines.
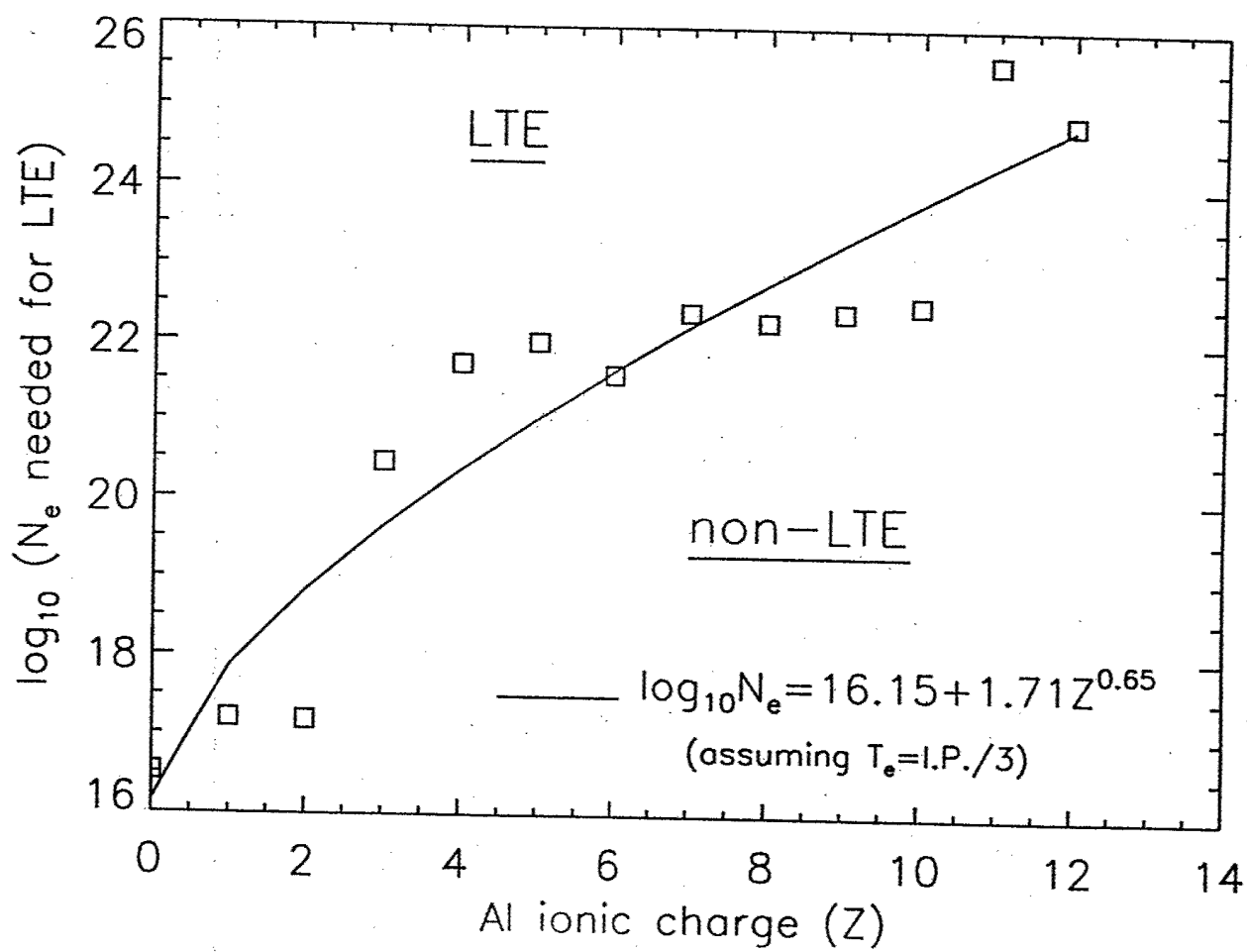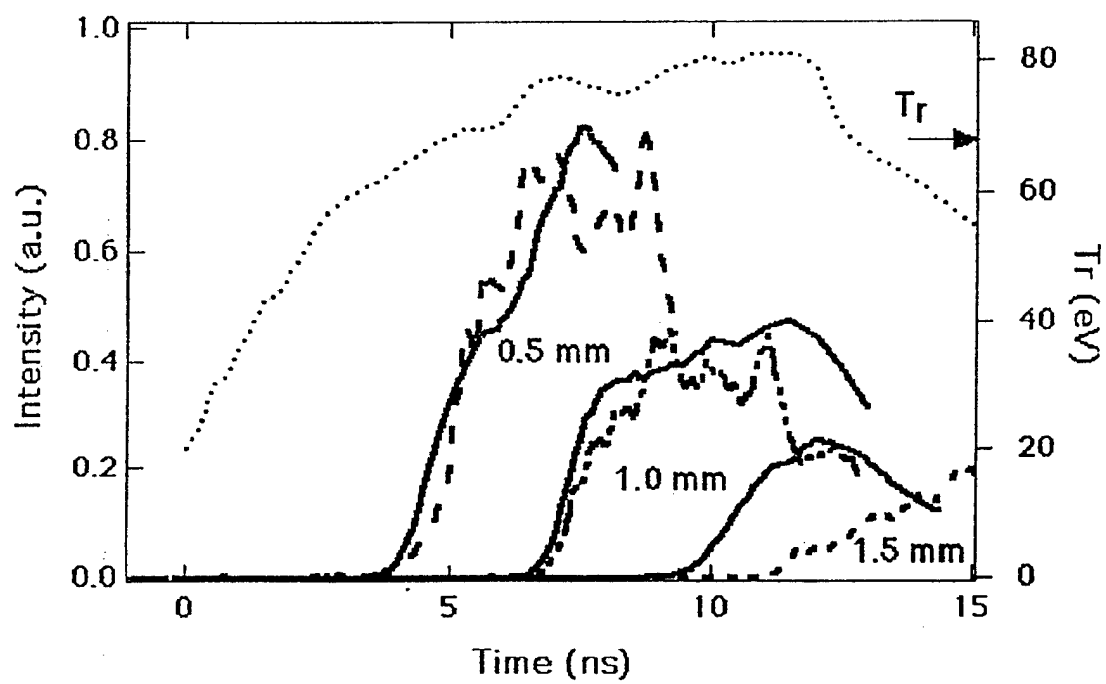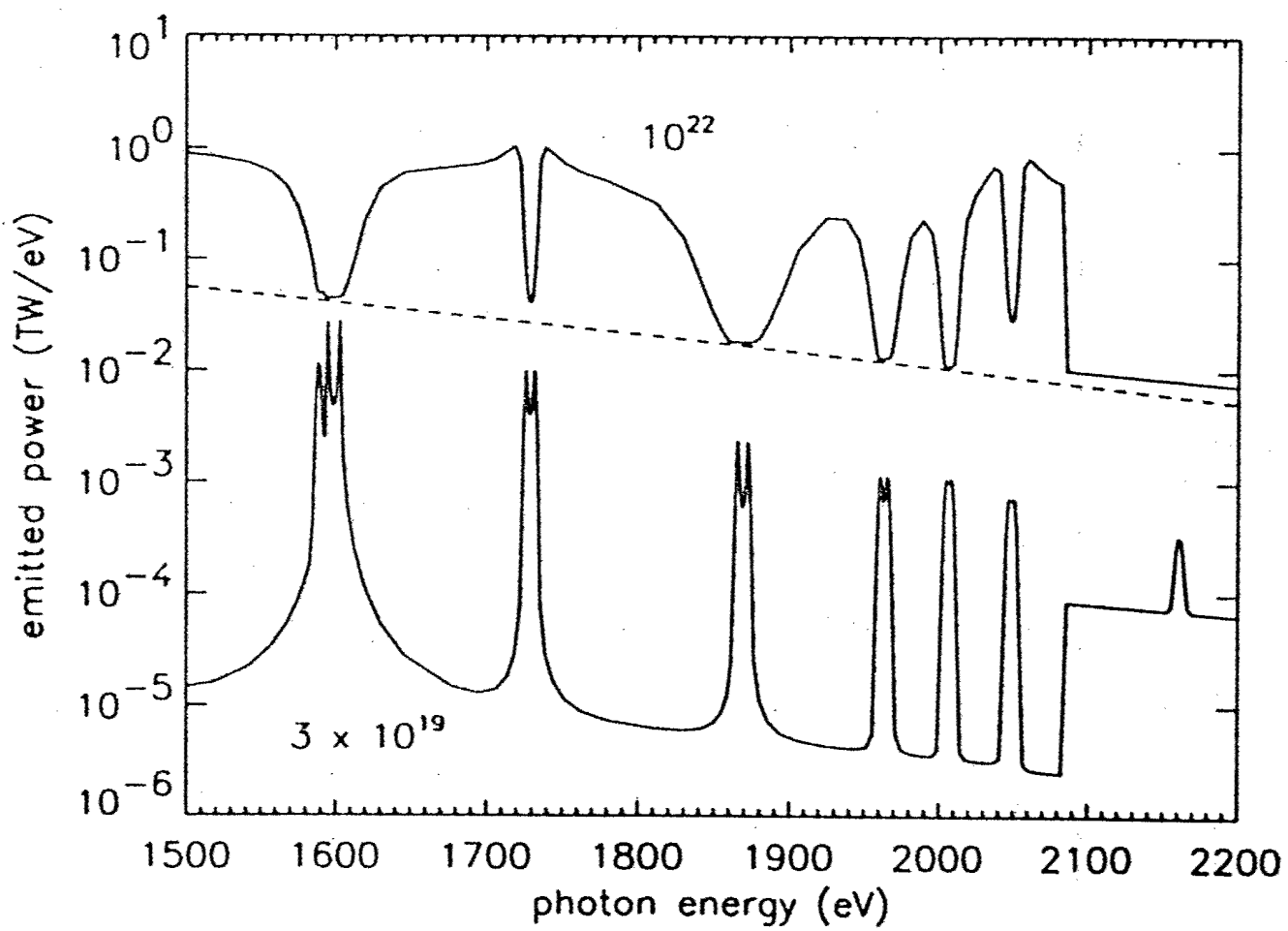
FIG. 1

FIG. 2

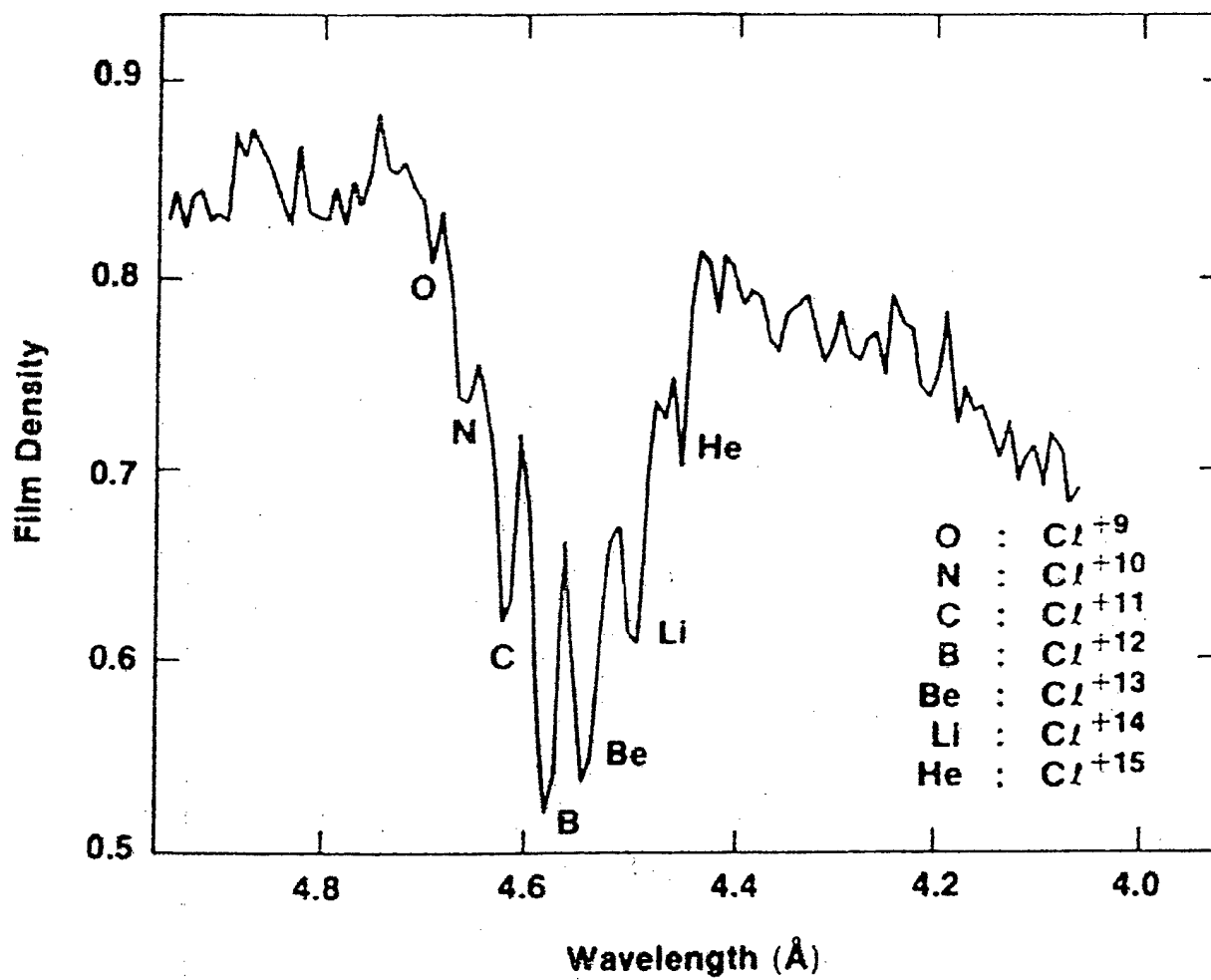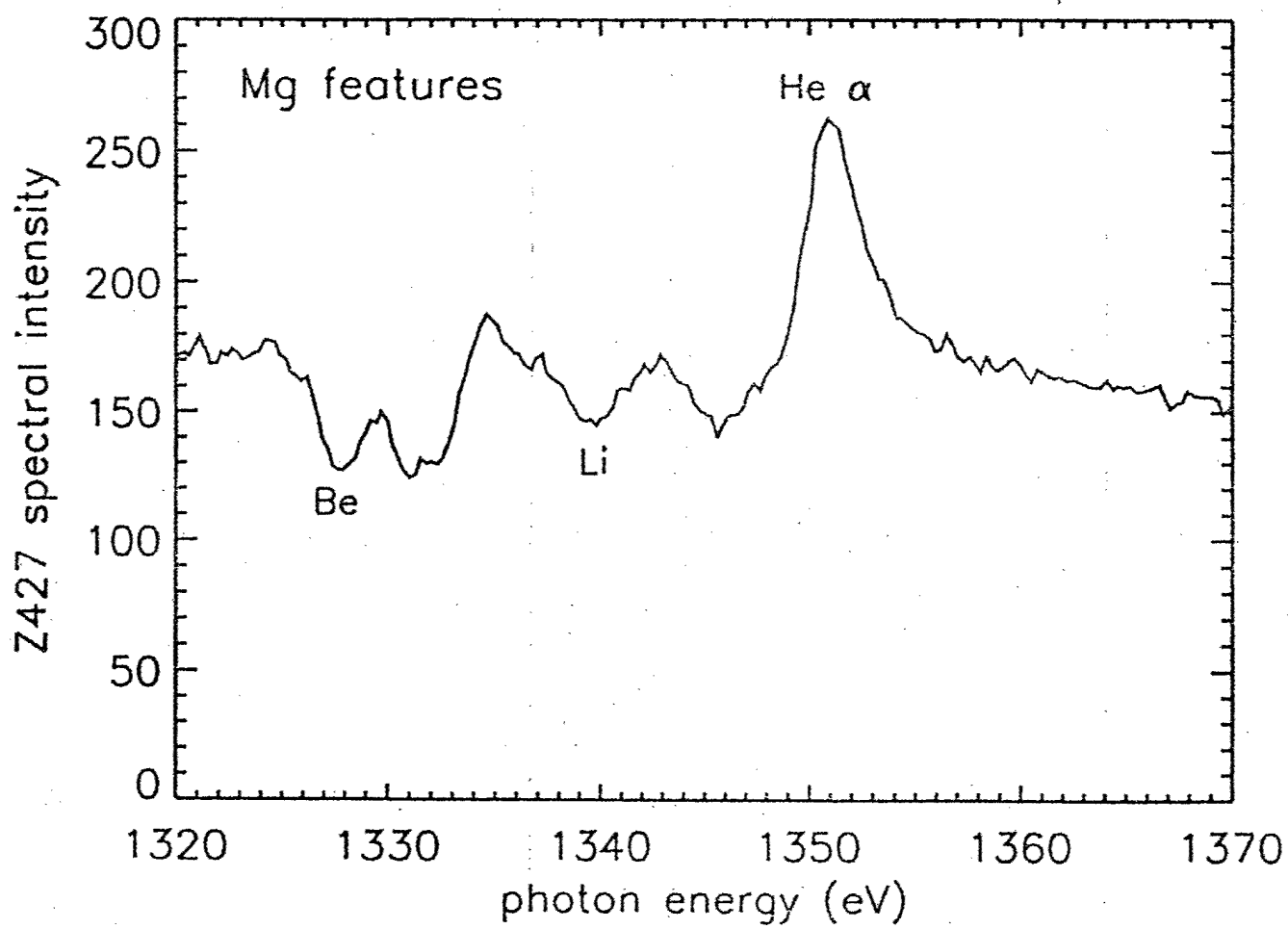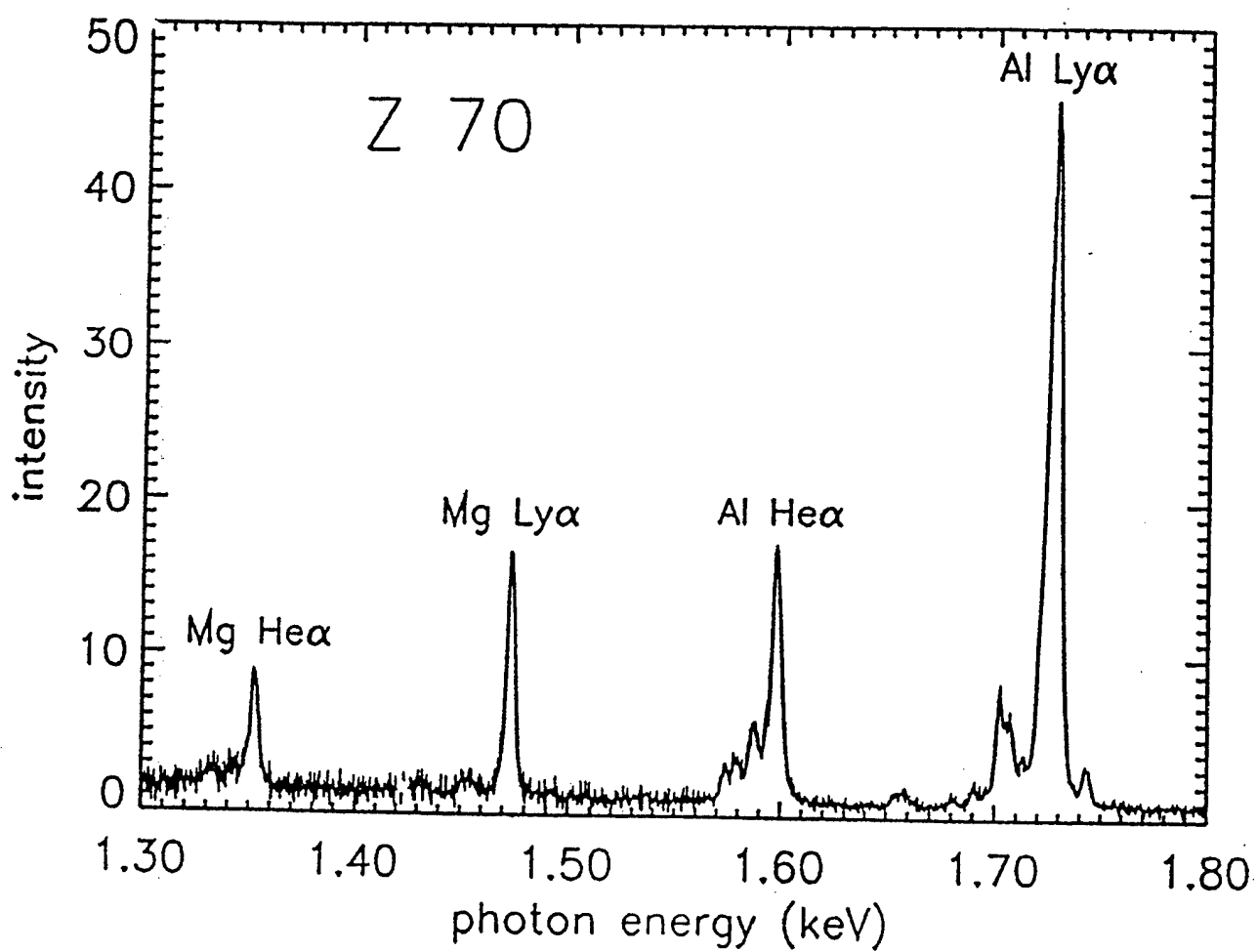FIG. 3

FIG. 4

68
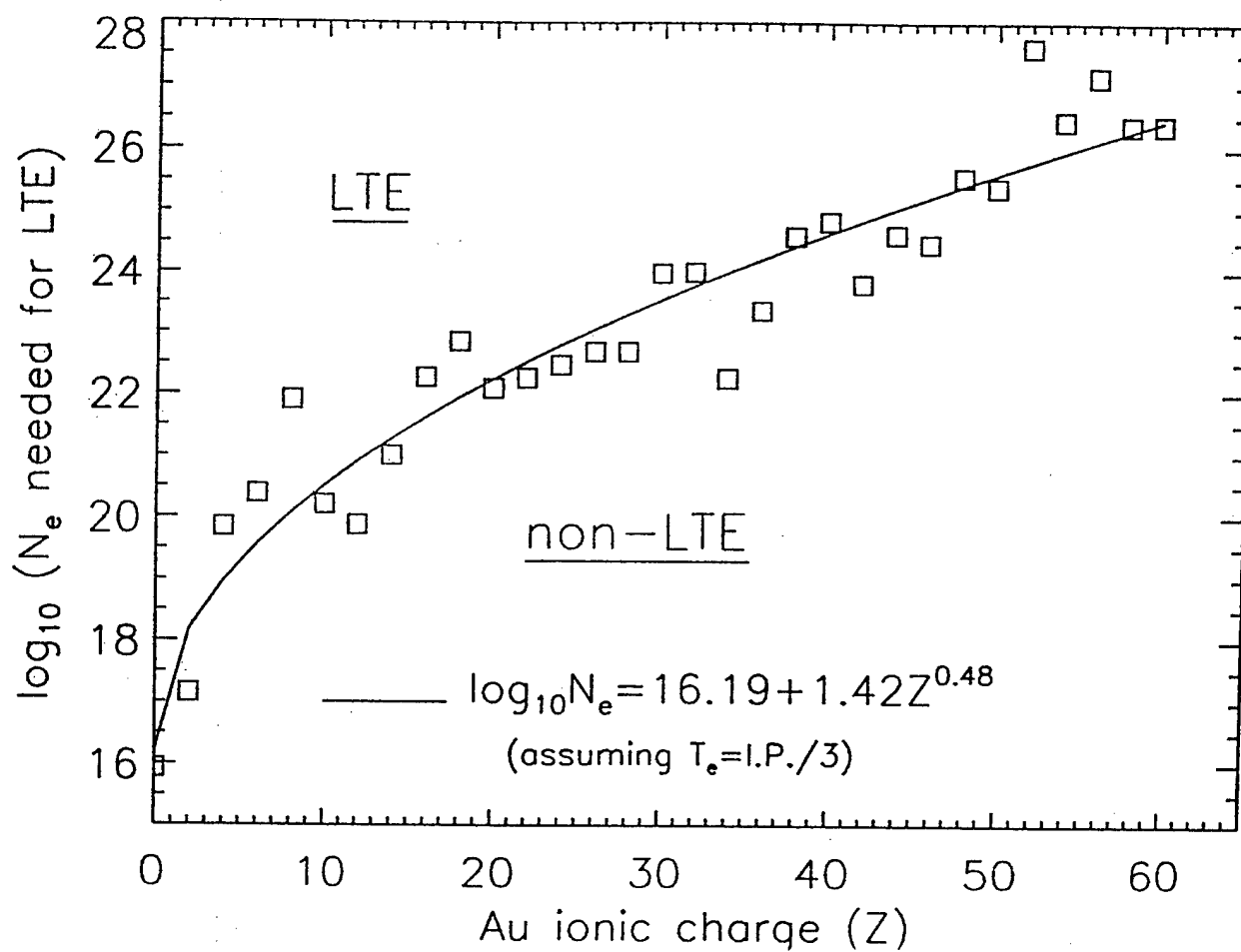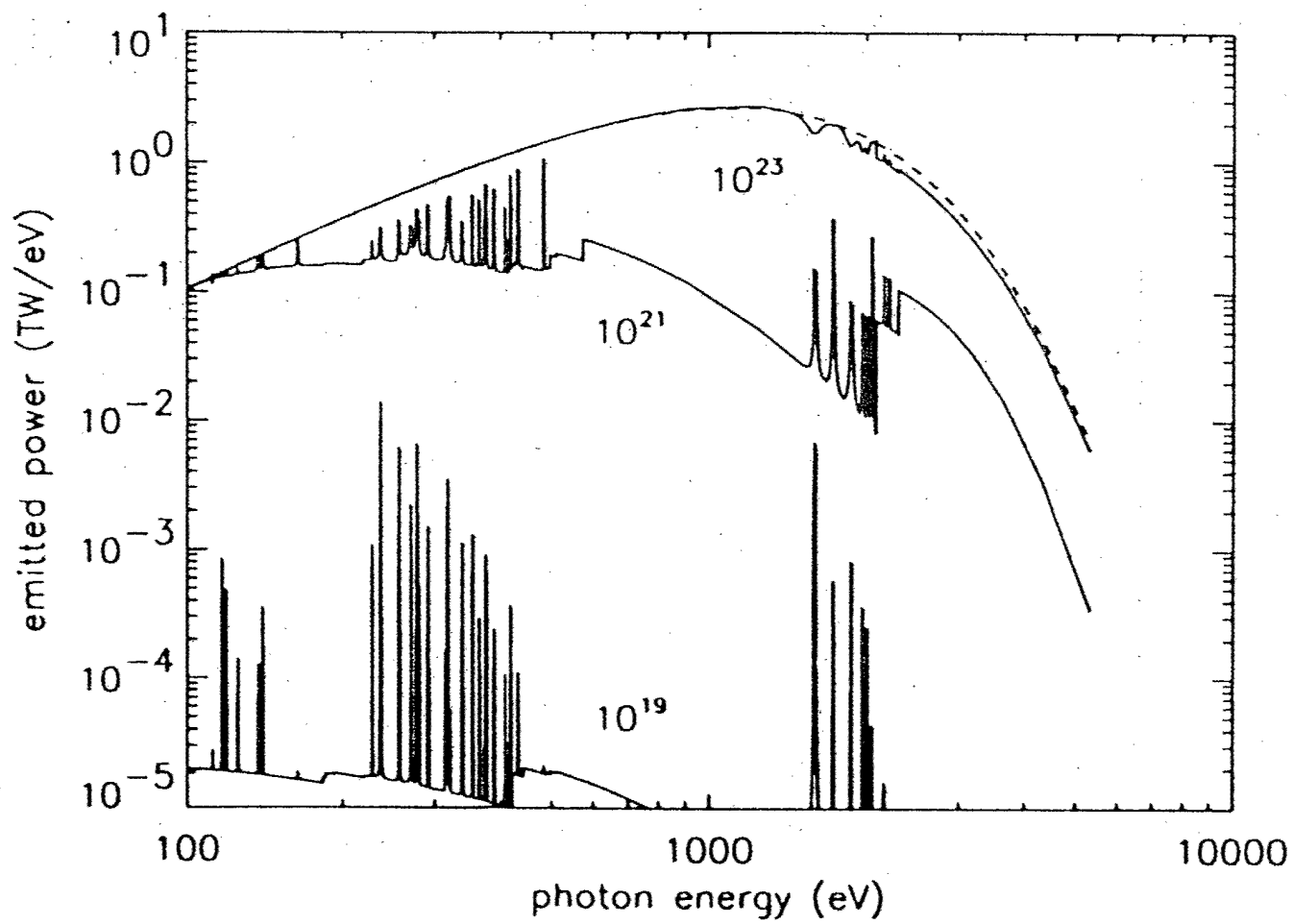
FIG. 5

FIG. 6

FIG. 7

FIG. 8

III. Perfectly conducting incompressible fluid model of a wire array implosion

I. Introduction

The achievements of high current Z pinch physics in recent years have been spectacular. Record values of total x-ray energy output ~2 MJ, peak total power >250 TW, argon (3.3 keV) and titanium (4.8 keV) K-shell yields over 270 and 125 kJ, respectively, have been produced on the 20 MA "Z" facility at Sandia National Laboratories.[1-3] To maximize the radiative performance of "Z" and other multi-MA current drivers, a careful design of the radiating loads is required. The actual Z-pinch plasma radiation sources (PRS) load designs used to obtain record-high yield and power emerged from a sustained effort of improving radiative properties of PRS through mitigating the Rayleigh-Taylor (RT) instability of implosion. The RT instability mitigation increases the radial compression of the pinch, and thereby the density of the radiating plasma, enhances the driver energy deposition to the plasma. The development of the gas-puff loads has progressed from annular puffs to uniform fills to the section of a gas jet produced by a recessed double-shell nozzle[3, 4] that combines the features of double shells and tailored density profiles.[5, 6] The wire array load design advanced through a significant increase in the number of wires in a cylindrical array,[7] and the use[1] of nested instead of single wire arrays.[8, 9]

To advance further in the wire array load design, a better understanding of the implosion physics is needed. Being essentially a three-dimensional (3-D) process,[10] a wire array implosion at the moment cannot be modeled numerically without sacrificing much of the relevant physics. Simplified two-dimensional (2-D) models permit more

detailed numerical and analytical investigation. The 2-D (r, z) MHD modeling is fairly advanced,[5, 11, 12] and capable of capturing many essential features of the implosions, including the growth of the fastest $m = 0$ RT and MHD instability modes and enhanced energy coupling to the pinch plasma.[11, 13] However, since a wire array load is not an annular plasma shell, at least initially,[14] there are some important phenomena affecting the radiative performance, which cannot be described by the 2-D (r, z) modeling. The most important of them are formation of the imploding plasma shell from the individual wire plasmas, ejection of the precursor plasma streams that converge to the axis prior to the implosion of the main plasma mass[15] and current splitting and/or switching between the components of the load in the nested wire arrays (including the case when it operates in the "transparent inner" mode)[8, 9, 16] or in hybrid loads like gas-puff-on-wire-array.[17] These 2-D effects have to be modeled on the (r, θ) plane.

The 2-D (r, θ) MHD modeling is possible (see Refs. 10, 14-16 and references therein) but still quite complicated. It is not certain yet how well the 2-D MHD can reproduce some essential features of implosions, such as collisions between plasma layers, reconnection of magnetic field and switching of current between components of a nested load. This is why simplified approaches could be helpful, like the simple wire-dynamic model[8, 9] used to study the implosion kinematics and current switching in nested wire array loads. The magnetostatic effects due to finite sizes of the wire plasmas are beyond the thin wire approximation used in Refs. 8, 9 and could only be treated numerically.[18]

Our present study extends the results of Refs. 8, 9, 18. We investigate the (r, θ) dynamics of finite-size perfectly conducting plasma columns in a periodic array.

Distribution of current density on the surfaces of the plasma columns and on the return current can, as well as the magnetic field in vacuum, are calculated self-consistently with the time-dependent cross-sectional shapes of the columns. This approach could be regarded as an alternative to the direct numerical integration of the MHD equations. Numerically, it is quite economical and has an attractive capacity of treating a plasma-vacuum boundary explicitly. Using the theory of analytic functions, one can describe 2-D plasma dynamics in the global magnetic field of the wire array by integrating one-dimensional (1-D) equations that refer to the field and plasma parameters on the surface of a plasma column. Thus we obtain a virtually exact solution, which provides a better insight into the physics of our simplified model. A similar analytical method has been applied in Ref. 19 to study non-linear dynamics of the free surface of an ideal fluid.

This paper is structured as follows. In Section II we derive the equations that self-consistently describe the shape and motion of perfectly conducting incompressible fluid columns on the (x, y) – same as (r, θ) – plane. Section III presents the derivation of magnetic field and current distributions and formulas for self- and mutual inductance for plasma columns arranged as in a single or nested wire array inside a cylindrical return current can. Dynamics of wire array implosions described by this model is investigated numerically in Section IV. In Section V, we conclude with a discussion.

I. Plasma dynamics

A. Formulation of the problem

Consider a two-dimensional - (x, y) or (r, θ) - motion of the wire plasmas during an implosion of a periodic N-wire array. The wire plasma is modeled as a perfectly

conducting, incompressible, irrotational, inviscid fluid. Physically, the assumption of perfect conductivity means that the current is concentrated in a thin skin layer on the plasma surface. This is not typical for high-current implosions, where the thickness of an imploding shell or individual wire is of the order of its skin depth, the magnetic Reynolds number being of order unity rather than very large, as required by the perfect conductivity assumption. The incompressibility assumption is not realistic either. Indeed, the plasma temperature during the run-in phase for most wire materials is controlled by radiation losses, and therefore the actual plasma density has to increase roughly as the magnetic pressure driving its implosion. Our plasma model is admittedly highly idealized and not directly applicable to the experimental conditions. The idealization of the problem, however, permits us to do study it analytically, highlighting certain physics issues relevant in the general case, as well as generating virtually exact solutions, which could be used, in appropriate parameter ranges, to benchmark the hydrocodes. It should be added that our results pertaining to magnetostatics (current splitting between the components of a nested wire array, distribution of the return current on the surface of a cylindrical can, etc.) are not sensitive to the distributions of current and mass in individual wires. The corresponding formulas are therefore applicable whenever the impedance of the wire array load is mainly inductive, see below.

Initially, the wires are cylindrical columns equidistantly distributed over a circle whose radius is $R_c(0)$. The initial rotational symmetry of the N-th order, as well as the translational symmetry with respect to the displacements along the z-axis, are supposed to be conserved during the implosion.

76

Denote the projection of the n-th plasma column onto the complex plane $z = x + iy$ at the moment t by $\mathrm{R}_n(t)$ with its boundary $\gamma_n(t)$. Due to the rotational symmetry of the system, one can write, omitting the subscript 1 for the first plasma column,

$$\gamma_n(t) = \gamma(t)\exp[2\pi i(n-1)/N]. \tag{1}$$

The Riemann theorem[20] states that while $\mathrm{R}(t)$ remains a simply connected domain, for any instant t there exists a conformal mapping $z = \Xi(z_0, t)$ of the interior of the unit circle, $|z_0| \leq 1$ on the complex plane $z_0 = x_0 + iy_0$ onto the interior of the domain $\mathrm{R}(t)$. The complex function $\Xi(z_0, t)$, as well as all its derivatives with respect to both arguments, z_0 and t, is analytic (moreover, $\partial\Xi(z_0, t)/\partial z_0 \equiv \Xi_{z0} \neq 0$) in the interior of the unit circle. This conformal mapping is determined by three parameters. Since the boundary of the unit circle $\exp(iu)$, $0 \leq u \leq 2\pi$, is mapped to the boundary contour, $\gamma(t)$, we can introduce a complex function of a real argument u that also defines the boundary of the domain $\mathrm{R}(t)$:

$$\gamma(t) = \Xi(e^{iu}, t) = \xi(u, t) = \varsigma(u, t) + i\lambda(u, t). \tag{2}$$

If the real axis x is the axis of symmetry of the domain $\mathrm{R}(0)$ at the initial moment, this mirror symmetry will be conserved at later time t due to the global rotational symmetry of the system. So one can assume that the points of the unit circle that belong to the real axis x_0 will be transformed by the conformal mapping Ξ to the points of the domain $\mathrm{R}(t)$ on the real axis x: At any moment t,

$$\mathrm{Im}[z = \Xi(z_0, t)] = 0 \quad \text{if} \quad \mathrm{Im}(z_0) = 0. \tag{3}$$

77

Thus we can fix two arbitrary parameters of the conformal mapping $z = \Xi(z_0, t)$ by

eliminating an arbitrary rotation with respect to the center of the unit circle $z_0 = 0$:

$$\lambda(t,0) = 0 \text{ and } \lambda(t,\pi) = 0. \tag{4}$$

Schwartz integral[20] recovers the value of an analytic function $\Xi(z_0, t)$ in the

interior of the domain $R(t)$ from the real part of its boundary value, $\varsigma(u,t)$:

$$\Xi(z_0,t) = \frac{1}{2\pi} \int_0^{2\pi} \varsigma(u,t) \frac{e^{iu} + z_0}{e^{iu} - z_0} du + iC, \tag{5}$$

where C is an arbitrary real constant. From Eqs. (2), (5) the imaginary part of the

complex function $\xi(u,t)$ can be expressed via its real part in terms of an integral operator

$\hat{H}$:

$$\lambda(u,t) = \hat{H}\varsigma(u,t) = \int_0^{2\pi} \varsigma(w,t) \cot\left(\frac{u-w}{2}\right) dw + C. \tag{6}$$

The time derivative of the function $\xi(u,t)$ is the boundary value of another

analytic function, $\Xi_t \equiv \partial\Xi(z_0,t)/\partial t$:

$$\frac{\partial}{\partial t}\xi(u,t) \equiv \xi_t = \Xi_t(e^{iu},t) = V(u,t), \tag{7}$$

where $V(u,t)$ is the complex velocity of the point of the boundary contour with

coordinate u. This complex vector can be expressed through its real components, $V_\parallel$ and

$V_\perp$:

$$V(u,t) = \mathbf{e}_\parallel V_\parallel(u,t) + \mathbf{e}_\perp V_\perp(u,t). \tag{8}$$

Here, $\mathbf{e}_\parallel$ and $\mathbf{e}_\perp$ are complex unit vectors, and the frame of reference is tied to the contour

$\xi(u,t)$, see Fig. 1:

$$\mathbf{e}_\parallel = \frac{\xi_u}{|\xi_u|}, \quad \mathbf{e}_\perp = i\frac{\xi_u}{|\xi_u|}, \quad \xi_u \equiv \frac{\partial}{\partial u}\xi(u,t). \tag{9}$$

The components of the complex velocity are readily expressed via ξ and its derivatives:

$$V_\parallel(u,t) = \mathrm{Re}(\xi_t\bar{\mathbf{e}}_\parallel) = |\xi_u|\,\mathrm{Re}(\xi_t/\xi_u), \tag{10}$$

$$V_\perp(u,t) = \mathrm{Re}(\xi_t\bar{\mathbf{e}}_\perp) = -|\xi_u|\,\mathrm{Re}(i\xi_t/\xi_u). \tag{11}$$

In Eqs. (10)-(11) and below, the bar denotes a complex conjugate value: $\bar{z} = x - iy$.

On the complex plane $z = x + iy$ a potential flow of an incompressible fluid in the domain $z \in \mathsf{R}(t)$ is described by two real functions of complex argument: the velocity potential $\Phi(z,t)$ and the stream function $\Theta(z,t)$:

$$v_x = \frac{\partial \Phi}{\partial x} = \frac{\partial \Theta}{\partial y}, \quad v_y = \frac{\partial \Phi}{\partial y} = -\frac{\partial \Theta}{\partial x}, \tag{12}$$

where v_x and v_y are, respectively, real and imaginary part of the complex velocity of the fluid, $v = v_x + iv_y$. The fluid is incompressible ($\nabla \cdot \mathbf{v} = 0$) and irrotational ($\nabla \times \mathbf{v} = 0$), which implies that both functions satisfy the Laplace equation:

$$\nabla^2\Phi = 0, \quad \nabla^2\Theta = 0. \tag{13}$$

Defining the complex velocity potential as

$$X(z,t) = \Phi(z,t) + i\Theta(z,t), \tag{14}$$

we find that Eqs. (12) are the Cauchy-Riemann conditions which ensure that the complex function $X(z,t)$ and all its derivatives with respect to both arguments are analytic functions in the domain $\mathsf{R}(t)$.

The velocity potential $\Phi(z,t)$ at the boundary of the domain $\mathsf{R}(t)$ could be expressed as a function of the coordinate u and time:

$$\Phi(\xi(u,t),t) = \Psi(u,t). \tag{15}$$

This equation is generalized for the complex velocity potential in terms of the integral operator $\hat{H}$ introduced in Eq. (6):

$$X(\xi(u,t),t) = (1 + i\hat{H})\Psi(u,t). \tag{16}$$

The analytic function $\partial X / \partial z$ and the complex velocity of the fluid are complex conjugate functions in $R(t)$:

$$\frac{\partial}{\partial z} X(z,t) = \bar{v}(z,t), \quad z \in R(t). \tag{17}$$

Thus $v(z,t)$ is an anti-analytic function in $R(t)$, its real and imaginary parts satisfying the Cauchy-Riemann conditions with inverted signs [e. g., compared to (12)]. The boundary value of the analytic function $\bar{v}(z,t)$ at the point u is

$$\bar{v}(\xi(u,t),t) = \left.\frac{\partial X}{\partial z}\right|_{z=\xi} = \frac{1}{\xi_u}(1 + i\hat{H})\Psi_u(u,t), \tag{18}$$

because the integral operator $\hat{H}$ is commutative with the differential operator $\partial / \partial u$:

$$\frac{\partial}{\partial u}\hat{H}\Psi(u,t) = \hat{H}\frac{\partial}{\partial u}\Psi(u,t) \equiv \hat{H}\Psi_u. \tag{19}$$

With the aid of Eq. (9) we express the boundary value of the fluid velocity via its real components $v_{\parallel}$ and $v_{\perp}$ as

$$v(\xi(u,t),t) = e_{\parallel}v_{\parallel}(u,t) + e_{\perp}v_{\perp}(u,t), \tag{20}$$

where the longitudinal component $v_{\parallel}(u,t)$ equals

$$v_{\parallel}(u,t) = \mathrm{Re}\left(e_{\parallel}\bar{v}(\xi,t)\right) = \mathrm{Re}\left(\frac{\xi_u}{|\xi_u|}\left.\frac{\partial X}{\partial z}\right|_{z=\xi}\right) = \frac{\Psi_u}{|\xi_u|}, \tag{21}$$

and the normal component $v_{\perp}(u,t)$ equals

$$v_\perp(u,t) = \text{Re}\big(e_\perp \bar{v}(\xi,t)\big) = -\frac{\hat{H}\Psi_u}{|\xi_u|}.\tag{22}$$

B. Equation of motion for the fluid contour

In Section II.A two complex functions have been introduced at the point of the boundary contour ξ with coordinate u: the velocity of motion of this point, $V(u,t)$, and the fluid velocity at this point, $v(\xi(u,t),t)$. Generally, they are not equal to each other, $V(u,t) \neq v(\xi(u,t))$. Indeed, the first function characterizes the conformal mapping $\Xi(z_0,t)$, and the second one is the physical velocity. Moreover, $V(u,t)$ is the boundary value of an analytic function Ξ_t, whereas the function $v(z,t)$ is anti-analytic in $R(t)$. Nevertheless, in the reference frame (9) tied to the contour ξ, the normal components of these two velocities are the same: $v_\perp(u,t) = V_\perp(u,t)$. Therefore, the equation of motion for the contour follows from (11) and (22):

$$\text{Re}\left(\frac{i\xi_t}{\xi_u}\right) = \frac{\hat{H}\Psi_u}{|\xi_u|^2}.\tag{23}$$

The left-hand side of Eq. (23) is the real part of the boundary value of a function $g(z_0,t)$, which is defined in the interior of the unit circle, $|z_0| \leq 1$:

$$\frac{i\xi_t(u,t)}{\xi_u(u,t)} = g(z_0,t)\big|_{z_0=\exp(iu)}.\tag{24}$$

Since $\xi(u,t)$ is the boundary value of $\Xi(z_0,t)$ on the unit circle $z_0 = e^{iu}$, the following relations hold:

81

$$\xi_t(u,t) = \Xi_t(z_0,t)\big|_{z_0 = \exp(iu)},$$
(25)

$$\xi_u(u,t) = \left(\frac{\partial z_0}{\partial u}\frac{\partial \Xi}{\partial z_0}\right)_{z_0 = \exp(iu)} = \left(iz_0\Xi_{z_0}\right)_{z_0 = \exp(iu)}.$$
(26)

In Eq. (26) the dependence $z_0(u) = e^{iu}$, initially defined on the unit circle boundary

$|z_0| = 1$, was analytically continued in the interior of the unit circle, so that $z_0 = |z_0|e^{iu}$,

and $\partial z_0 / \partial u = iz_0$ for $|z_0| \leq 1$. Thus we have:

$$g(z_0,t) = \frac{1}{z_0} \times \frac{\Xi_t(z_0,t)}{\Xi_{z_0}(z_0,t)}, \qquad |z_0| \leq 1.$$
(27)

Obviously, $g(z_0,t)$ is not an analytic function in the interior of the unit circle, since it has

a pole $\sim 1/z_0$ at the point $z_0 = 0$ (note that $\Xi_{z_0} \neq 0$ for $|z_0| \leq 1$). However, one can

construct an auxiliary function $G(z_0,t)$ that is analytic in the unit circle:

$$G(z_0,t) = g - \frac{1}{z_0} \times \lim_{z_0 \to 0}\left(z_0 g\right) = g(z_0,t) - \frac{F(t)}{z_0},$$
(28)

where

$$F(t) = \frac{\Xi_t(z_0,t)\big|_{z_0=0}}{\Xi_{z_0}(z_0,t)\big|_{z_0=0}}$$
(29)

is a real-valued function, see below. Substituting $g(e^{iu},t)$ expressed via $G(e^{iu},t)$ into Eq.

(23), we obtain:

$$\text{Re}\left(i\frac{\xi_t}{\xi_u} - F(t)e^{-iu}\right) = \frac{\hat{H}\Psi_u}{|\xi_u|^2} - F(t)\cos u.$$
(30)

Since the function $G(z_0, t)$ is analytic in the interior of the unit circle $|z_0| \leq 1$, the imaginary part of its boundary value can be recovered from its real part by applying the integral operator $\hat{H}$ to both sides of Eq. (30):

$$\operatorname{Im}\left(i\frac{\xi_t}{\xi_u} - F(t)e^{-iu} \right) = \hat{H}\frac{\hat{H}\Psi_u}{|\xi_u|^2} - F(t)\sin u \, . \tag{31}$$

Summing Eqs. (30) and (31), we obtain the equation for the evolution of the function $\xi(u, t)$:

$$V(u, t) = \xi_t = \xi_u\left[(\hat{H} - i)\frac{\hat{H}\Psi_u}{|\xi_u|^2} - 2F(t)\sin u \right]. \tag{32}$$

From Eq. (10), we find the longitudinal component of the velocity of the point with coordinate u on the boundary contour $\xi(u, t)$:

$$V_{\parallel} = |\xi_u|\left[\hat{H}\frac{\hat{H}\Psi_u}{|\xi_u|^2} - 2F(t)\sin u \right]. \tag{33}$$

The denominator of the right-hand side of Eq. (29) is a function of time:

$$\Xi_{z_0}(z_0, t)\Big|_{z_0=0} = f(t) \, . \tag{34}$$

This function could be found by integrating the function $\Xi_{z_0}(z_0, t)$, which is analytic in the circle $|z_0| \leq 1$, over the contour $z_0 = e^{iu}$, using the mean-value theorem:

$$f(t) = \frac{1}{2\pi}\int_0^{2\pi}\left(\Xi_{z_0}\right)_{z_0=\exp(iu)} du = \frac{1}{2\pi i}\int_0^{2\pi}\xi_u e^{-iu} du \, . \tag{35}$$

If the contour $\xi(u, t)$ is symmetrical with respect to the real axis x, then

$$f(t) = \frac{1}{2\pi}\int_0^{2\pi}\left[\left(\hat{H}\varsigma_u\right)\cos u - \varsigma_u \sin u \right] du \, . \tag{36}$$

83

The numerator of the right-hand side of Eq. (29) is the velocity $V_c(t)$ of the point $z_c(t) = \Xi(0,t)$ representing the image of the center of the unit circle:

$$\Xi_t(z_0,t_0)\big|_{z_0=0} = \frac{d}{dt}z_c(t) = V_c(t). \tag{37}$$

According to Eq. (4), the easiest way to define the position of the point z_c is the following:

$$z_c(t) = \frac{1}{2}\left[\varsigma(0,t) + \varsigma(\pi,t)\right]. \tag{38}$$

Equation (38) ensures that the point z_c always remains within the domain $R(t)$, as long as it remains simply connected. Postulating (38), we fix the last free parameter of the conformal mapping $z = \Xi(z_0,t)$ [the other two have been fixed by Eq. (4)]. The velocity $V_c(t)$ is found from Eq. (38):

$$V_c(t) = \frac{1}{2}\left[\varsigma_t(0,t) + \varsigma_t(\pi,t)\right]. \tag{39}$$

E. g., for a uniform distribution of the fluid velocity, $v(z,t) = v_0$, where v_0 is a real constant, Eq. (32) yields a solution $V(u,t) = v_0$ provided that $V_c(t)$ is defined by (39); see Appendix A. Obviously, the functions $f(t)$, $z_c(t)$, and, consequently, $V_c(t)$ and $F(t) = V_c(t)/f(t)$ are real-valued.

In order to reduce the number of parameters, we re-write the equation of motion for the fluid contour (32) in terms of the function $\xi_u(u,t)$:

$$\frac{\partial \xi_u}{\partial t} = \frac{\partial}{\partial u}\left[\xi_u\left(\hat{H} - i\right)\frac{\hat{H}\Psi_u}{|\xi_u|^2} - 2F(t)\xi_u \sin u\right]. \tag{40}$$

Separating the real part of Eq. (40), we derive the equation sought for:

84

$$\frac{\partial \varsigma_u}{\partial t} = \frac{\partial}{\partial u}\left[\varsigma_u\left(\hat{H}\frac{\hat{H}\Psi_u}{\varsigma_u^2 + (\hat{H}\varsigma_u)^2} - 2F(t)\sin u\right) + \frac{(\hat{H}\varsigma_u)(\hat{H}\Psi_u)}{\varsigma_u^2 + (\hat{H}\varsigma_u)^2}\right]. \tag{41}$$

The imaginary part of ξ, $\lambda(u,t)$, is found from (6).

C. Equation for the velocity potential

The partial time derivative of the contour function (15) $\Psi(u,t)$ is expressed via the time derivative of the complex velocity potential $X(z,t)$ on the boundary contour $\xi(u,t)$:

$$\frac{\partial}{\partial t}\Psi(u,t) = \frac{\partial}{\partial t}\mathrm{Re}[X(\xi(u,t),t)] = \frac{\partial \Phi}{\partial t}\bigg|_{z=\xi} + \mathrm{Re}\left[\frac{\partial X}{\partial z}\bigg|_{z=\xi}\frac{\partial \xi}{\partial t}\right]. \tag{42}$$

In the interior of the domain $\mathsf{R}(t)$ the dynamics of the incompressible inviscid fluid is described by the Bernoulli integral

$$\frac{\partial}{\partial t}\Phi(z,t) + \frac{1}{2}|v(z,t)|^2 + \frac{1}{\rho}P(z,t) = a(t), \tag{43}$$

where $P(z,t)$ is the pressure of the fluid, ρ is the constant fluid density, and $a(t)$ is some function of time. We can express the time derivative of the velocity potential on the boundary contour from (43)

$$\frac{\partial \Phi}{\partial t}\bigg|_{z=\xi} = a(t) - \frac{1}{2}\left(v_\|^2 + v_\perp^2\right) - \frac{p}{\rho}, \tag{44}$$

where $p(u,t) = P(\xi(u,t),t)$ is the fluid pressure on the boundary contour $\xi(u,t)$. On the other hand, the second term on the right-hand side of (42) is a scalar product of two complex vectors, $v(\xi(u,t),t)$ and $V(u,t)$:

$$\text{Re}\left[\left.\frac{\partial X}{\partial z}\right|_{z=\xi} \frac{\partial \xi}{\partial t}\right] = v_\| V_\| + v_\perp V_\perp . \tag{45}$$

Substituting Eqs. (44) and (45) into (42), we obtain an evolution equation for the contour function $\Psi(u,t)$:

$$\frac{\partial \Psi}{\partial t} = a(t) + \Psi_u \left(\hat{H} \frac{\hat{H}\Psi_u}{\varsigma_u^2 + (\hat{H}\varsigma_u)^2} - 2F(t)\sin u\right) + \frac{1}{2}\frac{(\hat{H}\Psi_u)^2 - \Psi_u^2}{\varsigma_u^2 + (\hat{H}\varsigma_u)^2} - \frac{p}{\rho} . \tag{46}$$

The yet unknown function of time, $a(t)$, vanishes from the equation for the evolution of the derivative, $\Psi_u(u,t)$:

$$\frac{\partial \Psi_u}{\partial t} = \frac{\partial}{\partial u}\left[\Psi_u \left(\hat{H} \frac{\hat{H}\Psi_u}{\varsigma_u^2 + (\hat{H}\varsigma_u)^2} - 2F(t)\sin u\right) + \frac{1}{2}\frac{(\hat{H}\Psi_u)^2 - \Psi_u^2}{\varsigma_u^2 + (\hat{H}\varsigma_u)^2} - \frac{p}{\rho}\right] \tag{47}$$

Equations (41) and (47) form a closed system of integro-differential equations, which describe the evolution of the contour functions, $\varsigma_u(u,t)$ and $\Psi_u(u,t)$. Evolution of this system satisfies the following conservation law

$$\frac{d}{dt}\oint_{z=\xi}\Phi\,dz + \oint_{z=\xi}\frac{P}{\rho}\,dz = 0, \tag{48}$$

which ensures conservation of the total momentum of the system, see Appendix B.

The perfectly conducting fluid approximation means that the magnetic field does not penetrate into the plasma column, and the electric current is concentrated in the infinitely thin skin layer adjacent to the boundary contour $\xi(u,t)$ with surface density

86

$J(u,t)$. Each wire carries $1/N$ of the total current $I(t)$, which is expressed by the normalization condition

$$\int_0^{2\pi} J(u,t)\,|\xi_u(u,t)|\,du = \frac{I(t)}{N}.$$ (49)

In the exterior vicinity of the contour, only the longitudinal component of the magnetic field is induced by the electric current:

$$\mathbf{B}(z,t)\big|_{z\to\xi(u,t)} = \mathbf{e}_\parallel B_\parallel(u,t), \quad z \notin \mathsf{R}(\mathbf{r}),$$ (50)

where

$$B_\parallel(u,t) = \mu_0 J(u,t).$$ (51)

The sum of magnetic and hydrodynamic pressure should be continuous through the thin skin layer, hence the fluid pressure under the skin layer is determined by the local surface current density:

$$p(u,t) = \frac{1}{2\mu_0} B_\parallel^2(u,t) = \frac{\mu_0}{2} J^2(u,t).$$ (52)

The procedure for calculating the distribution of current density $J(u,t)$ for any given contour $\xi(u,t)$ is described in the next Section.

We have shown that the 2-D dynamics of the wire plasma in this model is described by two coupled 1-D integro-differential evolution equations (41) and (47). It must be supplemented by the procedure of determining the distribution of current density on the surface of the plasma column self-consistently for its given position and the shape of its horizontal cross section.

Our approach has much in common with one developed in Ref. 19. Regularization of the singularity at $z_0 = 0$ is done differently here, which makes it possible for us to

update the numerical solution for a longer time. The original formalism of Ref. 19 would not be applicable here for a wire displacement exceeding its initial diameter: the singularity would move through the boundary contour. The system of hydrodynamic equations derived in Ref. 19 contained three equations, with two of them being harmonically conjugated. For this system, we were unable to obtain a stable numerical solution even using a Lax-Friedrichs scheme with the highest possible numerical dissipation. Such a system does not seem to be similar to a hyperbolic system of conservation equations. On the other hand, our system of two equations (41) and (47) has two characteristic velocities (Alfvén velocity with positive and negative signs), and in this sense resembles a hyperbolic system. Its numerical integration is sufficiently simple.

Some mathematical methods developed for the study of interfacial hydrodynamic instabilities[21] were used in the derivations presented in the Appendices.

III. Magnetostatics

A. Equation and boundary conditions for the magnetic vector potential

The results of Section II apply to an arbitrary 2-D potential motion of a perfectly conducting, incompressible fluid. Here we use the N-th order rotational symmetry to find the distribution of current on the surface of each plasma column, and hence, the magnetic pressure that drives the implosion.

The magnetic field $\mathbf{B}$ is expressed via the vector potential $\mathbf{A}$:

$$\mathbf{B} = \nabla \times \mathbf{A}, \quad \nabla \cdot \mathbf{A} = 0. \tag{53}$$

Neglecting the displacement currents, we arrive to the quasi-static (in our particular case, magnetostatic) approximation: from the Maxwell equation $\nabla \times \mathbf{B} = \mu_0 \mathbf{J}$, in vacuum,

where there is no current density, and (53), we find that the magnetic vector potential satisfies the Laplace equation:

$$\nabla^2 \mathbf{A} = 0. \tag{54}$$

If the current density $\mathbf{J}$ is directed along the wires, as is the case for a wire array without axial magnetic field, then the vector potential has only one nonzero component in the same direction, $A(z,t)$, where, as above, $z = x + iy$. The magnetic field $\mathbf{B} = B_x \mathbf{e}_x + B_y \mathbf{e}_y$, where

$$B_x = \frac{\partial A}{\partial y} \quad \text{and} \quad B_y = -\frac{\partial A}{\partial x}. \tag{55}$$

The current density is assumed below to be composed of a large number of discrete thin current filaments. Therefore, $A(z,t)$ is a real part of an analytic function with a large number of logarithmic singularities located at the positions of the current filaments.

The wire array is enclosed in a cylindrical, perfectly conducting return current can, whose radius is R_r. The vector potential of the return current can is assumed zero. The value of the vector potential at the surface of the plasma columns, $A(\xi,t) = \Lambda(t)$ has a clear physical meaning:

$$\phi = \int \mathbf{B} \cdot d\mathbf{S} = -l \int \frac{\partial A}{\partial r} dr = l\Lambda(t) \tag{56}$$

and

$$\frac{d}{dt}\phi = l\frac{d}{dt}\Lambda(t) = -\int [\nabla \times \mathbf{E}] \cdot d\mathbf{S} = U. \tag{57}$$

where ϕ is the magnetic flux, l is the length of the wire array, U is the voltage applied to it. The integration contour in Eqs. (56), (57) consists of two parallel straight lines, one on

the plasma column surface, another on the return current can surface. For a single conductor carrying a current I inside a return current can, the inductance per unit length is defined as

$$\frac{L}{l} = \frac{\phi}{Il} = \frac{\Lambda(t)}{I}.$$ (58)

Direct calculation of the energy integral gives:

$$W = \frac{1}{2\mu_0} \int B^2 dV = \frac{1}{2} \frac{(l\Lambda)^2}{L},$$ (59)

which illustrates that the inductance is positive definite.[22] This is readily generalized for a system of parallel straight conductors inside the same return current can. Then instead of Eq. (58) we obtain:

$$L_{jk} I_k = l\Lambda_j.$$ (60)

(Here and below, summation over repeated indices is implied.) The inductance matrix L_{jk} is symmetric and positive definite.[22] Such a matrix can always be inverted, and efficient numerical methods for its inversion are available.

B. Vector potential of current filaments in a cylindrical can

Introduce an elementary current $\delta I_n(u,t)$ flowing in the interval $[u - \delta u / 2, u + \delta u / 2]$ of the contour $\xi_n(u,t)$. Due to the rotational symmetry, $\delta I_n(u,t) = \delta I(u,t)$ (recall that the subscript referring to the first contour is omitted). The current filament δI_n generates the magnetic vector potential satisfying the boundary condition $\delta A_n(z,t) = 0$ at the return current can, $|z| = R_r$:

$$\delta A_n = \mathrm{Re}(\delta Y_n) = \frac{\mu_0}{2\pi} \delta I_n \mathrm{Re}\left[\ln \frac{R_r^2 - \bar{\xi}_n z}{R_r(z - \xi_n)} \right] = \frac{\mu_0}{2\pi} \delta I \ln \frac{|R_r^2 - \bar{\xi}_n z|}{R_r |z - \xi_n|}.$$ (61)

Here, the magnetic vector potential generated by a single elementary filament is presented as a real part of a function δY_n which is analytic in the exterior of the conducting contour $\xi_n(u,t)$. This feature of Eq. (61) helps in summation of the corresponding contributions from all the other wires in the array. Taking into account that

$$\prod_{n=1}^{N}\left[z-\xi\exp\left(2\pi i\frac{n-1}{N}\right)\right]=z^N-\xi^N,$$

(62)

we obtain

$$\delta A(z,t)=\sum_{n=1}^{N}\delta A_n=\frac{\mu_0}{2\pi}\delta I\ln\frac{|R_r^{2N}-(\bar{\xi}z)^N|}{R_r^N|z^N-\xi^N|}.$$

(63)

For large number of wires, the inequality $\left(|\xi|/R_r\right)^N\ll 1$ is satisfied, so that Eq. (63) reduces to

$$\delta A(z,t)=\frac{\mu_0}{2\pi}\delta I\ln\frac{R_r^N}{|z^N-\xi^N|}.$$

(64)

This approximation can be used if the plasma column is not too close to the return current can.

The vector potential δA given by (63) is the real part of an analytic function δY. Equation (63) could be used to determine the distribution of return current density on the can surface, $J_r(\varphi,t)$, where φ is the coordinate on this surface: $z=R_r e^{i\varphi}$:

$$\delta J_r=\frac{1}{\mu_0}\frac{\partial}{\partial r}\delta A=\frac{1}{\mu_0 R_r}\frac{\partial}{\partial\varphi}\text{Im}(\delta Y)=-\frac{N\delta I}{2\pi R_r}\frac{R_r^{2N}-|\xi|^{2N}}{|R_r^N-\xi^N\exp(-iN\varphi)|^2}.$$

(65)

The average density of the return current $\langle\delta J_r\rangle=-N\delta I/(2\pi R_r)$ corresponds to the total return current $-N\delta I$, which fully balances the elementary currents of all wires, as it should. The return current density varies between the minimum and maximum values

equal to $\langle \delta J_r \rangle (R_r^N - |\xi|^N)/(R_r^N + |\xi|^N)$ and $\langle \delta J_r \rangle (R_r^N + |\xi|^N)/(R_r^N - |\xi|^N)$, respectively,

where $r = |\xi|$ correspond to the center-of-mass position of the wires. The maximums are

located exactly opposite the wires, the minimums – between them. Variation of the return

current density is negligible provided that $\left(|\xi|/R_r\right)^N \ll 1$, i. e. when the approximation

(64) applies.

The total contribution to the vector potential from all the contour currents could

be found from integrating (63) over the coordinate u:

$$A(z,t) = \frac{\mu_0}{2\pi} \int_0^{2\pi} J |\xi_u| \ln \frac{|R_r^{2N} - (\bar{\xi}z)^N|}{R_r^N |z^N - \xi^N|} du .$$ (66)

Substitution of (66) into the boundary condition for the magnetic vector potential on the

plasma column $A(\xi,t) = \Lambda(t)$ yields the integral equation

$$\Lambda(t) = \frac{\mu_0}{2\pi} \int_0^{2\pi} J |\xi_u| \ln \frac{|R_r^{2N} - [\bar{\xi}(u,t)\xi(w,t)]^N|}{R_r^N |\xi(w,t)^N - \xi(u,t)^N|} du$$ (67)

which holds for any w between 0 and 2π. Solving (67) for the current density $J(u,t)$ and

applying the normalization condition (49), we find both the distribution of the current

density and the inductance from Eq. (58). The return current density $J_r(\varphi,t)$ is expressed

as

$$J_r(\varphi,t) = -\frac{N}{2\pi R_r} \int_0^{2\pi} \frac{J |\xi_u| (R_r^{2N} - |\xi|^{2N})}{|R_r^N - \xi^N \exp(-iN\varphi)|^2} du .$$ (68)

C. Thin wire approximation for single and nested arrays

Before describing a general method that we use for solving the integral equation

(67), consider an important approximation which assumes the current to be uniformly

distributed over the surface of a thin cylindrical conductor whose radius is R_w, i. e.

$$\xi = R_c + R_w \exp(iu) \qquad (69)$$

and $J|\xi_u| = I/2\pi N$. Here, R_c is the distance from the wire axis to the axis of symmetry of the array. The thin wire approximation is valid if $R_w \ll R_c/N$, $R_r - R_c$. Then, of course, $R_w \ll R_c$, hence the numerator of argument of logarithmic function in Eq. (67) is approximated by $R_r^{2N} - R_c^{2N}$, whereas the denominator becomes $NR_c^{N-1}R_w R_r^N$. Thus we obtain the well-known Russell's formula[23] for the inductance of a single wire array:

$$L = \frac{\mu_0 l}{2\pi}\left[\ln\frac{R_r}{R_c} + \frac{1}{N}\ln\frac{R_c}{NR_w} + \frac{1}{N}\ln\left\{1 - \left(\frac{R_c}{R_r}\right)^{2N}\right\}\right]. \qquad (70)$$

(It should be noted that a version of this formula presented in Ref. 24 contains a typo, reproduced later by some other authors: instead of the radius of the wire, the second term in square brackets contains the wire diameter.) The correction of order of $(R_c/R_r)^{2N}$ was taken into account in Ref. 18. In most cases, it is very small.

Now consider a nested wire array, a load configuration initially suggested in Ref. 8 and then used in Refs. 1, 16 and many other experiments. Here we consider two concentric rows each containing N wires located at the radii R_{c1} and R_{c2}, where subscripts 1 and 2 refer to the outer and inner arrays, respectively. Denote the complex coordinates of the first wires in each array by ξ_1 and ξ_2, respectively:

$$\xi_j = R_{cj} + R_{wj}\exp(iu), \quad j = 1,2. \qquad (71)$$

Vector potential of the global magnetic field in the case of nested wire array configuration is a sum of contributions from the two arrays:

$$A(z,t) = A_1(z,t) + A_2(z,t), \qquad (72)$$

where

93

$$A_j(z,t) = \frac{\mu_0}{2\pi} \int_0^{2\pi} J_j \mid \xi_{ju} \mid \ln \frac{\mid R_r^{2N} - (\bar{\xi}_j z)^N \mid}{R_r^N \mid z^N - \xi_j^{EN} \mid} du .$$
(73)

Since both arrays are connected to the same electrodes, the magnetic vector

potential has the same value for all the wires:

$$A(\xi_j, t) = \Lambda_j(t) = \Lambda(t), \quad j = 1,2.$$
(74)

This condition allows one to find the distribution of current I between the inner and the

outer components of the nested array, $I_1 + I_2 = I$. Applying the thin wire approximation

to both arrays (i. e. assuming $R_{wj} \ll R_{ck}$, $j,k = 1,2$ and $J_j \mid \xi_{ju} \mid = I_j / 2\pi N$), one can

present the system of equations (60) in a matrix form:

$$\hat{e}_j \phi = \hat{e}_j \int U dt = \hat{e}_j I \Lambda = \frac{\mu_0 I}{2\pi} \hat{L}_{jk} I_k, \quad j,k = 1,2,$$
(75)

where $\hat{e}_j = \begin{pmatrix} 1 \\ 1 \end{pmatrix}$ is the unit column and $\hat{L}_{jk}$ are the elements of the dimensionless

inductance matrix:

$$\hat{L}_{jj} = \ln \frac{R_r}{R_{cj}} + \frac{1}{N} \ln \left[\frac{R_{cj}}{NR_{wj}} \left(1 - \frac{R_{cj}^{2N}}{R_r^{2N}} \right) \right],$$

$$\hat{L}_{jk} = \frac{1}{N} \ln \frac{R_r^{2N} - R_{cj}^N R_{ck}^N}{R_r^N \mid R_{cj}^N - R_{ck}^N \mid}, \quad j \neq k.$$
(76)

Here, the diagonal elements of the matrix are self-inductances of the component arrays,

and the off-diagonal term is the mutual inductance (in this case of a 2×2 matrix, the

mutual inductance is $\hat{L}_{12} = \hat{L}_{21}$). The inductance matrix is symmetric and positive

definite,[22] thus the inverted matrix $\hat{L}_{jk}^{-1}$ always exists. Presenting the normalization

condition in a vector form

$$I = I_j \hat{e}_j = I_1 + I_2,$$
(77)

we obtain a general solution of Eqs. (75), (77)

$$I_k = \frac{2\pi\phi}{\mu_0 l} \hat{L}_{jk}^{-1} \hat{e}_j .$$ (78)

The total inductance is

$$L = \frac{\phi}{I} = \frac{\mu_0 l}{2\pi} \frac{1}{\hat{e}_k \hat{L}_{jk}^{-1} \hat{e}_j} ,$$ (79)

and combining this with (78), we find:

$$I_k = I \frac{\hat{L}_{jk}^{-1} \hat{e}_j}{\hat{e}_k \hat{L}_{jk}^{-1} \hat{e}_j} .$$ (80)

All the derivations for the nested arrays were performed in a general vector form, and therefore are valid for any amount of wires in arrays consistent with the N-th order rotational symmetry (for instance, N wires in the inner and $2N$ wire in the outer array).

For an important particular case when $(R_{c1}/R_r)^N$, $(R_{c2}/R_r)^N \ll 1$ we can further simplify (76) to give

$$\hat{L}_{11} = \ln \frac{R_r}{R_{c1}} + \frac{1}{N_1} \ln \frac{R_{c1}}{N_1 R_{w1}} , \quad \hat{L}_{22} = \ln \frac{R_r}{R_{c2}} + \frac{1}{N_2} \ln \frac{R_{c2}}{N_2 R_{w2}} ,$$
$$\hat{L}_{12} = \hat{L}_{21} = \ln \frac{R_r}{R_{c1}} .$$ (81)

In the thin wire approximation, (81) is valid under above assumptions for arbitrary numbers of wires N_1 and N_2 in the component arrays. The self-inductance for each of them is given by the Russell's formula. The mutual inductance in this approximation simply equals a self-inductance of a conducting shell whose radius equals the radius of the outer array. Physically, this is quite clear: the outer array generates the same magnetic flux in the contour formed by the inner array and the return current can as a conducting shell of the same radius R_{c1} would.

95

For a two-component nested wire array, the solutions (79)-(80) could be presented

in a scalar form:

$$L = \frac{\mu_0 l}{2\pi} \frac{\hat{L}_{11}\hat{L}_{22} - \hat{L}_{12}^2}{\hat{L}_{11} + \hat{L}_{22} - 2\hat{L}_{12}}$$

$$I_1 = I\frac{\hat{L}_{22} - \hat{L}_{12}}{\hat{L}_{11} + \hat{L}_{22} - 2\hat{L}_{12}}, \quad I_2 = I\frac{\hat{L}_{11} - \hat{L}_{12}}{\hat{L}_{11} + \hat{L}_{22} - 2\hat{L}_{12}}.$$

(82)

Using the approximation (81) for the self- and mutual inductance, one determines the

fraction of the total current flowing in the inner array to be

$$\frac{I_2}{I} = \frac{\frac{1}{N_1}\ln\frac{R_{c1}}{N_1 R_{w1}}}{\ln\frac{R_{c1}}{R_{c2}} + \frac{1}{N_1}\ln\frac{R_{c1}}{N_1 R_{w1}} + \frac{1}{N_2}\ln\frac{R_{c2}}{N_2 R_{w2}}}.$$

(83)

According to (81), the numerator of the right-hand side of (83) is the excess of the self-

inductance of the outer array over the self-inductance of a perfectly conducting shell of

the same radius R_{c1}. A perfectly conducting shell would provide a perfect screening,

$I_2 = 0$. Equation (83) also implies that a perfect screening – no current in the inner array

– is achieved when the argument of the logarithm is unity, i. e. the gap-to-diameter ratio

is

$$\frac{r_g}{D_{w1}} = \pi,$$

(84)

where $r_g = 2\pi R_1 / N_1$ is the gap between the centers of the neighboring wires, $D_{w1} = 2R_{w1}$

is the outer wire diameter. In fact, the current in the inner array does not vanish when

(84) is satisfied, see below. Rather, (84) indicates the gap-to-diameter ratio below which

the thin wire approximation is no longer valid. For typical experimental conditions of,

say, Ref. 1 ($N_1 = 240, N_2 = 120, R_{c1} = 2$ cm, $R_{c2} = 1$ cm, R_{w1} and R_{w2} varied between 20

and 50 μm), the current fraction in the inner array varies between 0.8% and 0.3%. Our explicit expressions for self- and mutual inductance of single and nested wire arrays can help in obtaining a simple zero-dimensional (0-D) description of their implosion dynamics, see Appendix C.

Figure 2 compares the current fraction in the inner array and the total induction found using the thin wire approximation and with the aid of Eq. (74) solved exatcly, as described in the next Section. Here $R_r / R_{c1} = 2$, $R_{c1} / R_{c2} = 2$, $R_{c1} / R_{w1} = R_{c2} / R_{w2} = 64$, and the number of wires in both arrays, $N_1 = N_2 = N$ is varied. The condition (84) corresponds to $N = 64$. We see that (83) is a good approximation for I_2 / I up to $N \sim 50$. For larger number of wires, this approximation breaks down for the obvious reason: distribution of the current density on the surface of a conducting plasma column cannot be assumed uniform when the distance between the neighboring columns is comparable to the column diameter. Note that the expression for the total inductance L remains a good approximation even when the thin wire approximation becomes formally invalid.

D. Arbitrary shape of the boundary contour: Distribution of current in discrete filaments

The technique described in Section III.C allows us to develop a general method of calculating the current density distribution on the surface of a conductor with arbitrary shape of its cross section. For this, we approximate the conducting surface with a large number of thin current filaments and treat these filaments as separate wires connected in parallel to the same electrodes. Therefore, all these filaments are at the same vector potential. Assuming the radii of these filaments much less than the cross-sectional dimension of the plasma column, R_w, one can use the symmetrical, positive-definite

inductance matrix derived above in the thin wire approximation to determine the distribution of the current between the filaments.

Here we describe this calculation for a single wire array (it is readily generalized for a nested wire array). The interval $[0, 2\pi]$ for the variable u is split into a large number $K \gg 1$ of sub-intervals $[u_k - (1/2)\Delta u, u_k + (1/2)\Delta u]$, where $\Delta u = 2\pi / K$. It is assumed that the complex coordinate of the middle point of the k-th subinterval $\xi_k(t) = \xi(u_k, t)$ defines the position of the k-th filament, which carries a current $I_k = J(u_k, t)|\xi_{ku}|\Delta u$, and its effective radius is $q_k = (1/2)|\xi_{ku}|\Delta u \ll R_w$. Thus the solution (75) obtained in the thin wire approximation, remains valid:

$$\hat{e}_j \phi = \hat{e}_j l\Lambda = \frac{\mu_0 l}{2\pi} \hat{L}_{jk} I_k, \quad j,k = 1,...,K, \tag{85}$$

where $\hat{e}_j$ is now a unit column containing K rows. The inductance matrix is similar to (76), but its elements now refer to the current filaments on the surface of a single plasma column rather than to the inner and outer components of a nested wire array:

$$\hat{L}_{jj} = N \ln \frac{R_r}{|\xi_j|} + \ln \left[\frac{|\xi_j|}{N q_j} \left(1 - \frac{|\xi_j|^{2N}}{R_r^{2N}} \right) \right],$$
$$\hat{L}_{jk} = \ln \frac{|R_r^{2N} - (\overline{\xi}_k \xi_j)^N|}{R_r^N |\xi_j^N - \xi_k^N|}, \quad j \neq k. \tag{86}$$

The normalization condition (77) becomes

$$N I_k \hat{e}_k = 1. \tag{87}$$

The total inductance of the N-wire array is given by an equation similar to (79):

$$L = \frac{\mu_0 l}{2\pi N} \frac{1}{\hat{e}_k \hat{L}_{jk}^{-1} \hat{e}_j}. \tag{88}$$

and the current in each filament is given by a formula similar to (80):

$$I_k = \frac{I}{N} \frac{\hat{L}_{jk}^{-1}\hat{e}_j}{\hat{e}_k\hat{L}_{jk}^{-1}\hat{e}_j} . \tag{89}$$

Using the formulae (86)-(88), (89), the distribution of the current density on the surface of a conductor with arbitrary shape of its cross section can be calculated numerically. In the plasma dynamics problem described in Section II, the cross section is represented by a given contour $\xi(u,t)$ on a complex plane. We can thus find the fluid pressure in Eq. (52) $p = p_k = p(u_k,t)$ for the given complex coordinate $\xi_k(t) = \xi(u_k,t)$ of a boundary contour:

$$p(u_k,t) = \frac{\mu_0}{2} J^2(u_k,t) = \frac{\mu_0}{2} \frac{I_k^2}{(\Delta u)^2} \frac{1}{|\xi_u(u_k,t)|^2} . \tag{90}$$

This closes the MHD model presented in this article.

IV. Dynamics of a single wire array implosion

We apply dicretization to both arguments u and t of the contour functions $\xi_u(u,t)$ and $\Psi_u(u,t)$. Numerical integration of Eqs. (41) and (47) is performed using a space-centered explicit predictor-corrector Lax-Wendroff scheme of second order. The integral operator $\hat{H}$ is calculated using the algorithm of fast Fourier transform (see Appendix D for details).

The wire array is characterized by its effective radius $R_c(t)$ [associated with the position of the point $z_c(t)$ introduced by Eq. (38)], the average radius $R_w(t)$ of the conducting contour $\xi(u,t)$ representing the cross-section of a plasma column, the number N of wires in the array, and the radius R_r of the return current can. The initial shape of the

99

domain $R(t=0)$ is a circle with the radius $R_w(0)$, whose center is on the real axis at

$x = R_c(0)$. Our model equations could be coupled to an arbitrary circuit equation, but

here we assume the current driver to be sufficiently stiff, so that the current waveform is

independent from the implosion dynamics and could be presented as

$$I(t) = I_{max} \sin^2\left(\frac{\pi t}{2t_{max}}\right).$$

(91)

This approximation is good for the experiments on the MAGPIE facility in the Imperial

College;[14-16] for MAGPIE, I_{max} varies between 1 and 1.4 MA, and t_{max} is about 240 ns. We

choose the initial parameters close to (but not exactly the same as) those of the MAGPIE

experiments. The initial radius of the wire array is taken $R_c(0) = 8$ mm, the radius of the

plasma corona after the explosion of a 15 μm Al wire $R_w(0) = 125$ μm, t_{max} is taken

between 250 and 300 ns, the number of wires in the array is varied from 8 to 64. The

radius of the cylindrical return current can, $R_r = 10$ mm, is intentionally taken much less

than that of the return current structure of MAGPIE (4 to 8 posts at about 75 mm from the

axis). The corresponding ratio that we have chosen, $R_r / R_c(0) = 1.25$, is more typical for

"Z" and other multi-MA generators, which are softer than MAGPIE and thereby require

low-inductance loads. Proximity of the return current structure to the imploded wire array

can make the non-uniformity of the return current an issue, which we are going to address

below.

The main parameter determining the configuration of magnetic field in the wire

array is the gap-to-diameter ratio $\pi R_c(0) / N R_w(0)$, cf. Eq. (84). If $N = 8$ this parameter is

large enough, about 25. In this case, as shown in Fig. 3, a substantial part of the magnetic

flux penetrates the inter-wire gaps towards the axis of the array. Figure 4 shows that the current density tends to be concentrated on the outer part of the plasma column surfaces (peaking at $u = 0$), although its distribution is close to uniform: $J(\pi)/J(0) \approx 80\%$.

In the other limit $N = 64$ (Fig. 5) the neighboring conducting contours are close, $\pi R_c(0)/NR_w(0) = \pi$, and the magnetic field is effectively screened from penetration through the gaps between the plasma columns. In this case most of the current flows through the outer area of the conducting surface (Fig. 6): $J(\pi)/J(0) = 12\%$, and, consequently, $p(\pi)/p(0) = 1.4\%$.

Figure 7 shows that the distribution of the current density $J_r(\varphi)$ on the return current can surface is not uniform due to proximity of the plasma columns to the can wall. The function $J_r(\varphi)$ has N maximums at $\varphi = 2\pi(n-1)/N$, $n = 1,...,N$, just opposite to the plasma columns. If the return current radius is increased to 20 mm, then the distribution of the return current becomes almost uniform, whereas the distribution of current density on the plasma surface would remain virtually unchanged.

The periodic pressure function $p(u,t)$ shown in Figs. 4 and 6 is expanded into the Fourier series:

$$p(u,t) = p_0(t) + p_1(t)\cos u + p_2(t)\cos 2u + ... \tag{92}$$

The first term in the expansion (92), $p_0(t)$ describes a uniform pressure distribution. This corresponds to the contribution to the pressure provided by the "private" magnetic filed of the individual wire, which would result in its pinching if it were compressible. Obviously, this component does not change the shape of the boundary contour and causes no acceleration of the plasma column.

The second term, $p_1(t)\cos u$, is due to the force that is responsible for the implosion of the wire array. This force is caused by the interaction of the surface current with the global magnetic field and accelerates each wire towards the axis of the array [at all time, $p_1(t) > 0$] without affecting its cross-sectional shape.

The third component, $p_2(t)\cos 2u$, approximates the interaction between the surface current in the neighboring plasma columns by a local tidal force. This force deforms the boundary contour $\xi(u,t)$, squeezing it along the real x-axis and expanding it along the imaginary y-axis, without accelerating the plasma column as a whole. The tidal force causes the plasma columns to merge, to form a uniform shell during the implosion of the array.

Thus, dynamics of the plasma columns is defined by a competition between the implosion and tidal forces. The relative role of the tidal force could be estimate by the variable $p_{21}(t) = p_2(t)/p_1(t)$. This parameter is mostly affected by the gap-to-diameter ratio $\pi R_c(t)/NR_w(t)$ during the implosion.

We simulated the implosion of an 8-wire array, taking $I_{max} = 1\,\mathrm{MA}$ and $t_{max} = 310$ ns in Eq. (91). At the initial moment $p_{21}(0) = 0.04$, and the implosion force dominates over the tidal force responsible for the annular shell formation. At the early stage of implosion, the plasma columns retain their initial circular shapes as they accelerate towards the axis. The function $R_r(t)$ shown in Fig. 8 reproduces the well-known 0-D solution [cf. Appendix C, Eq. (C2)] for the implosion of a thin conducting shell driven by a current (91).

At the later stage of the implosion, as the gap-to-diameter ratio $\pi R_c(t)/NR_w(t)$ decreases, the tidal force gradually becomes dominant. Figure 9 shows that the deformation of the boundary contours becomes noticeable at $R_c \approx 1.2$ mm. At this point the gap-to-diameter ratio is about 2, and the magnetic field configuration is similar to one shown in Fig. 5. However, the wire plasmas by this moment already have a high inward radial velocity, and the shell formation is only completed when $R_c \approx 0.5$ mm.

In the case of a 64-wire array, the tidal force plays an important role from the very beginning: $p_{21}(0) = 0.36$. Figure 10 demonstrates that the column cross-sections are already substantially deformed at the moment $t = t_{max}/4$, when the columns have barely moved from their initial positions toward the axis of the array. The distributions of current density and pressure at this moment shown in Fig. 11 are very close to the step functions characteristic of an annular shell implosion.

Our analysis demonstrated a competition between the imploding force, making the array implode as a set of individual wires, and the tidal force making the wires merge into an annular shell. Formation of precursor plasma streams flowing to the axis ahead of the main plasma mass is not described by the present model. The reason for this is seen from Eq. (50): only the normal component of the $\mathbf{J} \times \mathbf{B}$ force acts on the boundary surface of the plasma column, pushing the plasma inward. It is well known, however, that the exploded wire plasma is highly non-homogeneous. As predicted in Ref. 25 and confirmed in later studies (see Ref. 10 and references therein), electrical explosion of a solid wire produces a plasma column, which contains high-density core and low-density corona regions, with the skin depth comparable to the thickness of the corona. Assuming the

corona thickness at early time much less than the core diameter, we can roughly estimate the longitudinal component of the $\mathbf{J} \times \mathbf{B}$ acting on some parts of the coronal plasma by

$$e_{\parallel} \cdot [\mathbf{J} \times \mathbf{B}] \propto J(u,t) \frac{\partial}{\partial u} B_{\parallel}(u,t) \propto \frac{\partial}{\partial u} p(u,t) \equiv p_u. \tag{93}$$

Qualitative profiles of the derivative p_u are shown in Figs. 4 and 6. This function is zero at $u = 0$ and $u = \pi$ and has two maximums near $u = \pi/2$ and $u = 3\pi/2$. At both maximums of p_u the longitudinal component of the $\mathbf{J} \times \mathbf{B}$ force is directed to the axis of the wire array. Since the density of coronal plasma is much lower than the core density, and it is free to move away from the core, such a force configuration would produce precursor jets streaming to the pinch axis.[10, 16] However, neither the process of generation nor the dynamics of these jets could be treated in the incompressible fluid approximation.

V. Conclusion

The implosion dynamics of wire arrays on the (r, θ) plane has been studied with the aid of a perfectly conducting, incompressible fluid model. The implosion dynamics is driven by the competition between the implosion pressure, which makes the array converge to the axis as a set of individual plasma columns, and the tidal pressure that makes the wires merge, forming an annular conducting shell. The relative roles of the implosion and tidal pressure are determined by the gap-to-diameter ratio $\pi R_c(t) / N R_w(t)$. If this ratio is large at early time (this is when the thin wire approximation works, and the Russell's formula is valid), then the array implodes as a set of individual plasma columns. In the opposite limit, when this ratio is about π or less at early time, the thin-wire approximation is not applicable – the distribution of current over the plasma surface is

very non-uniform, peaked at the outer side. Then the tidal forces prevail in the early-time dynamics, and the plasma columns tend to form a shell-like configuration before they start converging to the axis of the array.

The approximation of perfectly conducting incompressible fluid does not describe the precursor plasma jets that stream to the axis ahead of the heavier wire cores. These are driven by the longitudinal component of the $\mathbf{J} \times \mathbf{B}$ force, which we were able to estimate. This force peaks at the sides of the plasma columns and is directed to the axis of the array. To describe the jet formation on the (r, θ) plane, one therefore needs adequate models of the plasma conductivity and its equation of state.

Our model, being admittedly simplified, has the advantages of physical transparence and numerical efficiency. It could be used to benchmark the MHD hydrocodes on the (r, θ) plane, where no exact solutions were available for this purpose until now. This model could also be applied to some other problems of relevance for the inertial confinement fusion. For instance, it could be used for modeling the non-linear stages of Rayleigh-Taylor and Richtmyer-Meshkov instabilities, where it might have some advantages over the existing analytical and semi-analytical approaches (see Refs. 26 and references therein).

Acknowledgements

Appendix A. A particular solution of the equation of motion for the contour: uniform velocity

Complex velocity potential $X(z,t) = zv_0$, where v_0 is a real constant, corresponds to a uniform distribution of the fluid velocity: $v(z,t) = v_0$. In this case the boundary value Ψ of the velocity potential $\Phi(z,t) = v_0 \operatorname{Re}(z)$ is

$$\Psi(u,t) = v_0 \operatorname{Re}[\xi(u,t)], \quad \Psi_u = v_0 \operatorname{Re}[\xi_u]. \tag{A1}$$

Substituting the above distribution of Ψ_u into Eq. (32), we obtain:

$$\frac{\hat{H}\Psi_u}{|\xi_u|^2} = -v_0 \operatorname{Im}\left(\frac{1}{\xi_u}\right), \quad \hat{H}\frac{\hat{H}\Psi_u}{|\xi_u|^2} = v_0 \operatorname{Re}\left(\frac{1}{\xi_u}\right) + \frac{2v_0}{f(t)}\sin u,$$

$$V(u,t) = \xi_t = v_0 + \frac{2\xi_u}{f(t)}[v_0 - V_c(t)]\sin u. \tag{A2}$$

If the function $V_c(t)$ satisfies (39),

$$\varsigma_t(0,t) = \varsigma_t(\pi,t) = v_0, \quad V_c(t) = v_0. \tag{A3}$$

Thus $V(u,t) = v_0$ for any shape of the boundary contour $\xi(u,t)$.

Appendix B. Integral of motion

Let us calculate the following integral

$$\begin{aligned}
P &= \frac{d}{dt}\oint_{z=\xi}\Phi dz + \oint_{z=\xi}\frac{P}{\rho}dz = \frac{d}{dt}\int_0^{2\pi}\Psi\xi_u du + \int_0^{2\pi}\frac{p}{\rho}\xi_u du \\
&= \int_0^{2\pi}\left[\xi_u\left(\frac{\partial\Psi}{\partial t} + \frac{p}{\rho}\right) - \Psi_u\xi_t\right]du.
\end{aligned} \tag{B1}$$

Substituting Eqs. (32) and (46) into (B1), we obtain that

$$P = \int_0^{2\pi}\left[a(t) - \frac{\left(\Psi_u - i\hat{H}\Psi_u\right)^2}{2|\xi_u|^2}\right]\xi_u du. \tag{B2}$$

Obviously,

$$a(t) \int_0^{2\pi} \xi_u du = a(t) \oint_{z=\xi} dz \equiv 0. \tag{B3}$$

and

$$\xi_u \frac{\left(\Psi_u - i\hat{H}\Psi_u\right)^2}{|\xi_u|^2} = \left[\frac{\partial \overline{X}(\overline{z})}{\partial \overline{z}}\right]_{\overline{z}=\overline{\xi}}^2 = \left[v(\overline{z},t)\right]_{\overline{z}=\overline{\xi}}^2. \tag{B4}$$

If we change the argument of the anti-analytic function $v(z,t)$ to its complex conjugate, this function becomes an analytic function $v(\overline{z},t)$ which satisfies the Cauchy-Riemann conditions. Thus, according to the Cauchy theorem,

$$\mathsf{P} = -\frac{1}{2} \oint_{\overline{z}=\overline{\xi}} v^2(\overline{z},t)d\overline{z} = 0. \tag{B5}$$

Therefore Eq. (48) holds during the evolution of the system described by Eqs. (41) and (47).

Appendix C. Dynamics of single and nested wire arrays in a thin wire approximation.

Our expressions for self- and mutual inductance lead to a simple 0-D description of the implosion dynamics in a thin wire approximation. Equations of motion are derived from a Lagrangian, which for a single wire array has the form

$$\mathsf{L} = \mathsf{K} - \mathsf{U} = \frac{m}{2}\dot{R}_c^2 + \frac{L(R_c)}{2}I^2. \tag{C1}$$

Here, m is the mass of the array, K is its kinetic energy, U is the potential or free energy given by the formula $\mathsf{U} = -LI^2/2$ from Ref. 22. Substituting the Russell formula (70) into the Lagrange equation $(d/dt)(\partial \mathsf{L}/\partial \dot{R}_c) = \partial \mathsf{L}/\partial R_c$, we obtain the well-known 0-D equation of motion

$$m\ddot{R}_c = \frac{I^2}{2}\frac{\partial L}{\partial R_c} = -\frac{\mu_0 l(N-1)}{4\pi N R_c}I^2 \tag{C2}$$

(the current I is treated here as an independent variable). Equation (C2) says that each wire is pushed to the axis by the Ampère force due to the interaction of its current, I/N, with the azimuthal magnetic field produced by the remaining $N-1$ wires. Note that the radial acceleration of the wires is given by (C2) even if the wires are not distributed equidistantly on a circle whose radius is R_c.

For a nested wire array, the corresponding Lagrangian is

$$\begin{aligned} L &= \frac{m_1}{2}\dot{R}_{c1}^2 + \frac{m_2}{2}\dot{R}_{c2}^2 + \frac{L(R_{c1}, R_{c2})}{2}I^2 \\ &= \frac{m_1}{2}\dot{R}_{c1}^2 + \frac{m_2}{2}\dot{R}_{c2}^2 + \frac{\mu_0 l}{4\pi}\left[\hat{L}_{11}(R_{c1})I_1^2 + 2\hat{L}_{12}(R_{c1}, R_{c2})I_1 I_2 + \hat{L}_{22}(R_{c2})I_2^2\right], \end{aligned} \tag{C3}$$

where m_1 and m_2 are the masses of the two components of the wire array, and its inductance is given by Eqs. (81), (82). In the "transparent inner" mode of interaction,[8, 9, 16] the imploding outer array 1 can penetrate inside the inner array 2, and their respective roles will then be reversed. To take this into account, we generalize the expression (81) for the mutual inductance:

$$\hat{L}_{12}(R_{c1}, R_{c2}) = \hat{L}_{21}(R_{c1}, R_{c2}) = \ln\frac{R_r}{\max(R_{c1}, R_{c2})}. \tag{C4}$$

The equations of motion derived from (C3) with the aid of (81), (82), (C4) are

108

$$m_1 \ddot{R}_{c1} = I^2 \frac{\partial}{\partial R_{c1}} L = \frac{\mu_0 l}{4\pi} \left(I_1^2 \frac{\partial \hat{L}_{11}}{\partial R_{c1}} + 2I_1 I_2 \frac{\partial \hat{L}_{12}}{\partial R_{c1}} \right)$$

$$= -\frac{\mu_0 l I_1}{4\pi R_{c1}} \left[\frac{(N_1 - 1)I_1}{N_1} + 2I_2 \theta(R_1 - R_2) \right],$$

$$m_2 \ddot{R}_{c2} = I^2 \frac{\partial}{\partial R_{c2}} L = \frac{\mu_0 l}{4\pi} \left(I_2^2 \frac{\partial \hat{L}_{22}}{\partial R_{c2}} + 2I_1 I_2 \frac{\partial \hat{L}_{12}}{\partial R_{c2}} \right)$$

$$= -\frac{\mu_0 l I_2}{4\pi R_{c2}} \left[\frac{(N_2 - 1)I_2}{N_2} + 2I_1 \theta(R_2 - R_1) \right],$$

$$(C5)$$

where $\theta(z)$ is the Heaviside step function. Equations (C5) demonstrate that the inner array is imploded by its own current, whereas the outer array is additionally pushed to the axis by the interaction of its current with the azimuthal magnetic field generated by the current in the inner array.

Appendix D. Fourier representation of the operator $\hat{H}$.

The function $X(z_0, t)$, which is analytic in the unit circle, is thereby equal to the sum of its Taylor series

$$X(z_0, t) = \sum_{k=0}^{\infty} c_k(t) z_0^k, \qquad (D1)$$

where $|z_0| \le 1$ and the coefficients c_k are given by

$$c_k(t) = \frac{1}{2\pi i} \oint \frac{X(z_0, t)}{z_0^{k+1}} dz_0, \qquad (D2)$$

where the integration contour is within the unit circle. At the boundary of the unit circle, Eqs. (14), (15), (D1), (D2) yield

$$X(z_0, t)\big|_{z_0 = \exp(iu)} = \Psi(u, t) + i\Theta(\xi(u, t), t) = \sum_{k=0}^{\infty} c_k(t) e^{iku},$$

$$c_k(t) = \frac{1}{2\pi} \int_0^{2\pi} \left[\Psi(w, t) + i\Theta(\xi(w, t), t) \right] e^{-ikw} dw.$$

$$(D3)$$

Separating the real and imaginary parts of Eq. (D3) and taking into account the Fourier expansion

$$\Psi(u,t) = \sum_{k=0}^{\infty} [a_k(t)\cos ku + b_k(t)\sin ku],$$ (D4)

where

$$a_k(t) = \frac{1}{\pi} \int_0^{2\pi} \Psi(w,t)\cos(kw)dw, \quad b_k(t) = \frac{1}{\pi} \int_0^{2\pi} \Psi(w,t)\sin(kw)dw,$$ (D5)

one can obtain that the following definition of the integral operator $\hat{H}$

$$\hat{H}\Psi(u,t) = \sum_{k=0}^{\infty} [a_k(t)\sin ku - b_k(t)\cos ku] = \frac{1}{\pi} \int_0^{2\pi} \Psi(w,t) \left[\sum_{k=1}^{\infty} \sin k(u-w) \right] dw$$ (D6)

is equivalent to its original definition (6). Indeed,

$$\hat{H}\Psi(u,t) = \frac{1}{\pi} \int_0^{2\pi} \Psi(w,t) \operatorname{Im} \left[\sum_{k=1}^{\infty} e^{ik(u-w)} \right] dw$$

$$= \frac{1}{\pi} \int_0^{2\pi} \Psi(w,t) \operatorname{Im} \left[\frac{e^{i(u-w)}}{1-e^{i(u-w)}} \right] dw = \frac{1}{2\pi} \int_0^{2\pi} \Psi(w,t)\cot\left(\frac{u-w}{2}\right) dw.$$ (D7)

Comparing Eqs. (D4) and (D6), we see that the operator $\hat{H}$ applied to a Fourier-series expansion of a real-valued function, changes the basis of the Fourier representation as follows: $\hat{H}(\cos ku, \sin ku) = (\sin ku, -\cos ku)$.

References

[1] C. Deeney, M. R. Douglas, R. B. Spielman, T. J. Nash, D. L. Peterson, P. L'Eplattenier, G. A. Chandler, J. F. Seaman, and K. W. Struve, Phys. Rev. Lett. **81**, 4883 (1998).

[2] C. Deeney, C. A. Coverdale, M. R. Douglas, T. J. Nash, R. B. Spielman, K. W. Struve, K. G. Whitney, J. W. Thornhill, J. P. Apruzese, R. W. Clark, J. Davis, F. N. Beg and J. Ruiz-Camacho, Phys. Plasmas **61**, 2081 (1999).

[3] H. Sze, J. Banister, P. L. Coleman, B. H. Failor, A. Fisher, J. S. Levine, Y. Song, E. M. Waisman, J. P. Apruzese, R. W. Clark, J. Davis, D. Mosher, J. W. Thornhill, A. L. Velikovich, B. V. Weber, C. A. Coverdale, C. Deeney, T. Gilliland, J. McGurn, R. Spielman, K. Struve, W. Stygar, and D. Bell, Phys. Plasmas **8**, 3135 (2001).

[4] Y. Song, P. Coleman, B. H. Failor, A. Fisher, R. Ingermanson, J. S. Levine, H. Sze, E. Waisman, R. J. Commisso, T. Cochran, J. Davis, B. Moosman, A. L. Velikovich, B. V. Weber, D. Bell and R. Schneider, Rev. Sci. Instrum. **71**, 3080 (2000).

[5] F. L. Cochran, J. Davis, and A. L. Velikovich, Phys. Plasmas **2**, 2765 (1995).

[6] A. L. Velikovich, F. L. Cochran, and J. Davis, Phys. Rev. Lett. **77**, 853 (1996); A. L. Velikovich, F. L. Cochran, J. Davis, and Y. K. Chong, Phys. Plasmas **5**, 3377-3388 (1998).

[7] T. W. L. Sanford, R. C. Mock, R. B. Spielman, D. L. Peterson, D. Mosher, and N. F. Roderick, Phys. Plasmas **5**, 3737 (1998).

[8] J. Davis, N. A. Gondarenko, and A. L. Velikovich, Appl. Phys. Lett. **70**, 170 (1997).

[9] R. E. Terry, J. Davis, C. Deeney, and A. L. Velikovich, Phys. Rev. Lett. **83**, 4305 (1999).

[10] J. P. Chittenden, S. V. Lebedev, A. R. Bell, R. Aliaga-Rossel, S. N. Bland, and M. G. Haines, Phys. Rev. Lett. **83**, 100 (1999). J. P. Chittenden, S. V. Lebedev, S. N. Bland, F. N. Beg, and M. G. Haines, Phys. Plasmas **8**, 2305 (2001).

[11] D. L. Peterson, R. L. Bowers, K. D. McLenithan, C. Deeney, G. A. Chandler, R. B. Spielman, M. K. Matzen, and N. F. Roderick, Phys. Plasmas **5**, 3302 (1998).

[12] D. L. Peterson, R. L. Bowers, W. Matuska, K. D. McLenithan, G. A. Chandler, C. Deeney, M. S. Derzon, M. Douglas, M. K. Matzen, T. J. Nash, R. B. Spielman, K. W. Struve, W. A. Stygar, and N. F. Roderick, Phys. Plasmas **6**, 2178 (1999).

[13] L. I. Rudakov, A. L. Velikovich, J. Davis, J. W. Thornhill, J. L. Giuliani, Jr., and C. Deeney, Phys. Rev. Lett. **84**(15), 3326-3329 (2000); A. L. Velikovich, L. I. Rudakov, J. Davis, J. W. Thornhill, J. L. Giuliani, Jr., and C. Deeney, Phys. Plasmas **7**, 3265 (2000).

[14] S. V. Lebedev, F. N. Beg, S. N. Bland, J. P. Chittenden, A. F. Dangor, M. G. Haines, K. H. Kwek, S. A. Pikuz, and T. A. Shelkovenko, Phys. Plasmas **8**, 3734 (2001)

[15] S. V. Lebedev, F. N. Beg, S. N. Bland, J. P. Chittenden, A. F. Dangor, M. G. Haines, K. H. Kwek, S. A. Pikuz, and T. A. Shelkovenko, Phys. Rev. Lett. **85**, 98 (2000).

[16] S. V. Lebedev, R. Aliaga-Rossel, S. N. Bland, J. P. Chittenden, A. E. Dangor, M. G. Haines, and M. Zakaullah, Phys. Rev. Lett. **84**, 1708 (2000); J. P. Chittenden, S. V. Lebedev, S. N. Bland, A. Ciardi, and M. G. Haines, Phys. Plasmas **8**, 675 (2001).

[17] R. B. Baksht, A. Y. Labetsky, S. V. Loginov, V. I. Oreshkin, A. V. Fedyunin, and A. V. Shishlov, Plasma Phys. Rept. **23**, 119 (1995); R. B. Baksht, A. Y. Labetsky, A. G. Rousskikh, A. V. Fedyunin, A. V. Shishlov, V. A. Kokshenev, and N. E. Kurmaev, Plasma Phys. Rept. **27**, 557 (2001).

[18] E. M. Waisman, J. Appl. Phys. **50**, 23 (1979).

[19] A. I. Dyachenko, V. E. Zakharov, and E. A. Kuznetsov, Plasma Phys. Rep. **22**, 829 (1996).

[20] M. A. Lavrentyev and B. V. Shabat, *Problems of Hydrodynamics and Their Mathematical Models*, 2nd edition (In Russian, Moscow, Nauka, 1977); Z. Nehari, *Conformal Mapping* (McGraw-Hill, New York, 1952).

[21] I. E. Parshukov, *Development and Applications of the Vortex Method for Studying the Nonlinear Evolution of an Unstable Contact Boundary Between Incompressible Fluids*, Ph. D. thesis (in Russian; Chelyabinsk State University, Chelyabinsk, Russia, 1997).

[22] L. D. Landau and E. M. Lifshitz, *Electrodynamics of Continuous Media* (Pergamon, New York, 1984).

[23] A. Russell, Journ. Inst. Electr. Eng. **62**, 1 (1923); **69**, 270 (1931); F. W. Grover, *Inductance Calculations / Working Formulas and Tables* (Van Nostrand Publishing Co., New York, 1946), p. 43.

[24] J. Katzenstein, J. Appl. Phys. **52**, 676 (1981).

[25] N. A. Bobrova, T. L. Razinkova and P. V. Sasorov, Sov. J. Plasma Phys. **14**, 617 (1988); **18**, 269 (1992); in *Dense Z-Pinches*, 3rd International Conference, AIP Conf. Proc. 299, London, United Kingdon, 19-23 April 1993, edited by M. Haines and A. Knight (American Institute of Physics, New York, 1994), p. 10.

[26] R. Menikoff and C. Zemach, J. Comp. Phys. **51**, 28 (1983); G. Hazak, Phys. Rev. Lett. **76**, 4167 (1996); A. L. Velikovich and G. Dimonte, Phys. Rev. Lett. **76**, 3112 (1996); N. J. Zabusky, Ann. Rev. Fluid Mech. **31**, 495 (1999)

Fig. 1. The reference frame tied to the contour $\xi(u,t)$.

Fig. 2. Fraction of current in the inner array I_2/I and normalized inductance of the nested array L/L_0 ($L_0 = \mu_0 l/2\pi$) vs. number of wires in both arrays, N, for $R_r/R_{c1} = 2$, $R_{c1}/R_{c2} = 2$, $R_{c1}/R_{w1} = R_{c2}/R_{w2} = 64$. Lines represent exact values found numerically, symbols – the thin wire approximation.

Fig. 3. Magnetic force lines for a 8-wire array with $R_w(0) = 125$ μm, $R_c(0) = 8$ mm, $R_r = 10$ mm, at early time $t \rightarrow +0$, before the motion and deformation of the array started. Bold lines show the conducting contours ξ_1, ξ_2, ξ_3 and the return current can.

Fig. 4. Relative variation of the current density $J(u,t)$ and fluid pressure $p(u,t)$ normalized to $J_0 = I(t)/2\pi N R_w$ and $p_0 = \mu_0 J_0^2/2$, respectively, vs. the contour parameter u, for the conditions of Fig. 3. The derivative $p_u = \partial p/\partial u$ is also shown in arbitrary units with its zero level marked by the dash-and-dot line. The positions defined as $u = 0$ and $u = \pi$ correspond to points of the contour, which are farthest from and closest to the axis, respectively (cf. Fig. 1).

Fig. 5. Same as in Fig. 3 for a 64-wire array with $R_w(0) = 125$ μm, $R_c(0) = 8$ mm, $R_r = 10$ mm.

Fig. 6. Same as in Fig. 4, for the conditions of Fig. 5.

Fig. 7. Relative variation of the current density $J(u,t)$, normalized as in Fig. 4, and of the return current density $J_r(\varphi,t)$ (normalized with respect to $\langle J_r \rangle = I(t)/2\pi R_r$), for the conditions of Fig. 3, and the same for the radius of return current can $R_r = 20$ mm.

Fig. 8. Implosion dynamics of a wire array whose initial configuration is shown in Fig. 3: the average radius of the array $R_c(t)$, the implosion velocity $V_c(t) = |\dot{R}_c(t)|$ and the current waveform $I(t)$.

Fig. 9. Cross-sections of the plasma columns ξ_1, ξ_2, and ξ_3 at the instants when $R_c(t) = 1.2$ mm (dashed lines) and 0.5 mm (solid lines) for the implosion whose time history is shown on Fig. 8.

Fig. 10. Early-time implosion dynamics of a wire array whose initial configuration is shown in Fig. 5. Solid lines show the cross-sections of the plasma columns ξ_1, ξ_2, and ξ_3 at $t = t_{max}/4$; dashed lines refer to their initial shapes and positions at $t = 0$.

Fig. 11. Relative variation of the current density $J(u,t)$ and fluid pressure $p(u,t)$ normalized as in Fig. 4, for the contours shown by the solid lines in Fig. 10.

IV. Increasing K-shell Yields by Using a Low-Z Gas in the Outer shell of a Double-Puff Nozzle

A. Introduction

In this section we show some encouraging model results attained by replacing argon with a low-Z gas in the outer shell of a 4-3-2-1 nozzle. These calculations provide theoretical evidence that attaining high argon K-shell yields from more massive loads than presently envisioned are possible if a low-Z gas, rather than argon, is employed in the outer shell. This means that for a given load configuration, e.g. the 4-3-2-1 nozzle, we could use more of the Decade Quad (DQ) current and energy for producing K-shell yield. Note, the idea of replacing argon with a lower-Z gas in the outer shell is an idea that has been discussed by the Plasma Radiation Source (PRS) community for some time. Such a study was recommended in the summary of the Second Meeting of the PRS Working Group, which took place in October 2002. The work presented in this section was performed in response to that recommendation.

The one-dimensional (1D) models are not capable of modeling all the effects present in multi-dimensional Z-pinch plasmas. However, by a judicious choice of transport coefficients (viscosity, heat conductivity, and ion-electron heat exchange), a reasonable match between calculated and measured K-shell yields can be made over a broad range of experimental conditions for a given nozzle configuration. We cannot fully quantify the extent that our phenomenological model captures the physics of actual multi-dimensional plasma implosions, so to some extent any insights gained by this work are inherently speculative. However, for now (until Mach2 is a fully operational code containing adequate radiation physics), this is likely the best modeling that can be accomplished that includes the essential radiation physics of the implosion. Specifically, having benchmarked the code to experimental argon 4-3-2-1 nozzle results, we apply the code to predict K-shell yields from 4-3-2-1 nozzle loads on DQ that contain a low-Z gas in their outer shells. We show results for DQ operating under drive voltage conditions similar to past experiments as well as voltage conditions that DQ is likely to achieve in the future. In the latter case, it is assumed that DQ is operating at 90 percent of its stated voltage (according to Pat Corcoran of Titan, this should be achievable). So far the DQ argon experiments have behaved as if only 82 percent of the voltage was driving the implosion.

B. Benchmarking the One Dimensional Model to the Z, Double-Eagle and Decade Quad Argon Experiments

The 1D calculations are benchmarked against the K-shell yields measured during the argon 4-3-2-1 nozzle experiments on Double-Eagle (DE),[1] Sandia National Laboratories' (SNL) Z generator,[2] and DQ (December 2001experiments).[3]

The electrical circuits of these generators are modeled as RL circuits driven by an open circuit voltage profile; see Figure 1. The DE profile was obtained from Jerry Levine at Titan and the DQ profile was obtained from Pat Corcoran, also at Titan. Chris Deeney from SNL supplied us with the Z machine voltage profile. In order to match the experimental implosion times with the peak value of measured current, the Z generator voltage is multiplied by a factor of 0.87 and the DQ

116

voltage is multiplied by 0.82. This factor is (0.82 x 70/85) for DQ calculations made under reduced voltage conditions, i.e., 70 kV as opposed to a full 85 kV charge voltage.

The mass distribution used in the calculations is taken from the measured gas distribution obtained from interferometry measurements performed at the Naval Research Laboratory.[4]

The tabular collisional radiative equilibrium (TCRE) model[5] was employed to rapidly perform (A 10 minute TCRE calculation reasonably approximates a full 15 hour probability of escape radiation transport calculation) numerous 80 zone 1D calculations, so that a large parameter space of multipliers on transport coefficients could be explored. The goal of this exploration was to optimally match the calculated K-shell yields to those attained from the above mentioned experiments. Once a judicious choice of multipliers is made, full probability of escape radiation transport calculations are performed using these parameters. For the 4-3-2-1 nozzle configuration we found that calculations employing a multiplier of 30 on classical thermal conduction and 50 on viscosity provided the best match to the experiments. Coincidentally, these multipliers are nearly identical to those that provided the best match to earlier aluminum DE experiments, which were discussed in our earlier paper about phenomenological modeling of turbulence of Z-pinch plasmas.[6]

Even with these multipliers on the transport coefficients, measured radiative powers are typically much lower than calculated powers. This indicates that the experimental (multi-dimensional) plasmas are not thermalizing kinetic energy as rapidly as calculated in the 1D models. In order to account phenomenologically for this longer thermalization time the ion-electron heating rate is multiplied by the factor {Minimum (0.1, α x $1.0e18/N_i$)} in our model. Because of this treatment, the calculated ion temperature is not strictly a thermal temperature, i.e., it is both a measure of random microscopic motions (real ion temperature) and random macroscopic turbulence. $\alpha = 1.25$ is the value that provides the optimal match to all the above experiments.

Comparisons between measured and calculated K-shell yields are displayed in Figures 2-5, for DE, DQ - 70 kV charge, DQ - 85 kV charge, and Z, respectively. These figures show that indeed we have chosen a set of enhancements to the transport coefficients that produces a reasonable match between calculated and measured K-shell yields. On the one hand, there is no guarantee that we have reasonably captured the physics that takes place in the experimental 4-3-2-1 nozzle implosions via this phenomenological modeling. On the other hand, we have produced a reasonable "best fit" model that covers such a broad region in the parameter space of drive currents and mass loads that it is useful for predicting K-shell yields for future 4-3-2-1 nozzle experiments on DQ.

Figure 5 also displays the 0D model predictions for K-shell yield on Z. Clearly, if Z operated normally and these are representative yields at the given mass load for this configuration, these 0D models over predict the K-shell yield. The 1D phenomenological models are inherently more flexible than the 0D models when it comes to matching K-shell yields over a broad experimental parameter space. This flexibility allows one to self-consistently match the calculated K-shell yields to the measured yields on Z. It is primarily the enhancement in thermal conduction that is responsible for the deviation between the 0D and the 1D model predictions. One can speculate that this indicates that there is more energy exchange occurring between the core and outer

117

regions of the pinch than is modeled in 1D without enhanced thermal conduction. Mixing of the inner with the outer puff gas or more radiative transfer occurring for the low energy photons than is presently modeled are a couple of possible mechanisms for this exchange.

Pat Corcoran and other members of the DTRA PRS community that work with DQ's pulse power, think that DQ should be able to operate at a drive voltage level that is 90 percent of the open circuit voltage profile (0.9 x V_{oc}) shown in Figure 1. If this is achievable, then the calculated K-yields shown in Figure 7 should also be achievable. Given that the measured K-yield for the 250 μg/cm load driven by 0.82 x V_{oc} (Fig. 5) is larger than the calculated yield, one can expect the K-yield for the same mass load imploded with 0.9 x V_{oc} to be higher than the calculated yield shown in Figure 6. An I^4 K-shell yield scaling prediction for a 250 μg/cm load driven by 0.9 x V_{oc} is 9.5 kJ/cm.

C. Results of Calculations Employing a Low-Z Gas in the Outer Shell

In addition to the above results, Figures 2-6 also display the results of the calculations for which argon was replaced with carbon in the outer shell of the double-puff nozzle. While carbon is not typically in gaseous form, the radiative and hydrodynamic properties of carbon should be similar to nitrogen gas, carbon monoxide, mixtures of nitrogen and deuterium, and mixtures of nitrogen and helium. The idea behind replacing argon with a low-Z gas is that its lower radiative losses maintain the outer shell at a hotter temperature than it would be if argon were utilized. This consequently insulates the core plasma and allows it to radiate at a higher temperature, i.e. at temperatures more conducive for producing K-shell emission.

We originally tried putting methane (CH_4) in the outer shell, but this load was difficult to compress and heat compared to pure carbon. The reason for this is that on a per-unit-mass basis there are twice as many ions and electrons introduced to the plasma when hydrogen is used as opposed to higher-Z elements. A few CD_2 calculations were performed and their results were similar to the carbon calculations. Neon was also tried in two DQ loads (Fig. 3), but it radiated so well in its K-shell that it had a higher radiative cooling rate and radiated more total energy than the all-argon loads on DQ. In this instance, the presence of neon cooled the core region of the plasma to where it couldn't sustain the temperatures needed for K-shell emission. Perhaps on the Z machine, which has the energy to radiate much higher in the argon L-shell as well as the ability to burn through the neon K shell, there may be an advantage to using this load.

These results show that the major effect of the low-Z gas is to move the optimal conditions for producing argon K-shell yield to a larger mass and current regime. The presence of the low-Z gas reduces the ability of the plasma to radiatively cool as the plasma stagnates. This reduced cooling means that a larger mass plasma can be imploded and sustain high core temperatures before the radiative cooling rate is in strong competition with the rate at which kinetic energy is thermalized during stagnation. Such a higher current and mass regime is well suited for a long implosion time machine like DQ. The results for the DQ imploded with 0.9 x V_{oc} (Fig. 6) show that the Ar/carbon load is potentially a better radiator of argon K-shell emission than an all-argon load.

118

Figure 2 shows that there was no advantage to employing an Ar/carbon load on DE. The reason being that the reduced radiative cooling ability of this load made it more difficult to compress and consequently couple energy into at stagnation. In part, some of this is because these loads are imploding after the peak in the DE short circuit current profile.

D. Summary

This work shows that by an appropriate choice of transport coefficients the 1D phenomenological models are capable of matching the experimental K-shell yields over a broad parameter space of current and mass for a given load configuration such as the 4-3-2-1 nozzle. The models indicate that the significant fall off in K-shell emission that occurs for the larger mass experiments is due to a larger than expected exchange of energy between the inner and outer shells. An effect that is modeled phenomenologically by enhancing thermal conduction. Such an exchange might be due to plasma mixing or larger radiative cooling than modeled at present. The models predict that an argon 4-3-2-1 nozzle load driven by 90 percent of the stated DQ voltage should produce in excess of 34 kJ of K-shell emission.

Following up on a recommendation from the PRS community we investigated theoretically the radiative performance of the 4-3-2-1 nozzle in which argon was replaced by a low-Z gas in the outer shell. These results are very encouraging because they show increased K-shell yields and that the optimal regime for producing K-shell emission is moved to larger mass and higher current, both of which are favorable to DQ.

Given that these results are based on phenomenological models, any conclusions based on these results are somewhat speculative. Nevertheless, this study strongly indicates that performing experiments to investigate this issue would be worthwhile for several reasons: (1) Ar/low-Z loads are potentially a better PRS load for DQ, (2) similar to varying the mass fraction between the inner and outer shell, an Ar/low-Z gas provides another option for optimizing yield, and (3) allows us to test the validity of our models.

References

1. H. Sze, P. L. Coleman, B. H. Failor, A. Fisher, J. S. Levine, et al., *Phys. of Plasmas* **7**,1 (2000).
2. H. Sze, P. L. Coleman, J. Bannister, B. H. Failor, A. Fisher, et al., *Phys. of Plasmas* **8**, 3135 (2001).
3. J. Levine, private communication, Titan Systems Corporation.
4. Y. Song, P. Coleman, B. H. Failor, R. Ingermanson, J. S. Levine, H. Sze, E. Waisman, R. J. Commisso, T. Cochran, J. Davis, B. Moosman, A. L. Velekovich, B. V. Weber, D. Bell and R. Schneider, *Rev. Sci. Instrum.* **71**, 3080 (2000).
5. J. W. Thornhill, J. P. Aruzese, J. Davis, R. W. Clark, et al., *Phys. of Plasmas* **8**, 3480 (2001).
6. J. W. Thornhill, K. G. Whitney, C. Deeney, and P. D. LePell, *Phys. of Plasmas* **1**, 321 (1994).
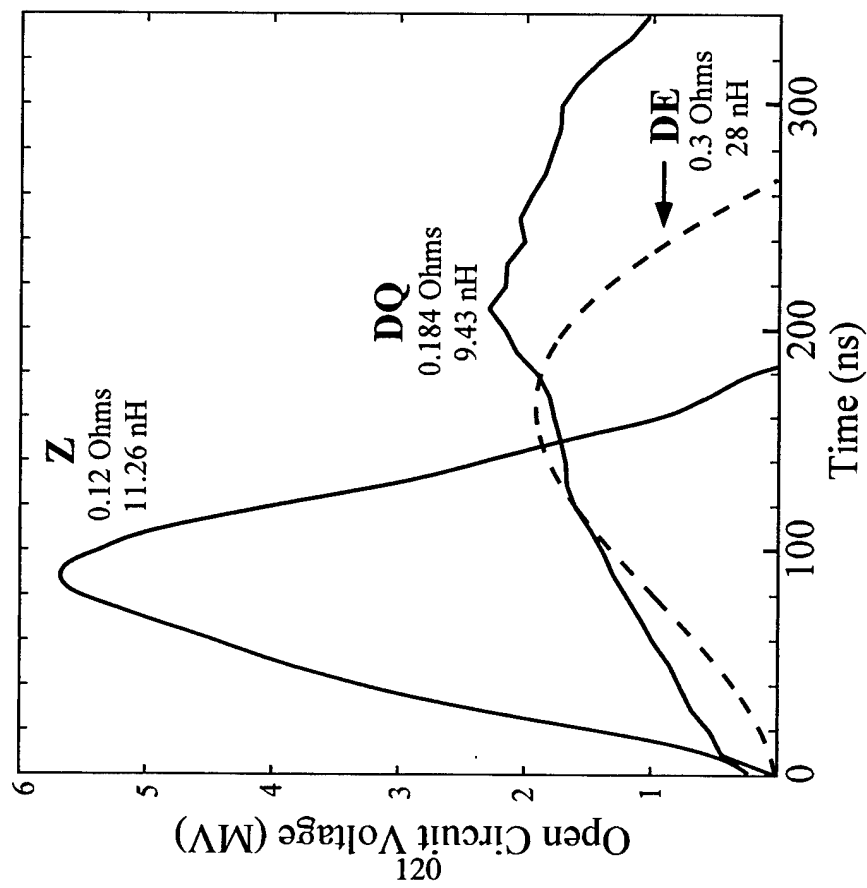
Fig. 2 Double-Eagle results for argon 4-3-2-1 nozzle experiments and calculations.

Fig. 1 Open circuit voltage profiles for Double-Eagle, Decade Quad, and the Z generator

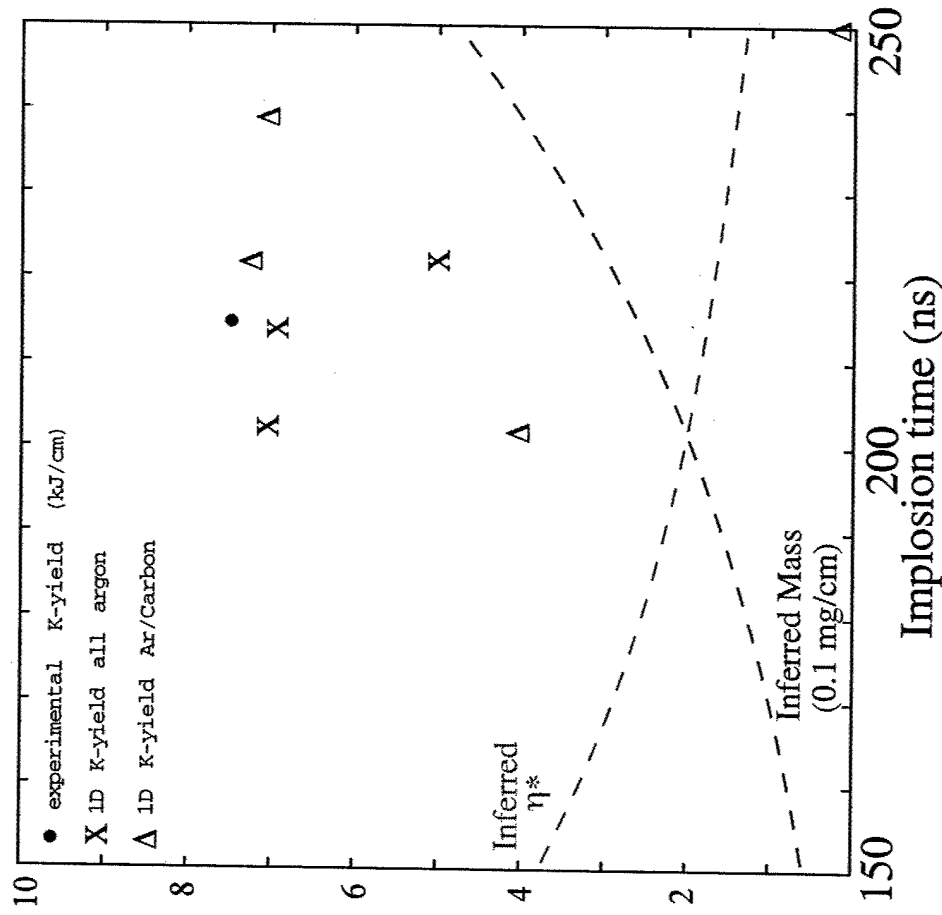Fig. 4 Decade Quad (85 kV) experimental and calculated results.

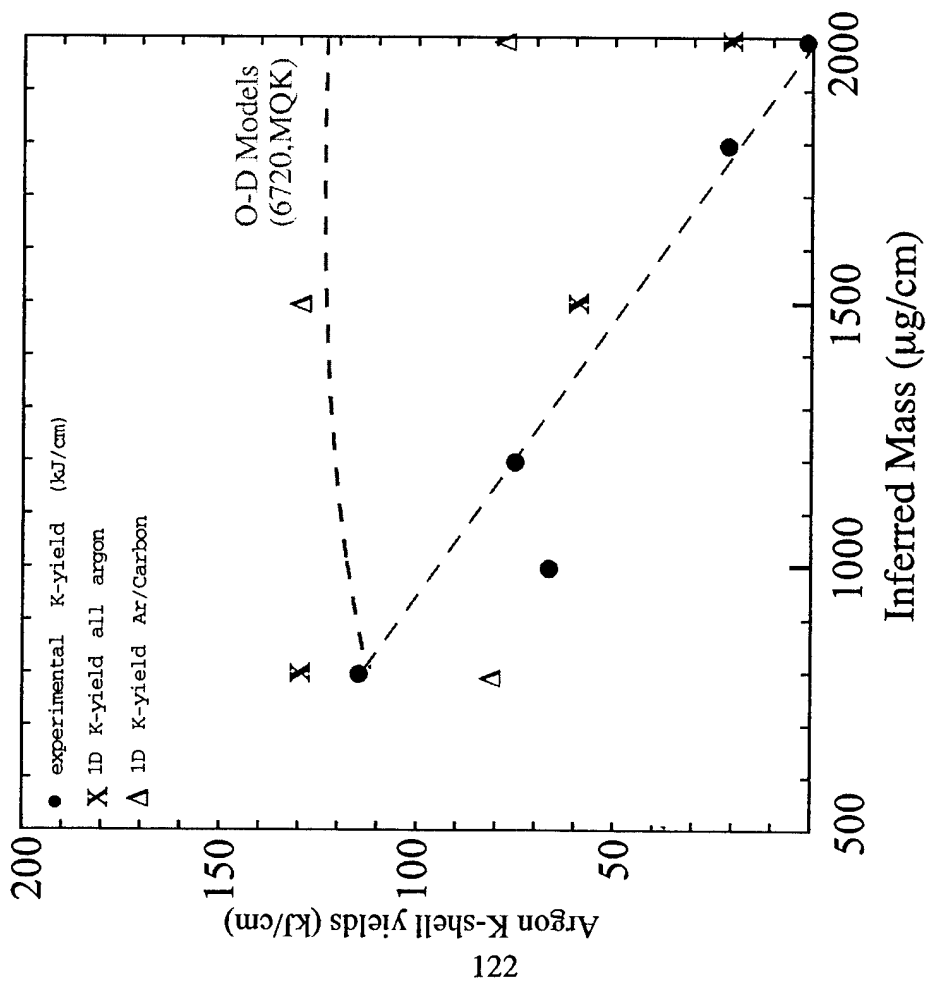Fig. 3 Decade Quad reduced voltage (70 kV) experimental and calculated results.

121

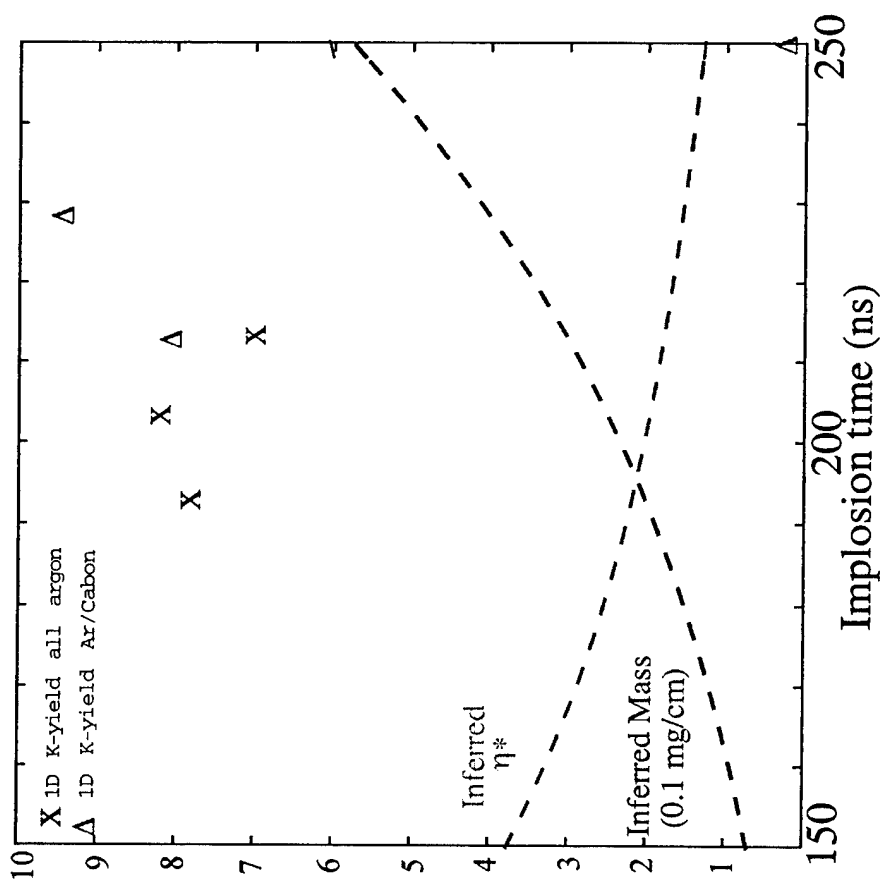Fig. 5 Z Generator results for 2001 experiments and calculations.

Fig. 6 Decade Quad calculated results for DQ operating at 90 percent of designed operating voltage.

V. Micro-Instability Induced Enhanced Energy Absorption in Long Current Rise-time Saturn Experiments

I. Introduction

The reconfiguration of Saturn from a short to a long current risetime machine has produced significant increases in total x-ray output by factors of 2 to 4 in wire experiments with aluminum and tungsten. This enhanced output can only be explained if an enhanced resistive energy coupling of the z-pinch to the Saturn generator is assumed. In work carried out during the previous year, the generation, build-up, and dissipation of magnetic flux tube energy within the plasma was investigated as a way of accounting for this enhanced resistive energy coupling. The buildup of flux-tube energy was hypothesized to occur as an added consequence of Rayleigh-Taylor instability growth at the surface of the pinch. Because no theory exists for such energy build-up, last year's analysis was entirely phenomenological in which phenomenological parameters were set by benchmarking model calculations to experimental data from one of the shots. The model was then used to investigate prospects for diverting more of this hypothesized flux tube energy into K-shell radiation.

In the investigations performed this year, an alternative approach to modeling enhanced energy coupling was pursued. It had been argued that conditions at the surface of a pinch are created that lead to the build-up of plasma micro-instabilities[1]. In Ref. (1), a formula for enhanced resistivity at the plasma surface that is produced by the hybrid drift-wave instability was proposed and investigated. It had the property of being temperature insensitive and of increasing as the density at the pinch surface decreased in contrast to the Spitzer resistivity, which is essentially density independent and decreases with temperature increases. Thus, as energy flows into and couples to the pinch at its surface, its surface temperature increases and its density decreases. When this occurs, Spitzer resistivity reduces, while drift-wave resistivity increases, the resistive energy coupling. Consequently, the approach taken this year to investigate enhanced z-pinch energy coupling was to assume that it was surface micro-instability, rather than magnetic flux-tube, induced.

The work carried out this year had three phases. This report is structured to describe each in sections III-V. First, in section II, the experimental data that motivated this work are briefly described along with some theoretical challenges that the data presents. In section III, 0-D calculations are described that demonstrate the need for enhanced resistive coupling and motivate the work that follows. These calculations describe the build-up of pinch energy during the run-in phase of the dynamics, but they cannot determine how this energy is converted into x rays. For this problem, one must self-consistently couple the generator to the pinch fluid dynamics. This coupling problem is briefly discussed in section IV, where expressions for the z-pinch circuit resistance are derived in terms of the pinch's surface resistivity. The self-consistent coupling of generator to pinch is easily accomplished in a 1-D fluid calculation, and these calculations are described in section V. The Saturn experiments manifest enhanced coupling because they produced an enhanced x-ray output. Therefore, 1-D fluid calculations must also demonstrate the capability to channel added energy inputs into x rays, and, in section V, some of the modeling issues that this channeling raises are also described. To address these issues, the simplifying procedure of

---

[1] A. E. Robson, Phys. of Fluids B, **3**, 1461 (1991).

specifying the time history of the plasma resistance was adopted in order to initially understand how substantial amounts of added energy input would impact the hydrodynamics. The problem was to determine the kind of resistance increases that are needed to produce the x-ray power pulses that had been observed, both in their energy content and in their having or not having a late-time foot following the main pulse. The feasibility of substantially increasing both the energy input and the x-ray output of the pinch was demonstrated in these calculations and is summarized in section VI.

II. Experimental Data

In its long current-risetime mode of operation, Saturn has an ample supply of current for large wire-number aluminum loads to be effectively utilized at radii $\geq$ 2 cm. Thus, interwire gap spacings can be kept small. Small gap spacings allow plasma shells to form prior to implosion. In a series of shots, in which only wire number was varied, an optimal spacing was found using 180 wires. The aluminum wire arrays in these shots were 2 cm long, 4 cm in diameter, and contained 616 μg/cm. This 180 wire experiment was repeated 3 times. The total x-ray power pulse recorded in each experiment is shown in Fig. 1, and a running time integration of these powers is shown in Fig. 2.
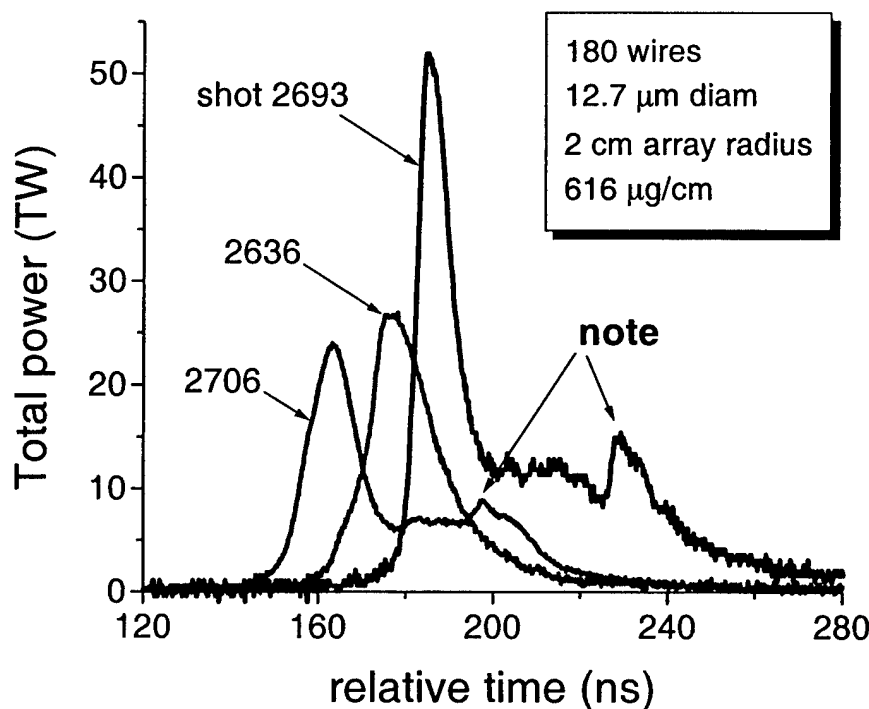
Figure 1. Total x-ray power versus time.

Figures 1 and 2 illustrate several problems that any attempt to model these experiments must address. The main problem is: what causes the extreme shot-to-shot variations in x-ray output that are seen? In shot 2693, the peak x-ray intensity is twice that of the other two shots, and the power pulse has a substantial late-time foot. Shot 2706 also has a foot, but shot 2636 does not. Fig. 2

shows that shot 2693 radiated twice the energy of the other two shots, but that half of this energy was late-time. Shot 2706, on the other hand, had half the energy in its main pulse as did shots 2693 and 2636, although it eventually radiated the same amount of energy as shot 2636. Shot 2636 did radiate roughly the same amount ($\sim$ 500 kJ) in one pulse as the main pulse of shot 2693, but it had essentially no foot emission. Note, finally, that the variations that were observed in K-shell emission (in Fig. 3) were not as large as those seen in soft x-ray emission; they varied only between 53 and 64 kJ.
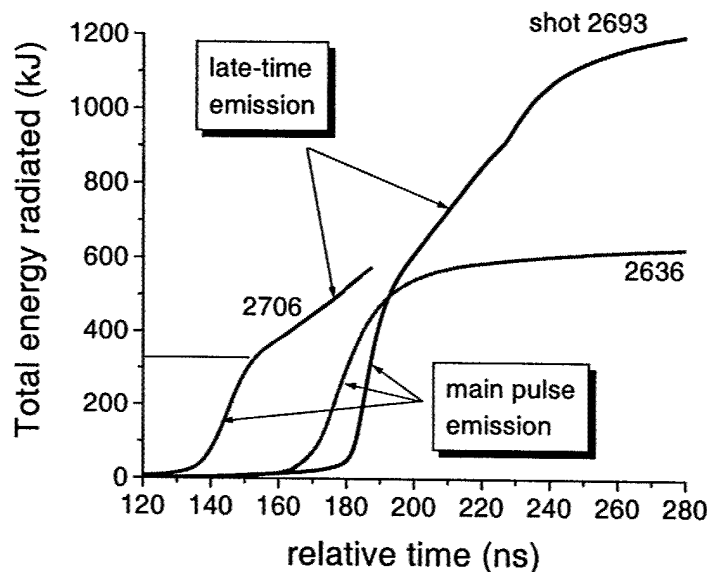
Figure 2. Total x-ray energy radiated as a function of time.

K-shell Energy Radiated vs Time
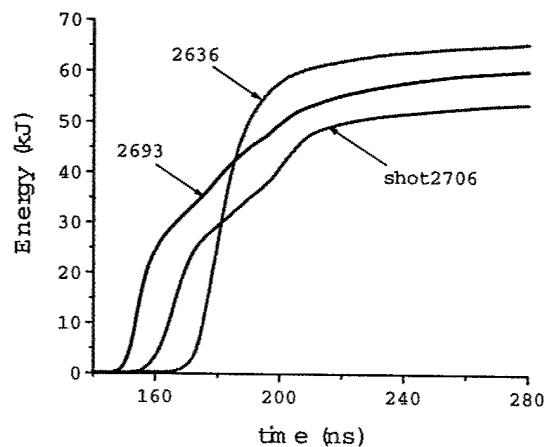
Figure 3. K-shell x-ray energy radiated as a function of time.

An analysis of these three shots suggests that two to four times as much energy is radiated

125

from these pinches as can be supplied in conventional hydrodynamic or 0-D modeling by the sum of the $j \times B$ work and Spitzer Ohmic heating. The pinch must be made more resistive in order for more generator energy to couple to it. However, this raises two questions: what is the source of this added (anomalous) resistivity and how well can the variations that are seen in the experimental x-ray data be explained by variable amounts of early-time and late-time anomalous resistivity? Moreover, if this added coupling can be introduced into hydrodynamic calculations, a further question arises of how efficiently this extra Ohmic heating can be converted into x rays.

Support for late-time energy coupling increases comes from a direct measurement of z-pinch impedance (in Fig. 4) that was made in Russia on the Tomsk IMRI-IV generator. A sharp rise in resistivity was observed late in time just before the pinch assembled on axis. The calculations that are described later in this report were guided by this observation. In all calculations, large increases in resistivity were made prior to the time of implosion, and the turn-on time was taken to be relatively short.

Measured $R_{\ell oad}$
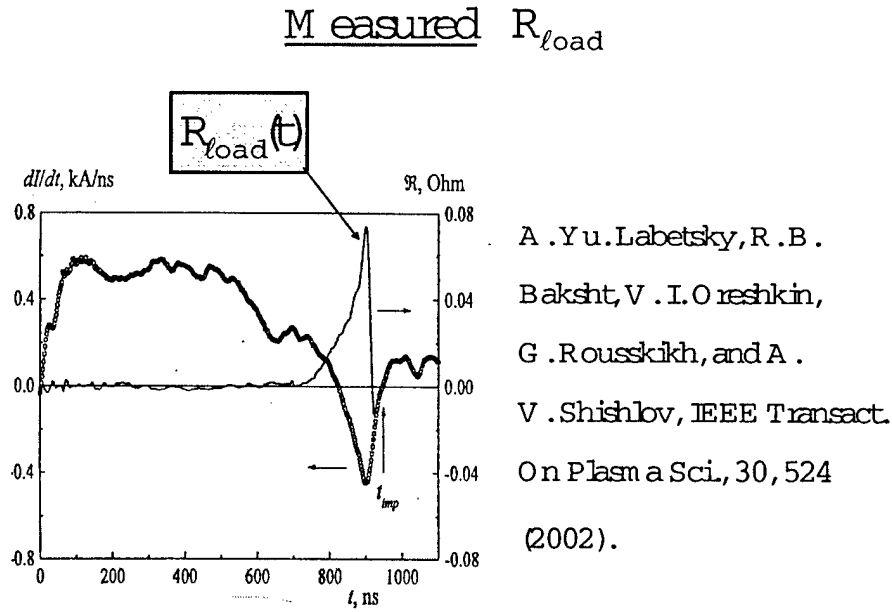
Figure 4. Measured load resistance as a function of time.

III. 0-D Modeling

A set of 0-D calculations using Saturn's long current-risetime circuit model was carried out to evaluate how adding load resistance changes the energy coupling to z-pinch loads. These calculations demonstrate the need for substantial increases in pinch resistivity if the energetics of shots 2706, 2636, and 2693 are to be modeled. The circuit equation used for these calculations is

$$\frac{d}{dt}\Big((L_{gen} + L_{\ell oad}(t))I(t)\Big) + \Big(R_{gen} + R_{\ell oad}(t)\Big)I(t) = V(t),$$

126

from which one derives the energy equation,

$$\frac{d}{dt}\left(\frac{1}{2}L_{gen}I^2 + \frac{1}{2}L_{\ell oad}I^2\right) + R_{gen}I^2 + P^{Load} = V(t)I(t).$$

It describes the conversion of generator power, VI, into the build-up of magnetic field energy, Ohmic heating losses in the generator, and energy flow, P^{Load}, into the z-pinch, which is given by

$$P^{Load} = \frac{1}{2}\frac{dL_{\ell oad}}{dt} + R_{\ell oad}I^2.$$

The load inductance, $L_{\ell oad}(b(t))$, which is defined in terms of $b(t)$, the z-pinch outer boundary, and r_{rc}, the radius of the return current path, is given by

$$L_{\ell oad} = \frac{2\ell}{c^2}\ln\left(\frac{r_{rc}}{b(t)}\right).$$

In a 0-D model, this inductance is calculated, but the load resistance, $R_{\ell oad}$, is unknown and must be specified. Zero-D modeling assumes that an infinitesimally thin shell of plasma of mass, $m[\mu g/cm]$, is accelerated inward by the $j \times B$ forces acting on the plasma:

$$m\ell\frac{d^2b(t)}{dt^2} = \frac{\partial}{\partial b}\left(\frac{1}{2}L_{\ell oad}I^2\right) = -\frac{\ell}{c^2}\frac{I^2}{b}.$$

The energy equation,

$$\frac{d}{dt}\left(\frac{1}{2}m\ell\left(\frac{db}{dt}\right)^2\right) = \frac{1}{2}\frac{dL_{\ell oad}}{dt} = -\frac{\ell\dot{b}}{c^2b}I^2,$$

derived from this force equation equates the $\dot{L}_{\ell oad}$ term in $P_{\ell oad}$ to the build-up of kinetic energy in the pinch.

To calculate energy coupling of the Saturn circuit to a z-pinch using a 0-D model, one must make a specific choice for $R_{load}(t)$. In the calculations whose results are shown in Figs. 6 and 8, $R_{load}(t)$ was taken to be a function of the pinch radius, $b(t)$, and to increase rapidly to a maximum value of R_{load}^{max} as the implosion progressed and b decreased:

$$R_{\ell oad}(t) = \left\{\left(\frac{1 - b(t)/b_0}{0.3}\right)^4 \middle/ \left(1 + \left(\frac{1 - b(t)/b_0}{0.3}\right)^4\right)\right\}R_{\ell oad}^{max},$$

where b_0 is the initial wire array radius. Some typical implosion trajectories are shown in Fig. 5 that illustrate the different points in time at which the load resistance reaches a value of $0.5R_{\ell oad}^{max}$ at a distance of $0.7b_0$ for different massed loads.
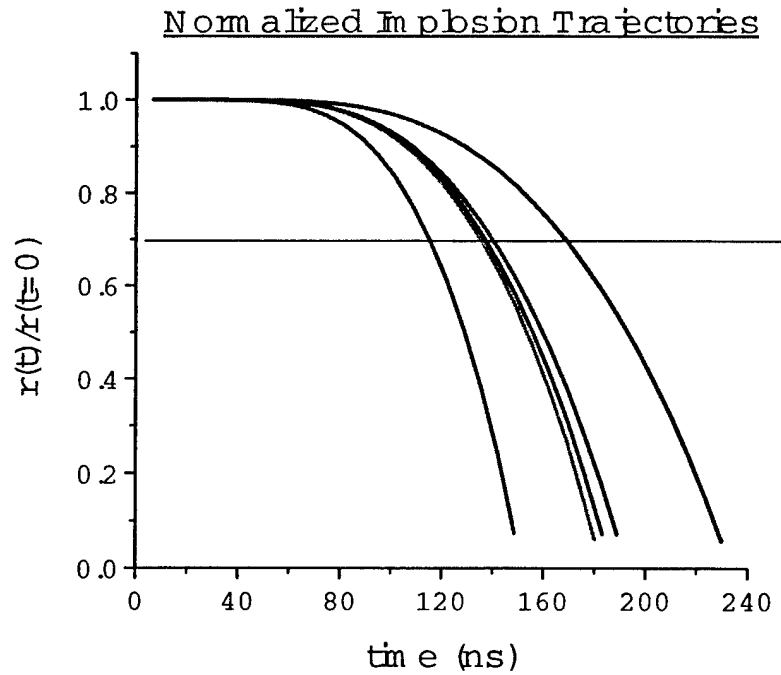
127

Normalized Implosion Trajectories

Figure 5. Implosion trajectories for different mass loads as a function of time. The masses range from 600 to 1800 μg/cm.

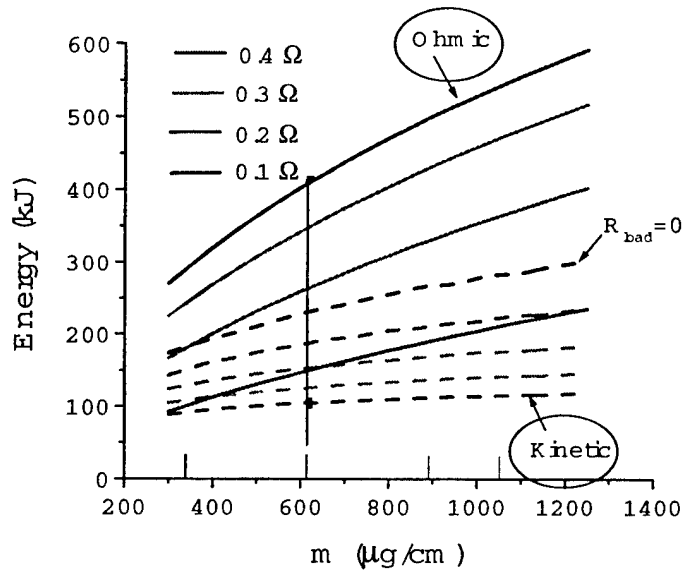**Load Energy Inputs for Different Maximum Load Resistances**

Figure 6. Calculated load energy inputs as a function of load mass for different values of maximum load resistance.

Fig. 6 shows how the Ohmic and kinetic energy inputs varied as a function of the load mass in these calculations. Four sets of calculations were made in which R_{load}^{max} was given different values of 0.1, 0.2, 0.3, and 0.4 Ω. Two important trends are seen in Fig. 6. One, as R_{load}^{max} increases, the kinetic energy generated during an implosion goes down while Ohmic heating moves dramatically upward. Two, for a given R_{load}^{max}, both the kinetic and Ohmic energy inputs increase as the load mass, and thus the implosion time, increases. This behavior with mass was seen in Saturn data (see the table in Fig. 7). A series of shots in which the load mass was varied, but all other load parameters were held fixed had been carried out. Total x-ray yields were generally found to increase as the load mass was increased, with one exception (in shot 2640 where $m = 328\mu g/cm$). This single-shot yield anomaly is consistent, however, with the shot-to-shot variability that is seen in Fig. 1 and that would have been present for the $m = 616\mu g/cm$ entry in the table had shot 2693 been substituted for shot 2636. Note that the sum of the kinetic and Ohmic energies at $m = 616\mu g/cm$ in Fig. 6 exceeds 500 kJ. This is the minimum amount of input energy that would be required to produce the energy output that is seen in the main pulses of shots 2636 and 2693. Note also that when $R_{load}^{max} = 0$, less than 250 kJ of kinetic energy is generated during the implosion of the $m = 616\mu g/cm$ load. This energy is approximately a factor of two smaller than the amount of energy seen to be radiated during plasma assembly. Finally, Fig. 8 provides a reason for the increase in energy coupling that is seen as the pinch mass is increased; namely, implosion times increase along with the mass of the load, and the circuit has a longer time interval in which to deliver its energy to the load.

Variable Mass Experiments

Shot #	Mass (μg/cm)	Implosion Time (ns)	Total x-ray energy (kJ)	K-shell x-ray energy (kJ)	Total x-ray energy (main pulse) (kJ)	K-shell x-ray energy (main pulse) (kJ)
2640	328	134		51.2	334	20.1
2636	616	175	629	68.8	458	51.9
2637	887	183	736	47.3	382	26.6
2641	1050	184	845	39.2	546	21.2
2702	1576	208	1040	50.9	652	29.3

Figure 7. Measured implosion times and x-ray outputs for the shots in a set of variable mass experiments.

Energetics of Long-risetime Implosions
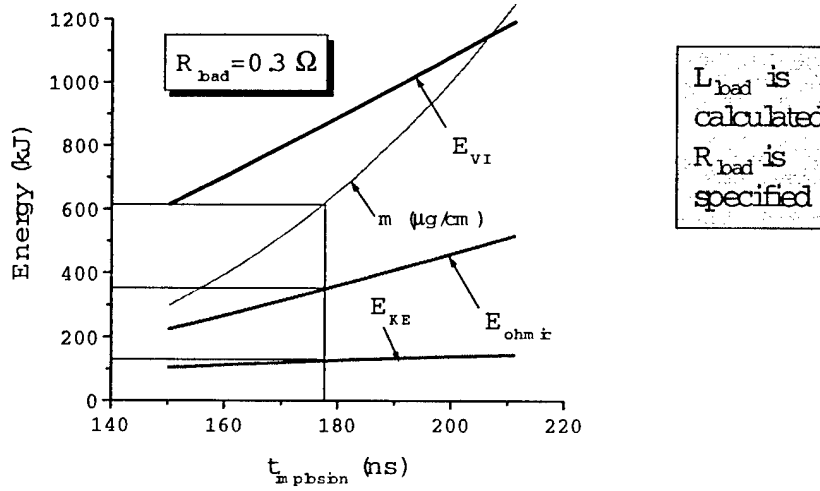
(0-D Modeling Saturn circuit model)

Figure 8. Calculated load and circuit energy inputs as a function of implosion time for a fixed value of maximum load resistance.

IV. Enhanced Energy Coupling

Zero-D models are, by design, unable to calculate how kinetic energy converts into x rays. For this, one needs a fluid description of how the plasma collides with itself on axis, at first thermalizing the kinetic energy that was built up during implosion, and then ionizing, and radiating. In order to couple this more complex fluid dynamics to a circuit model, one must augment the description of the load as a variable inductance and resistance with a description of it as a dynamic termination element in a transmission line. Fig. 9 depicts how the circuit picture of the load needs to be supplemented by the transmission line picture. In this figure, the transmission line is terminated ideally in a perfectly cylindrical vacuum diode cavity that has perfectly conducting walls and in which a cylindrically unperturbed and symmetric plasma of finite length, ℓ exists. The voltage drop, V_p, across the load in the circuit model is now represented by the voltage drop in the transmission line across the entrance to the vacuum diode. The power, P^{Diode}, flowing into the diode is determined by the transmission line electromagnetic fields, E_r and B_θ, while the power, P^{Load}, flowing into the z-pinch is determined by the fields, E_z and B_θ.

Because Spitzer resistivity is too small to account for the amount of Ohmic heating that had to be inserted into the above 0-D calculations, one must seek other mechanisms by which to enhance a z-pinch's resistivity. In order to maintain self-consistency with the circuit equation,

$$P^{Load} = \left(\frac{1}{2} \frac{dL_{\ell oad}}{dt} + R_{\ell oad} \right) I^2 .$$

130

Energy flowing in the transmission line is coupled to the pinch at its outer surface and is calculated from the electromagnetic energy flowing through this moving surface, which is located at $b(t)$. The dimensionality of the fluid dynamics is immaterial to this coupling calculation; however, in order to derive an analytic expression for this flux, one must specialize to the ideal 1-D geometry depicted in Fig. 9. Then, from the total energy equation that is derived from the fluid equations in such a geometry, one finds that

$$P^{Load} = Lim_{\epsilon \to 0} \left\{ 2\pi \ell r \left(\frac{dr}{dt} \frac{B_\theta^2}{8\pi} + \frac{c}{4\pi} E_z B_\theta \right) \right\} \Big|_{r=b(t)-\epsilon}.$$

To evaluate this Poynting flux, one must insert the surface values for B_θ and E_z, which are obtained from Ampere's law and from Ohm's law in the plasma:

$$B_\theta = \frac{2I(t)}{cb(t)}, \qquad E_z = -\frac{1}{c} \frac{db}{dt} B_\theta + \frac{1}{n_e e} \left(\alpha_\perp \frac{j_z}{n_e e} + \beta_\Lambda \partial_r (k_B T_e) \right).$$

Z-pinch Transmission Line Modeling
Provides an Alternative Approach to R_{load}
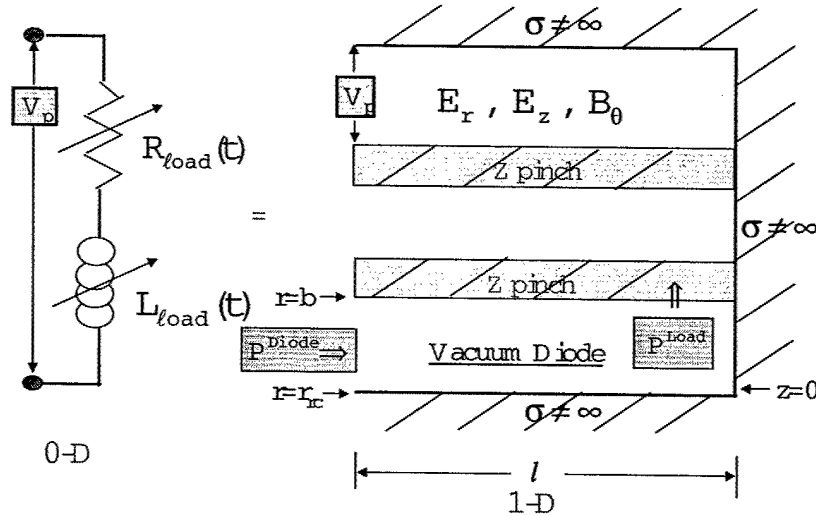
Figure 9. A transmission line-dynamics picture of the lumped circuit-model load.

By comparing the resulting expression for P^{Load} with its circuit equation expression, one finds expressions for both $L_{\ell oad}(t)$ and $R_{\ell oad}(t)$. The expression for $L_{\ell oad}(t)$,

$$L_{\ell oad}(t) = \frac{2\ell}{c^2} \ln \left(\frac{r_{rc}}{b(t)} \right),$$

is in agreement with 0-D modeling. The expression for $R_{\ell oad}(t)$ is unique to this calculation:

$$R_{\ell oad} = \hat{\alpha} \frac{\ell \eta_0}{A_j} + \frac{1}{2} x_{tr} \hat{\beta}_\Lambda \frac{\ell \eta_0}{A_{th}}.$$

131

The two areas, A_j and A_{th}, appearing in this equation are defined by the physical surface current density and by a theoretically defined surface current density, $j_{th} \equiv n_e e v_{th}$, where the thermal velocity, v_{th}, is defined by $v_{th} \equiv \sqrt{2k_B T_e/m_e}$:

$$A_j \equiv \frac{I}{j(r=b)}, \qquad A_{th} \equiv \frac{I}{j_{th}(r=b)}.$$

The quantities, $\hat{\alpha}_\perp$, β_Λ, and x_{tr} are dimensionless and are defined by $\hat{\alpha}_\perp \equiv 1 - (\alpha_1' x_b^2 + \alpha_0')/\Delta$, $\hat{\beta}_\Lambda \equiv x_b(\beta_1'' x_b^2 + \beta_0'')/\Delta$, and $x_{tr} \equiv v_{th}\tau_e\partial_r \ln(T_e)$. The coefficients in these definitions are found in the reference below[2], and $x_b \equiv eB_\theta \tau_e/(m_e c)$, where τ_e is the electron-electron collision time. The resistivity, η_0, is defined by $\eta_0 \equiv m_e/(n_e e^2 \tau_e)$.

Because all of the quantities appearing in the expression for $R_{\ell oad}$ are evaluated at the surface of the pinch where temperatures are high, densities low, and drift velocities high, conditions are right for the initiation and growth of micro-instabilities. The hybrid drift wave candidate instability of Ref. 1, which is capable of producing significant resistivity increases, can be introduced into $R_{\ell oad}$ through the replacement,

$$\hat{\alpha}\eta_0 \to \hat{\alpha}\eta_0 + \eta_{LH},$$

The drift-wave resistivity, η_{LH}, is proportional to the current density squared and to the B-field, and it is inversely proportional to the electron pressure and to the ion density squared (see Reference 1). Its dependence on these quantities indicates that the fluid dynamics will become highly nonlinear when this resistivity is introduced into it. With added resistivity, the rate of B-field, and therefore current, diffusion away from the surface increases. However, the plasma's resistance is dependent on this surface current density as well as on the surface Ohmic heating rate.

Transmission line energy flowing into the z-pinch at its surface must then be transported into its interior by the dynamics described by the fluid equations. From these equations, one can derive an equation for the build-up of energy within any region, i, of the plasma. In 1-D, these regions are easily defined by inner and outer radii, $r_i(t)$ and $r_{i+1}(t)$ respectively and:

$$\frac{d}{dt}\left(U_{Fluid}^i + U_B^i + U_{rad}^i\right) = -2\pi\ell r\left\{\frac{dr}{dt}\left(u_{rad}+u_B\right)+S_{rad}+\frac{c}{4\pi}E_z B_\theta +(P\cdot v)_r+q_r\right\}\Bigg|_{r=r_i(t)}^{r=r_{i+1}(t)},$$

where u_{rad} and $u_B = B_\theta^2/(8\pi)$ are the energy densities of the radiation field and magnetic field respectively and S_{rad} is the radiation field Poynting vector flux. The energies, U_{Fluid}^i, U_B^i, and U_{rad}^i, are integrations over region i of the fluid, magnetic field, and radiation energy densities:

$$U_{Fluid}^i = 2\pi\ell\int_{r_i(t)}^{r_{i+1}(t)} dr\, r u_{Fluid}, \qquad U_B^i = 2\pi\ell\int_{r_i(t)}^{r_{i+1}(t)} dr\, r\frac{B_\theta^2}{8\pi},$$

and

$$U_{rad}^i = 2\pi\ell\int_{r_i(t)}^{r_{i+1}(t)} dr\, r u_{rad}.$$

[2] S. I. Braginskii, in *Reviews of Plasma Physics*, edited by M. A. Leontovich (Consultants Bureau, New York, 1965), Vol 1, pp 205-311.

The fluid energy density is a sum of kinetic, thermal, and ionization energy densities. The four terms describing the flow of energy across region boundaries represent energy transfer by (1) magnetic field diffusion, $(c/4\pi)E_z B_\theta$, (2) heat conduction, q_r, (3) shock heating and pdV work, $(P \cdot v)_r$, and (4) radiation transport, S_{rad}. When these terms are large, energy that is coupled in at the pinch's surface moves quickly into its interior. When these terms are not large, surface heating will cause the plasma's outer regions to blow out and decouple from the plasma core, where the bulk of the x-ray emission occurs.

Previous experience with plasma fluid dynamics has shown that heat conduction, magnetic field diffusion, and shock heating are limited in the amount of energy that they can transport across fluid boundaries. Under the right plasma conditions, however, soft x-ray transport has the potential to significantly increase this energy flow. However, the modeling of radiative transport at low temperatures by soft x rays is generally inadequately modeled, at present, to quantify, with accuracy, the strength of this transport. The greater complexity of the soft x-ray transport problem is the reason. In this energy domain, the transport can be more nearly blackbody than at higher photon energies (hence Sandia's ICF program), and escape probability methods are not fully adequate.

A way of estimating the strength of soft x-ray energy transport in comparison to electron heat transport is to compare the formula for blackbody radiation conduction, which is given by,

$$q_{rad} = -\kappa_{rad}\partial_r T_e, \qquad \kappa_{rad} = \frac{16\sigma T_e^3}{3\rho K_R},$$

where σ is the Stefan-Boltzmann constant, ρ is the plasma density, and K_R is a Rosseland mean opacity, to the formula for electron heat conduction:

$$q_e = -\kappa_e \partial_r T_e, \qquad \kappa_e = \hat{\kappa}_e \frac{n_e k_B^2 T_e}{m_e},$$

where $\hat{\kappa}_e$ is a dimensionless constant ≤ 10 (see Reference 2). Two questions about the strength of q_{rad} relative to q_e were asked and answered using these formulas. One, for what values of K_R will q_{rad} be equal to some multiple, α, of q_e? Setting $q_{rad} = \alpha q_e$ yields

$$K_R = \frac{32}{3\alpha\rho\hat{\kappa}_e}\left(\frac{(\sigma/c)T_e^4}{n_e k_b T_e}\right)\frac{c}{v_{th}}\frac{1}{v_{th}\tau_e}, \qquad L_{rad} \equiv \frac{1}{\rho K_R},$$

where $v_{th} \equiv \sqrt{2k_B T_e/m_e}$, τ_e is the electron-electron collision time, and L_{rad} is the photon mean free path. Two, how do these values compare to published values of K_R, computed for aluminum? Answers to these questions are found in Figs. 10, 11, and 12. They were obtained through the post-processing of a typical 1-D hydrodynamics calculation of a long current-risetime z-pinch implosion.

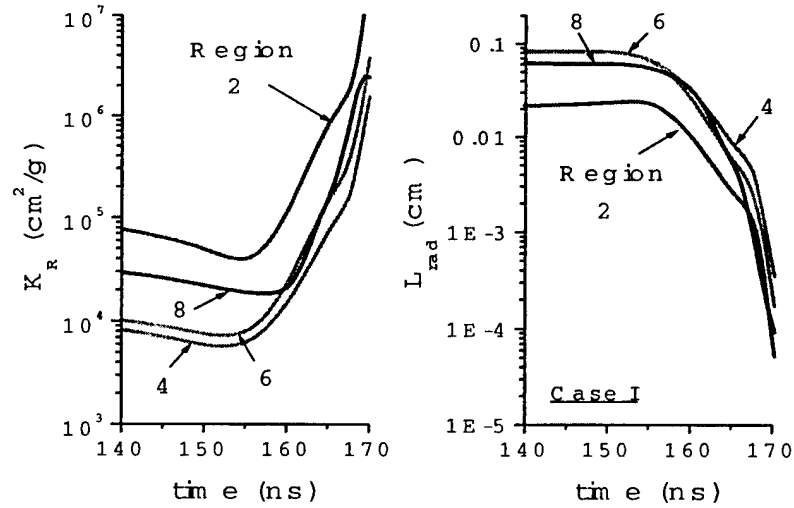# Calculated 1-D MHD K_R & L_{rad} ($\alpha = 10^4$)

Figure 10. Rosseland mean opacities and x-ray mean-free paths obtained from the above formulas at different locations in the pinch assuming $\alpha = 10^4$.

Initial Mass Distribution
(shell implosion calculation, 11 regions,
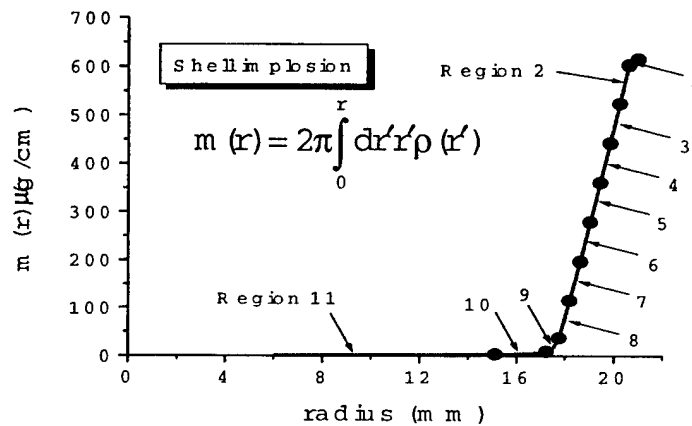## 9 zones per region)

$$m(r) = 2\pi \int_0^r dr' r' \rho(r')$$

Figure 11. The initial mass distribution for the 1-D calculations corresponds to an ideal plasma shell implosion.
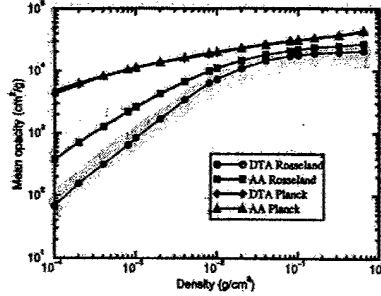
134

A lum inum Rosseland M ean Calculations

FIG. 3. The Rosseland and Planck mean opacities for aluminum plasmas as a function of density at a temperature of 40 eV.
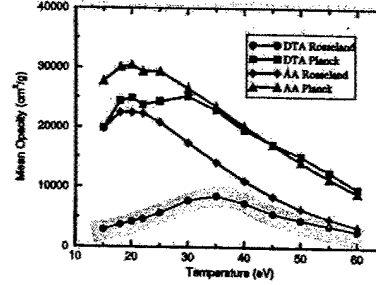
FIG. 5. The Rosseland and Planck mean opacities for aluminum plasmas as a function of temperature at a density of 0.01 g/cm³.

$$\frac{1}{K_R \, [cm^2/g]} = \int_0^\infty du \frac{W_R(u)}{K_{Al}(u)} \qquad W_R(u) = \frac{15}{4\pi^4} \frac{u^3 \exp(u)}{(1-\exp(u))^2}$$

J. Zeng and J. Yuan, Phys. Rev. E, 66, 016401 (2002).

Figure 12. Calculated values of the Rosseland mean opacity for aluminum.

The four curves that are shown in the two graphs of Fig. 10 represent values of K_R and L_{rad} that were calculated at different locations in the plasma. All of the 1-D calculations described in this report were ideal shell-like implosions in which the plasma mass was concentrated initially around a radius of 2 cm (see Fig. 11). For graphic purposes, the plasma was divided into 11 regions (as shown in Fig. 11), and each region contained 9 zones (except region 11, which contained 10 zones). The outer boundaries of some of these regions were used as the locations at which the curves in Fig. 10 were calculated. These curves illustrate that values of K_R in excess of 10^4 are already sufficiently small for q_{rad} to exceed q_e by a factor of 10^4. Moreover, since smaller values of K_R would increase the magnitude by which q_{rad} exceeds q_e and since the values of K_R that were calculated for aluminum (Fig. 12) are of the order of, but less than, 10^4 for plasma conditions similar to those found in these 1-D calculations, there is good reason to expect that energy transport by soft x rays should greatly exceed energy transport by electron heat conduction in calculations that are set up to model the Saturn experiments.

V. 1-D Modeling of the Saturn Experiments

The large contribution that soft x-ray transport is expected to play in redistributing energy during the later phases of a z-pinch implosion had to be put into the calculations described below phenomenologically. This was done by utilizing a multiplier of 10^4 on the electron heat conduction. The purpose of these calculations was to determine whether or not variable amounts of surface resistivity could be introduced into the calculations that would allow them to reproduce the total x-ray power pulse behavior (both as to size and shape) that is seen in Fig. 1. The strength of soft x-ray emissions that were calculated using escape probability methods also had to be

augmented (by a factor of 3), which is in accord with the modeling of energy transport by soft x rays within the plasma by means of a conduction equation. This procedure was used to offset some of the structural incompleteness in the L-shell model that was employed. Finally, the need to enhance resistivity in 1-D calculations is justified (as in the 0-D calculations) by the coupling results (illustrated in Fig. 13) that one obtains when only Spitzer resistivity is employed in the fluid calculations. The maximum energy that can be coupled by the implosion dynamics in this case is at most 275 kJ and only a small fraction of this energy ($\sim$ 25 kJ) comes from Ohmic heating.

Case 0 : No Anomalous Heating & a 1-D Calculation
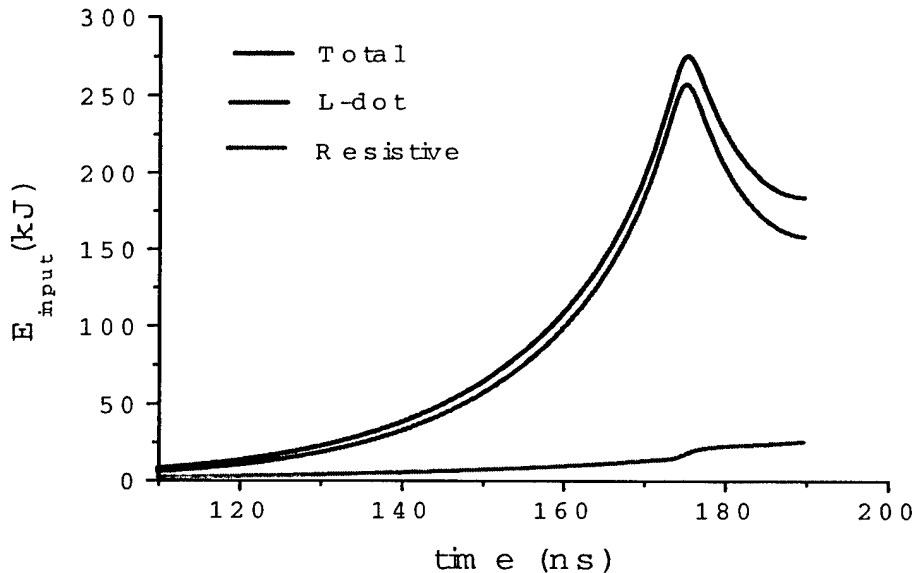
Figure 13. L-dot and resistive energy inputs versus time when there is no anomalous heating.

Because less than half the amount of energy was coupled to the pinch in this calculation as was coupled experimentally, less than half as much energy was radiated in the calculation as was seen experimentally. The calculated powers and radiated energies corresponding to the Fig. 13 implosion are shown in Fig. 14. Three powers are presented, one of the total x-ray output, one for the part of this output that lies above 1 kilovolt, and one for the line emission lying above 1 kilovolt (the K-shell lines). Although the total power peaks above 30 TW, the pulse is narrow so that less than 175 kJ of x rays are emitted (far less than the 600 kJ seen experimentally in Fig. 2. The calculated emissions above 1 kilovolt ($\sim$ 40 kJ) are also less than was seen experimentally in Fig. 3 (>55 kJ).

136

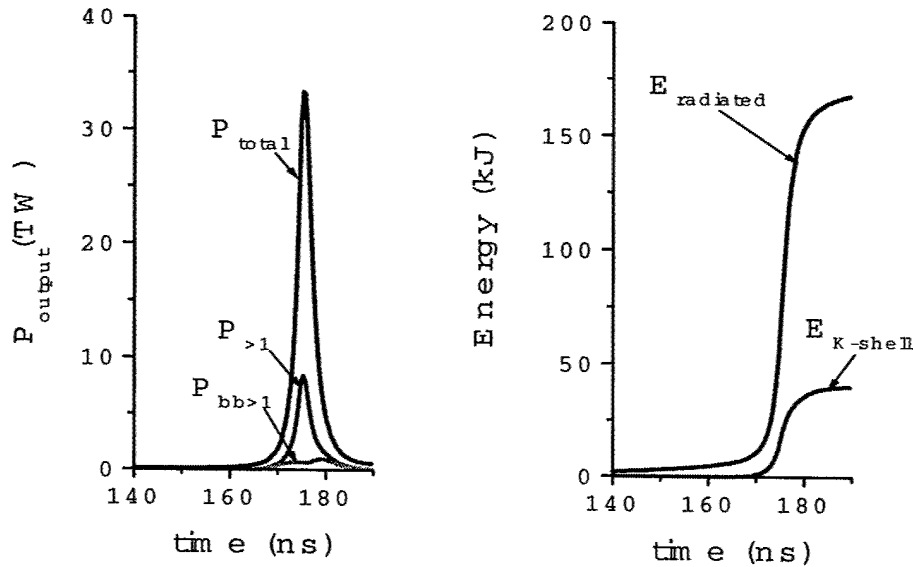# Case 0 Power and Energy Outputs

Figure 14. The x-ray powers and energies radiated versus time when there is no anomalous heating.

Spitzer resistivity is several orders of magnitude too small to account for the energy outputs seen in Figs. 2 and 3; hence, a large input of anomalous heating must be supplied in the 1-D calculations. Because this heating involves theoretical unknowns, its introduction into the fluid dynamics was carried out, at first, manually, similar to its introduction into the 0-D calculations. By adopting this procedure, one can more readily determine the kinds of added heating that are required to replicate the power pulses seen in Fig. 1. A fair degree of success in this venture was achieved when the two resistance time histories shown in Fig. 15 were employed. In one case, a Gaussian pulse of load resistance was added to the calculation; in case II, the same Gaussian pulse was allowed to more slowly decay exponentially after it had reached its peak value. In both cases, the resistance peaked just before the x-ray emission peaked and at a value of 0.5 Ω, which is slightly larger than the largest peak value used in the 0-D calculations. This value represents a more than two order of magnitude increase in resistance over that produced by Spitzer resistivity. Two curves are drawn in Fig. 15 that largely coincide with each other. The blue curve (marked volume calculation) undergoes small excursions away from the red curve (marked surface calculation) only at times when the pinch hits the axis and changes its direction of motion. The surface calculation of R_{load} comes from the formula derived above from the flux of electromagnetic energy through the outer pinch boundary. The volume calculation of R_{load} comes from the formula listed in Fig. 15, which is derived by integrating the magnetic field energy equation over the volume of the pinch. The agreement seen between these two curves provides a good measure of the accuracy of the magnetic field diffusion equation solver that is used in the 1-D calculation.

137

Compare Two Anomalous, Load
Resistance (1-D) Calculations

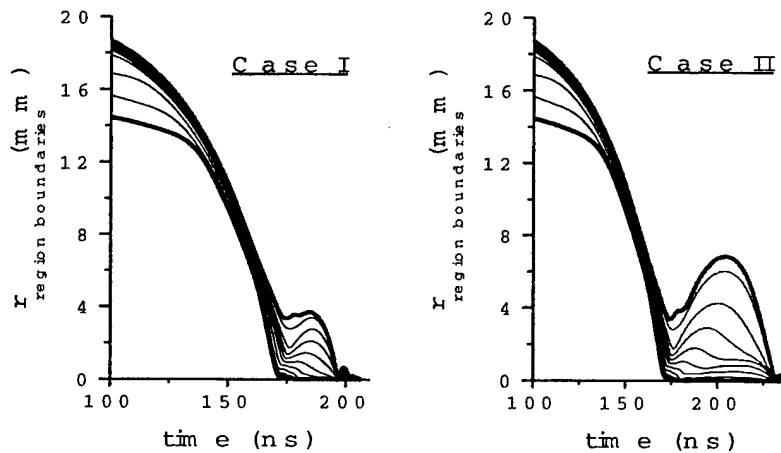Case I: Transient R   Case II: Sustained R
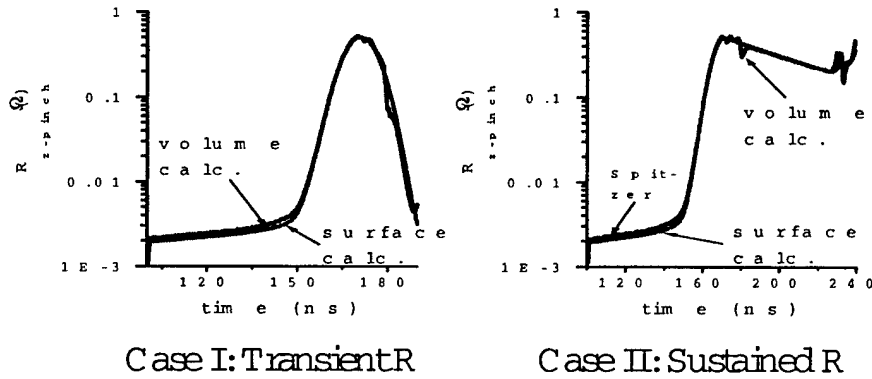
Volume calculation:

$$R_{load} = \frac{1}{I^2}\left(\frac{d}{dt}\int_{plasma} dV \frac{B_\theta^2}{8\pi} + \int_{plasma} dV \, j_z E_z\right) - \frac{1}{2}\frac{dL_{load}}{dt}$$

(All terms make significant contributions)

Figure 15. Two anomalous heating cases are studied: one without and one with a sustained heating following the main x-ray pulse.

Case I and II Implosion Dynamics

More energy input tends to produce more expansion rather than more x rays.

Figure 16. Implosion trajectories at different locations in the plasma are shown as a function of time.

138

Because the anomalous resistivity is several orders of magnitude larger than Spitzer resistivity and because there is no physical justification for introducing anomalous resistivity uniformly throughout the z-pinch, it must be gradually contoured down in the plasma interior from its surface value. For the calculations discussed in this report, this contouring was done mainly to demonstrate proof of principle, but otherwise, this problem needs further study. In these calculations, the resistivity was held at the same value throughout regions 1 and 2 (Fig. 11), and then it was linearly reduced throughout the next 5 regions of the plasma.

When large amounts of energy are absorbed by a z-pinch, two things can happen. If the energy is not radiated away rapidly enough and a significant fraction of it is stored as thermal energy, the hydrodynamics is energized and the plasma expands more rapidly following its assembly on axis than it would have if the energy had been radiated away as fast (or faster) as it was being supplied. These two outcomes are evident in Fig. 16 to varying degrees for cases I and II. In case I, enough energy is radiated during assembly for the current to maintain confinement of the plasma. In case II, more energy is ultimately supplied than can be completely reradiated, and a greater amount of plasma expansion occurs before the current regains control and produces the secondary, late-time implosion. This secondary implosion also occurs in case I, but it has much less energy than in case II. The late-time behavior that is predicted in 1-D calculations cannot be taken with complete seriousness because late-time implosions are weakened considerably in experiments by multi-dimensional effects. Nevertheless, while secondary implosion behavior is seldom seen experimentally with the strength predicted by 1-D calculations, some vestige of it is seen in the power pulses of shots 2693 and 2706 in Fig. 1. A small late-time spike indicative of a secondary implosion is seen on the feet of these x-ray pulses.

The energetics of these (case I and II) calculations are displayed in Figs. 17-20. For case I, $\sim$ 400 kJ coupled to the pinch, and more than 200 kJ of this energy came from Ohmic heating (Fig. 17). This energy was then radiated at assembly, in a single x-ray pulse with no foot of significance (Fig 18). This x-ray pulse was more strongly peaked and narrower than the one seen in shot 2636, and it produced only 350 kJ (but twice that seen in Fig. 14). For case II, the resistive energy input continued to rise as the anomalous resistivity slowly decayed until more than 500 kJ had been resistively coupled and more than 650 kJ in total (Fig. 19). In this case, the total x-ray power pulse had a foot similar to the ones seen in shots 2706 and 2693, and the foot had a sharply peaked secondary pulse near its termination point that corresponds to the more blunted secondary peaks seen in shots 2706 and 2693 (Fig. 20). In this case, more than 650 kJ was radiated in the calculation, more than in shot 2636, but less than in shot 2693. Notice that in both cases I and II, more energy was calculated to have been radiated from the K-shell than was seen experimentally, which is in keeping with the perfect 1-D symmetry in the calculations that is missing in the experiments. Finally, note that one can produce foot behavior without a secondary implosion spike in a calculation with anomalous heating. Fig. 21 illustrates a case II type implosion that produced no confinement following plasma assembly, but that nevertheless produced a late-time x-ray foot as some fraction of the late-time heating drove the expansion and the remaining fraction was radiated.
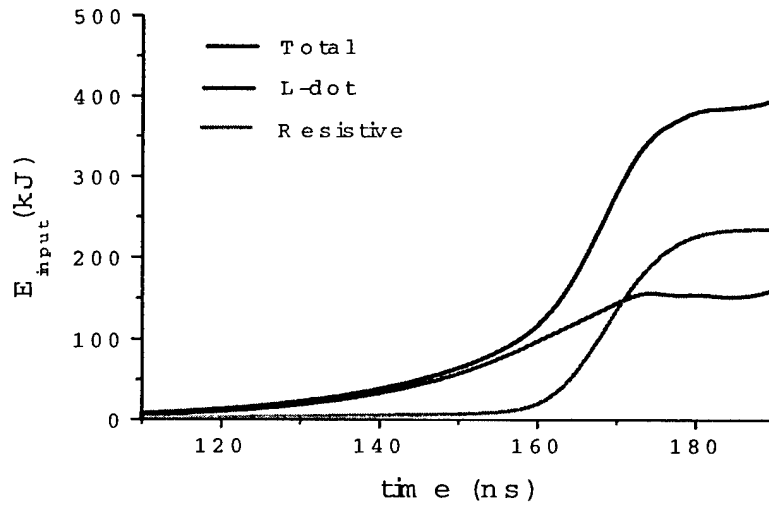
139

Case I Energy Input

Figure 17. Energy inputs to the pinch versus time when there is no sustained anomalous heating.
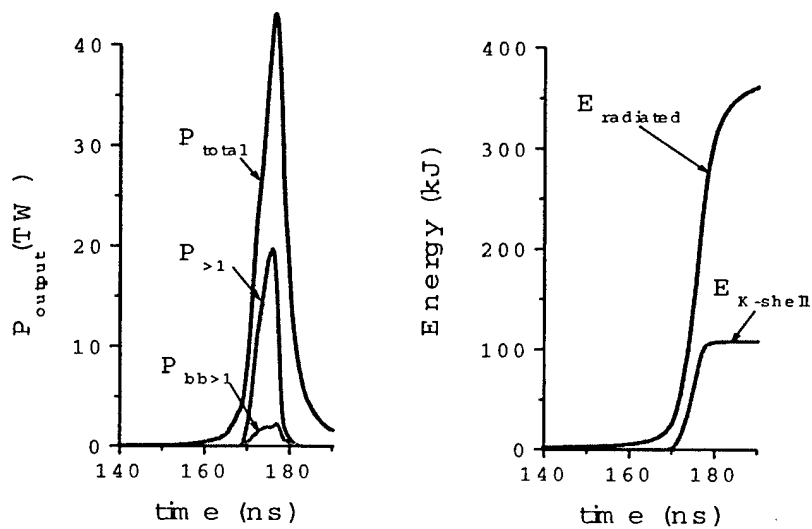
Case I Power and Energy Outputs

Figure 18. X-ray power and energy outputs versus time when there is no sustained anomalous heating.
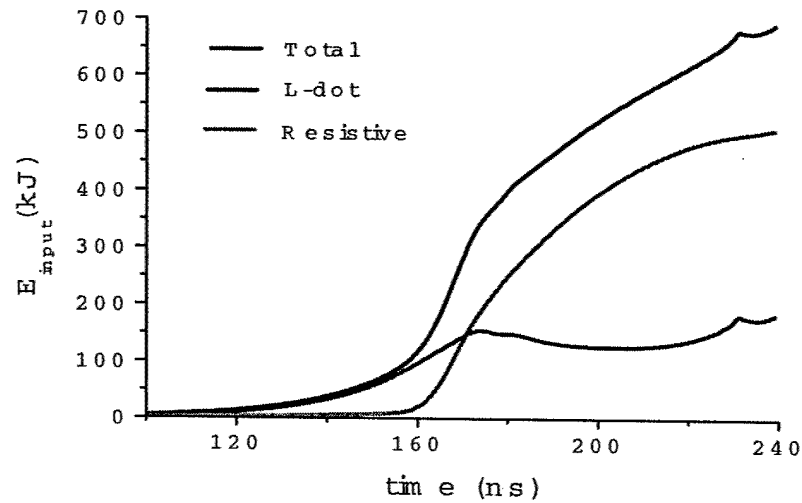
140

Case II Energy Input

Figure 19. Energy inputs to the pinch versus time when there is a sustained anomalous heating following the main x-ray pulse.
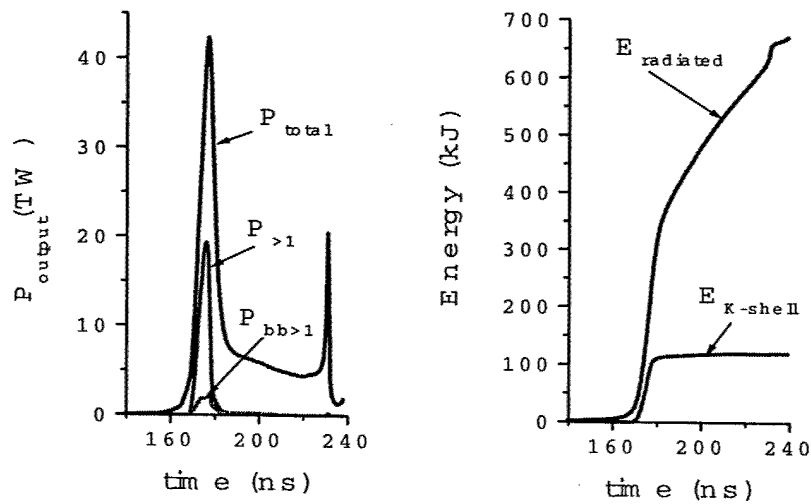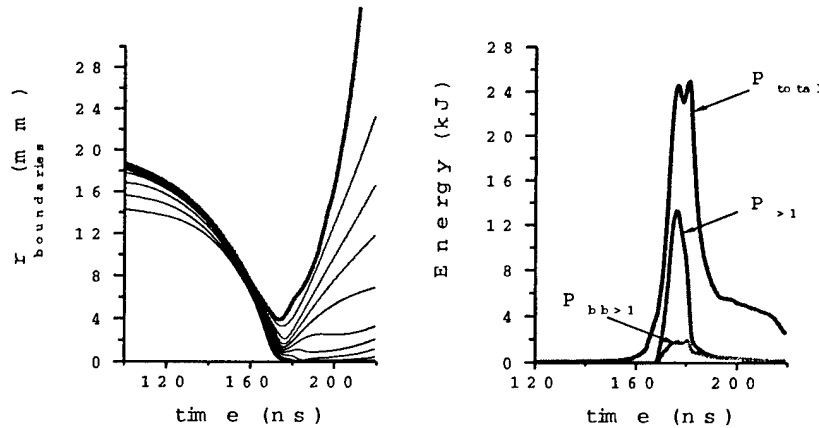
Case II Power and Energy Outputs

Figure 20. X-ray power and energy outputs versus time when there is a sustained anomalous heating following the main x-ray pulse.

Case III: A foot and no re-collapse

Energy not radiated goes into expansion kinetic
energy. In this calculation, a foot is nevertheless
produced in addition to the expansion.

Figure 21. X-ray power and energy outputs versus time when there is a sustained anomalous heating and no plasma re-collapse.

VI. Summary and Conclusions

The problem of anomalously high z-pinch energy coupling has only recently been observed and is just beginning to be researched. Much remains to be learned about it. It is not clear, for example, what causes the anomalous heating and two possibilities have been proposed. Both associate enhanced energy coupling with the anomalous build-up and dissipation of magnetic field energy within the pinch. Since much larger than expected x-ray outputs have been seen on the Saturn and Z machines, one might suspect that enhanced couplings get stronger as current risetimes and load currents increase.

The work described in this report offers proof-of-principle that a fluid calculation, once modified through the addition of an anomalously high resistivity, can replicate qualitatively and semi-quantitatively the behavior seen in the Saturn long current-risetime experiments. The next step in this research is to replace the prescribed resistivity with one that is calculated from plasma conditions present in the calculation. A formula for doing this was offered in Ref. 1. However, how this resistivity turns on, grows to saturation, and subsequently decays must still be guided by experiment. The fuller set of Saturn data also needs to be analyzed and, based on the phenomenology that is discovered, some new predictions for experiments need to be made.

It would be useful if load current measurements could be made that would verify directly, as in the Russian experiments, that z-pinch loads acquire anomalously high impedances whose time history can be tracked. However, while such current measurements are attempted, they are, at present, potentially deceptive as illustrated in Figs. 22 and 23. Fig. 22 shows a comparison

142

between a 2-D calculation, in which the Rayleigh-Taylor instability produced increased amounts of late-time load inductance and a large reduction in the calculated late-time current, and the corresponding measured experimental current trace, in which no such reduction was seen. This late-time discrepancy is troubling since the agreement between measured and calculated currents is excellent up to the time of peak current. Late-time errors in the measured current are suggested. On the other hand, Fig. 23 shows that measured currents can reflect some of the late-time behavior that is expected; namely, the shot with the greater energy output and the larger resistive loading did have a larger reduction in late-time current. Since the current traces for the two shots are in close agreement during their early rise, they do support the idea that anomalous resistance turns on late in these implosions. There is a problem with these measurements however. They reach minimum values at roughly the times of peak emission, which generally correlate with implosion times. However, since both loads had the same mass, the higher current shot (2636) is expected to implode earlier than shot 2693 in contradiction to what measurements showed.

2-D Calculated Current Compared to the Measured Current
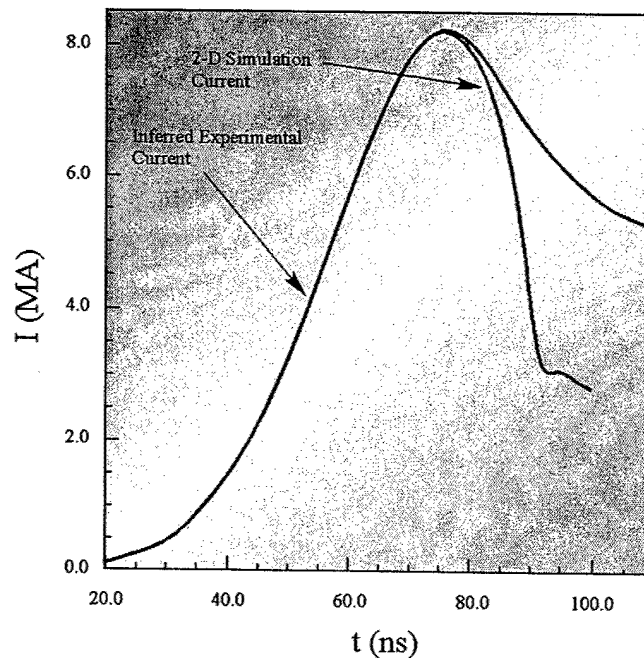
D.L.Peterson, et. al., Phys. Of Plasmas 5, 3302 (1998).

Figure 22. Comparison between a 2-D calculated and a measured circuit current versus time.

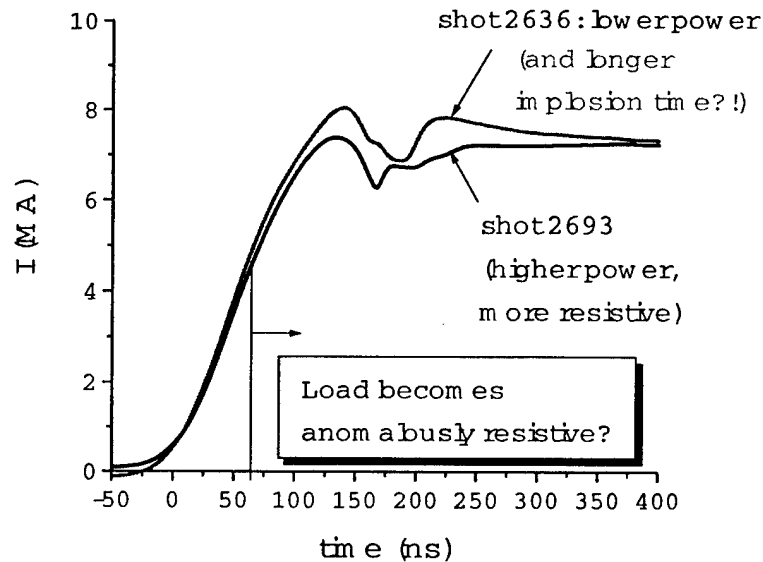# M isleading M easured Load Currents

Figure 23. Two measured diode currents versus time.

While many more steps need to be taken in order to better understand and interpret the data that was obtained in the Saturn long current-risetime experiments, the work described in this report does offer a promising first step. Shots 2636, 2693, and 2706 exhibited large variations in outcome even though they began with identical loads and were driven by the same generator. They had one quality in common, however. They all produced far more x-ray output than could be accounted for by a fluid dynamics that had only a Spitzer resistivity. Large, anomalously high, increases in electrical resistivity are required to input the energy into the plasma that is seen to be radiated from it experimentally. This requirement is supported by both 0-D and 1-D modeling. The 1-D calculations that were described in this report were also able to reproduce the variability seen in shots 2636, 2693, and 2706 through the addition of correspondingly variable amounts of anomalous resistivity.

144